Development of a
Piezoelectric Servo-Flap Actuator
for Helicopter Rotor Control

by

Eric Frederick Prechtl

B.S., Penn State University (1991)

Submitted to the Department of Aeronautics and Astronautics
in partial fulfillment of the requirements
for the degree of

Master of Science in Aeronautics and Astronautics

at the

Massachusetts Institute of Technology

May 1994

Author⎯⎯⎯⎯⎯⎯⎯⎯⎯⎯⎯⎯⎯⎯⎯⎯⎯⎯⎯⎯⎯⎯⎯⎯⎯⎯⎯⎯⎯

Department of Aeronautics and Astronautics
April 21, 1994

Certified by⎯⎯⎯⎯⎯⎯⎯⎯⎯⎯⎯⎯⎯⎯⎯⎯⎯⎯⎯⎯⎯⎯⎯⎯⎯

Professor Steven R. Hall
Department of Aeronautics and Astronautics
Thesis Supervisor

Accepted by⎯⎯⎯⎯⎯⎯⎯⎯⎯⎯⎯⎯⎯⎯⎯⎯⎯⎯⎯⎯⎯⎯⎯⎯⎯

Professor Harold Y. Wachman
Chairman, Departmental Graduate Committee

Development of a
Piezoelectric Servo-Flap Actuator
for Helicopter Rotor Control

by

Eric Frederick Prechtl

Abstract

An actuator using a piezoelectric bender to deflect a trailing edge servo-flap for use on a helicopter rotor blade was designed, built, and tested. This actuator is an improvement over one developed previously at MIT. The design utilizes a new flexure mechanism to connect the piezoelectric bender to the control surface. The efficiency of the bender was improved by tapering its thickness properties with length. Also, implementation of a nonlinear circuit allowing the application of a greater range of actuator voltages increased the resultant strain levels.

Experiments were carried out on the bench top to determine the frequency response of the actuator, as well as hinge moment and displacement capabilities. Flap deflections of 11.5 deg were demonstrated while operating under no load conditions at 10 Hz. Excessive creep at low frequencies precluded the measurement of achievable hinge moments, but extrapolation from deflection and voltage characteristics indicate that if properly scaled, the present actuator will produce flap deflections greater than 5 deg at the 90% span location on an operational helicopter. In addition, the first mode of the actuator was at seven times the rotational frequency (7/rev) of the target model scale rotor. Proper inertial scaling of this actuator could raise this modal frequency to 10/rev on an operational helicopter, which is adequate for most rotor control purposes.

A linear state space model of the actuator was derived. Comparisons of this model with the experimental data highlighted a number of mild nonlinearities in the actuator's response. However, the agreement seen between the experiment and analysis indicate that the model is a valid tool for predicting actuator response.

Acknowledgements

Contents

List of Figures

List of Tables

Notation

$\mathbf{A}_{\mathrm{ss}}$	state matrix
a	speed of sound
a_2, b_0	thin airfoil theory aerodynamic coefficients
$\vec{B}$	state control vector
b	bender width
b_{h}	half-width of bender
$\mathbf{C}$	actuator damping matrix
$\mathbf{C}^{\mathrm{E}}$	stiffness matrix measured at constant field
$\vec{C}_{\mathrm{ss}}$	output vector
$\overline{\mathbf{c}}$	modal damping matrix
C	capacitance of one half of bender
C_{f}	bender to flexure mechanism bond integrity coefficient
C_{H_α}	hinge moment coefficient per angle of attack
C_{H_δ}	hinge moment coefficient per flap deflection
C_{L}	coefficient of lift
C_{L_α}	lift coefficient per angle of attack
c	airfoil chord length
c_{f}	flap chord length
$\mathbf{D}$	plate bending inertia matrix
$\mathbf{d}$	piezoelectric strain coefficient matrix
$\tilde{\mathbf{d}}$	reduced piezoelectric strain coefficient matrix
$\widehat{\mathbf{d}}$	normalized piezoelectric strain coefficient matrix
$\vec{D}$	charge density vector
d_{31}	transverse piezoelectric strain coefficient
$\vec{E}$	electric field vector
$\mathbf{e}$	piezoelectric stress coefficient matrix
E	Young's modulus of piezoelectric ceramic
E_{d}	Young's modulus of Delrin
E_{f}	ratio of flap to airfoil chord length
F	applied vertical tip force
f	frequency (Hz)
f_1, f_2	half power frequencies
f_{n}	natural frequency of first mode

g	piezoelectric voltage coefficient matrix
h	piezoelectric stiffness coefficient matrix
h	distance between mid-planes of uniform bender
I	area moment of inertia
I_{F}	flap mass moment of inertia about flap hinge
I_{f}	bending inertia of member AB
I_i	moment of inertia of ith flexure in flexure mechanism
i	current
K	stiffness matrix
$\vec{\mathcal{K}}$	curvature vector
k_{B}	bender tip stiffness
$k_{\mathrm{B_s}}$	optimum tapered bender tip stiffness
k_{M}	modeled spring stiffness of flexure mechanism
k_{f}	modeled stiffness of member AB and bender – flexure mechanism bond
k_i	torsional stiffness of ith flexure in flexure mechanism
k_{δ}	linear flap hinge stiffness at bender tip
L_1, L_2	geometric lengths in flexure mechanism
l	bender length
l_{f}	length of member AB
l_i	length of ith flexure in flexure mechanism
M	mass matrix
M	bender moment
M_{F}	equivalent mass from rotational inertia of flap
M_{H}	flap hinge moment
M_{δ}	torsional flap hinge stiffness
$\vec{M}_{\Lambda}$	actuated moment vector
m	bender mass per unit area
$\overline{m_i}$	modal mass of ith mode
N	number of rotor blades
n	thickness parameter for uniform bender
$\vec{Q}$	forcing vector
Q	magnitude response at first mode
q	modal amplitude of assumed shapes
R	rotor blade radius

$\mathbf{S}$	compliance matrix
$\vec{S}$	strain vector
S_s	surface strain of beam in bending
s	actuator lever arm length
s_opt	impedance matched lever arm length
$\vec{T}$	stress vector
$\tilde{T}_\mathrm{Total}$	total actuator kinetic energy
T_tip	airfoil thickness at tip of bender
t	time
t_bt	bender tip thickness
t_i	thickness of ith flexure in flexure mechanism
t_o	optimum thickness of tapered bender
t_p	thickness of one piezoelectric wafer of uniform bender
t_s	shim thickness of linearly tapered bender
t_w	wall thickness of optimum tapered bender
U	free stream velocity
U_D	design point velocity
u	electric field input
$\mathbf{V}$	eigenvector matrix
V_0	DC bias voltage
V_B	bender strain energy
$V_\mathrm{B_s}$	optimum tapered bender strain energy
V_Bot	voltage applied to bottom half of bender
V_C	coercive voltage
V_F	free bender tip deflection energy
V_M	strain energy stored in flexure mechanism
V_P	poling voltage
V_Top	voltage applied to top half of bender
V_Total	total actuator strain energy
V_i	strain energy in ith flexure of flexure mechanism
V_in	input voltage to nonlinear circuit
V_out	output voltage from nonlinear circuit
V_se	strain energy of plate in bending
V_δ	flap deflection energy

W_{Total}	total work done from actuated strain
w	plate transverse deflections
w_{A}	constrained bender tip deflections
w_{F}	free bender tip deflections
$w_{\text{F}_{\text{s}}}$	optimum tapered free bender tip deflections
$\vec{x}$	state vector
y_0	flap deflection output
α	airfoil angle of attack
$\boldsymbol{\beta}$	inverse dielectric constant matrix
β_{r}	rigid angle of flexure mechanism
δ	flap deflection angle
δ_{A}	constrained flap deflection angle
$\delta_{\text{A}_{\text{D}}}$	design point flap deflection angle
δ_{F}	free flap deflection angle
$\boldsymbol{\varepsilon}$	dielectric constant matrix
$\overline{\varepsilon_3}$	normalized dielectric constant
ζ	viscous damping factor
η_{B}	bender efficiency
η_{c}	local bending constraint efficiency
η_q	impedance matching efficiency
η_{t}	tip deflection efficiency
Λ	actuation strain
λ_i	assumed mode shape frequency coefficient
ξ	assumed spanwise mode shape
ρ	free stream density
σ_i	assumed mode shape amplitude coefficient
ϕ	assumed lengthwise mode shape
Ω	rotor angular velocity
ω	frequency (rad/sec)
ω_i	natural frequency of ith mode

Subscripts

f	full scale parameter
m	model scale parameter

S	full scale to model parameter ratio

Superscripts

D	constant charge density elasticity measurement (open circuit)
E	constant electric field elasticity measurement (short circuit)
S	constant strain dielectric measurement (blocked)
T	constant stress dielectric measurement (free)
$(\bar{\ })$	non-dimensional parameter
$(\ )'$	matrix transpose operation

Chapter 1

Introduction

The normal operation of a helicopter rotor can result in vibration, noise, and aerodynamic inefficiencies. The source of these problems is the unsteady aerodynamic environment associated with rotor operation. The goal of helicopter rotor control is to reduce or eliminate these problems.

There are a number of sources of rotor vibration and noise. These include atmospheric turbulence, retreating blade stall, blade vortex and blade fuselage interactions, as well as blade and rotor instabilities (ground/air resonances) [21]. The majority of previous rotor control efforts involved blade root pitch actuation to eliminate vibrations at the rotor hub, so that none are transmitted to the fuselage and passenger compartment of the helicopter, *i.e.*, disturbance rejection at the hub. While efforts into this method of control have been successful, disturbance rejection in any system is most effective when the control is applied at the point where the disturbances enter the system. For helicopters, this suggests the presence of an actuator in the rotating frame.

Previous research at MIT by Spangler and Hall [45] demonstrated that actuation of a servo-flap with the use of piezoelectric ceramic benders is a feasible method of rotating frame actuation for helicopter rotor control. While they demonstrated appreciable flap deflections and force authority, they found that their design did not work entirely as expected, due to hinge friction and backlash present in the linkage connecting the bender and flap. This thesis describes the improvements made to this

actuator concept, resulting in a design with the potential for integration into a blade cross-section capable of producing adequate performance for rotor control.

In the following sections, a brief discussion of the methods used for rotor control is presented, and a survey is presented on the different approaches taken by previous researchers to affect the aerodynamics of airfoils and rotor systems. The chapter concludes by outlining the goals of this thesis and the specific organization of the following four chapters.

1.1   Rotor Control Methodologies

Rotor control is performed using blade pitch command inputs to reduce vibration, noise and/or aerodynamic inefficiencies. Two common types of rotor control are higher harmonic control (HHC) and individual blade control (IBC). The difference between these two types of rotor control is in what each treats as the *plant*. Higher harmonic control applies inputs to the rotor system, treating the group of N blades as the plant. Individual blade control is different, because it treats each blade as a separate plant and wraps a feedback loop around each blade in the rotating frame [26], [21].

Shaw *et al.* [43] applied higher harmonic control in a wind tunnel study of a 1/6 scale CH-47D demonstrating the possibilities of HHC. Using swashplate controlling electro-hydraulic actuators with the ability to actuate up to the 4/rev frequency, they were able to demonstrate a 90% decrease in vibratory shears at the hub (at the cost of a 20% increase in hub moments) or performance improvements of 4% and 6% drops in required power at advanced ratios of 0.37 and 0.31, respectively. Nguyen and Chopra [39] performed an analytical study of the same rotor and confirmed many of these results.

Individual blade control may be considered an improvement over HHC. In addition to attacking the problems addressed by HHC, using IBC the designer may address additional problems such as gust alleviation, attitude stabilization, lag damping augmentation, flapping stability at high advance ratios and individual blade tracking. As

18

shown by Ham [21], all of these tasks can be achieved to some degree using the conventional swashplate. Obviously, since the swashplate only provides a maximum of three degrees of freedom, however, for rotors with four or more blades, less improvement is obtained by applying IBC with just the swashplate.

Placing one actuator on each rotor blade provides the necessary degrees of freedom to take full advantage of IBC algorithms. Furthermore, in addition to the benefits discussed above, Kretz *et al.* [26], [27] have suggested that putting actuators on each blade could eliminate the need for the swashplate. This is desired because the swashplate is a coupling path between blades that leads to monocyclic pitch variations.

In the past, placing actuators in the rotating frame added either a substantial amount of weight or complexity to the rotor system design. Nevertheless, because there are so many benefits from placing an actuator in the rotating frame, the problem has been the subject of a number of studies. The next section provides a brief review of the subject.

1.2   Rotating Frame Actuation

The easiest location to place an actuator in the rotating frame is at the blade root, because little or no modification to the blades is required. However, such an actuator would only be able to provide root pitch actuation. Placing actuators over the span of the blade allows for spanwise varying pitch commands.

Advantages from applying a spanwise varying pitch schedule have been described in the literature. An analysis performed over 20 year ago addressed the effect of the built-in twist of a rotor blade on its aerodynamics [31]. The discussion in that study recognized the fact that the vibratory loads of a helicopter are a strong function of the blade twist. To minimize vibratory loads, a decreased negative twist is necessary on the advancing side while a simultaneous increased negative twist should be present on the retreating side. A torsionally flexible blade along with moment control inputs at the blade tip and root would accommodate such a twist schedule, significantly

improving the vibration reduction ability of a rotor system. More recently two studies at MIT have also demonstrated the benefits of blade mounted actuation. Specifically, Hall, Yang and Hall [20] determined that actual rotor systems operate with induced power losses 14% greater than would exist given a maximum coefficient of lift, $C_{\mathrm{L}} = 1.5$ and the ability to prescribe a specific lift pattern over the entire rotor area. A spanwise varying pitch command could therefore improve the efficiency of the rotor. In addition, Garcia [18] performed a linear state space analysis of an H-34 helicopter rotor equipped with blade mounted servo-flaps. The model included rigid blade flapping and elastic torsion. The results predicted control loads much less than those necessary for root pitch control in hover and forward flight. Finally, a study by Millott and Friedmann [37] also reported that the power requirements necessary to twist a flexible blade and perform rotor control are lower than those needed to perform full blade feathering control at the root.

From the above discussion, it is clear that it would be useful to have an actuator that can operate in the rotating frame, while providing acceptable amounts of control authority. The remainder of this survey will focus on methods that have been proposed for the control of the aerodynamics of wing sections, with the emphasis on actuators that are capable of introducing a spanwise varying pitch distribution on a rotor blade. This survey is broken down into passive and active methods.

1.2.1 Passive Methods

Landgrebe and Davis performed analytical studies on an aeroelastically tuned tab placed on the trailing edge of a helicopter blade [28]. The goal of the tab was to introduce a harmonic airload forcing so that, if sized and phased correctly, could reduce the harmonic vibration of the rotor blades. Results showed that while this approach leads to small reductions of in-plane shears at the hub, the increase in vertical shears there are too great for this method of control to succeed.

Following an idea used for fixed wing tips, Stroub *et al.* [46] designed and built a rotor blade, consisting of a conventional blade design with its outer 10% connected to the rest of the blade with a tension/torsion device. The centrifugal force pulls the

tip section away against the tension/torsion strap, forcing the strap to torque the tip section, rotating it nose up. The aerodynamic forces balance this motion and the result is net positive aerodynamic lift located at the tip. Wind tunnel results show a 12% reduction in power at cruise speeds. Additional benefits include 40-70% smaller blade bending moments along with reduced sensitivity to gusts. A stability analysis of such a free-tip blade was performed by Chopra [9].

1.2.2   Active Methods

The first study in actively controlling a blade mounted helicopter actuator was performed by Carpenter and Paulnock in 1950 [8]. This was an experiment run on the Langley helicopter tower, and was designed only to check the stability of a rotor controlled with blade mounted servo-flaps. Vibration effects were not addressed. An external airfoil of 15.5% span was mounted just behind the trailing edge and centered at the 75% spanwise location. The actuation of this flap was achieved using a pitch link system. Actuating flap deflections up to 15 deg, 1500 lbs of thrust and ±7 deg of rotor tilt were demonstrated. However, due to the extra drag associated with the external flap, there was a 6.5% increase in required power.

An experimental study performed in 1965 analyzed the propulsive force of a rotor with the inner 50% span following a different pitch schedule than the outer 50% [15]. The motivation behind this design came from the fact that a helicopter's maximum advance ratio is limited by the retreating blade stall. Using this design, the effects of this retreating blade stall were delayed enough to allow this rotor to reach substantially higher advance ratios than those of conventional helicopter rotors. Future work recommended in this study included determination if the design could be simplified by reducing the independent control surface into a large chord trailing edge flap.

One type of control used in a number of rotor studies for actuation in the rotating frame is circulation control [48]. Circulation control essentially consists of blowing a thin tangential jet of air out of the leading and trailing edges of an (usually elliptical) airfoil. This influx of air boosts the lift coefficients of the blade section. This technology has been applied in the X-wing project, a rotor system that can stop in

mid-flight and operate as a fixed wing aircraft with blades swept forward and back at 45 degree angles. Circulation control provides the lift and control necessary to make the transition from rotating to fixed wing operation and to operate as a fixed wing aircraft.

Some researchers have suggested using active materials for macroscopic shape control of an airfoil [3], [14], [29], [42]. Rossi *et al.* [42] used magnetostrictive struts to perform shape control on a fixed wing airfoil. While the design is too big and heavy for helicopter control, it does show excellent response upon activation of a closed loop shape control system utilizing LVDT sensors.

Others have investigated bending and twisting of entire lifting surfaces with surface bonded piezoelectric ceramics. Lazarus *et al.* [29] investigated inducing torsion in lifting surfaces using bending-twist and extension-twist coupled plates. Separately, Ehlers and Weishaar [14] have also investigated the same subject. These studies showed that for typical fixed wing aircraft, bending or torsion strain actuation may be as effective as trailing edge control surfaces [29]. However, because helicopter blades have such large aspect ratios, such an actuation method is not feasible for rotor control.

Research by Barrett [3] showed that by partially attaching piezoelectric ceramics, the stiffness of the attachment becomes larger in one particular direction. The force transmitted by such a piezoelectric ceramic is thus concentrated along this direction. By proper alignment, these Directionally Attached Piezos (DAP's) may induce twisting in a wing. Although no wind tunnel tests were performed, analytical studies predict that wings equipped with DAP's may induce a ΔC_L of 0.65 for Mach number up to 0.7, using reasonable electric fields.

Loewy and Tseng [32] analyzed a system with an aileron/tab configuration. By making the aileron/tab configuration unstable and using a simple feedback loop to stabilize it, the system becomes very sensitive to control inputs. Therefore, small tab deflections get amplified into larger aileron deflections.

The results of studies by Lemnios *et al.* [31] led Kaman Corporation to the development of their Controllable Twist Rotor (CTR). The CTR uses standard H-34

22

blades, with a servo-flap (essentially a small airfoil) appended behind the trailing edge, centered at the 89% span location. A conventional swashplate was used for root control of the blades, while the servo-flaps were connected to a second swashplate (below the first) with a pitch link system. Wind tunnel tests performed by Lemnios *et al.* [30] demonstrated blade loadings 20% greater than those seen in conventional H-34 rotors. This was attributed to stall alleviation of the system at high advance ratios. McCloud and Weisbrich [35] performed an additional wind tunnel investigation of this same rotor, applying multicyclic control inputs. The study showed the ability to decrease blade bending moments, while simultaneously decreasing control loads. The one problem discovered from these studies was that the external flap produced a tremendous amount of extra drag, resulting in higher power requirements to operate the rotor. The improvement suggested to overcome this problem was to fair the flap inside the blade, creating a control surface which operated much like an aileron on a fixed wing [30]. In the literature, this improved configuration has been termed the advanced controllable twist rotor [34].

As an attempt to design a flap deflecting mechanism compatible with an advanced CTR design, Fabunmi [16] has suggested a complex resonant ratchet mechanism for producing blade servo-flap deflections. By actuating a spring mass system at its resonance with a piezoelectric stack, attached to the airfoil's main spar, the system effectively cranks the flap up or down using a ratchet mechanism. This study was analytical only, but a bench test model was proposed as future work.

Spangler and Hall [45] presented a method of deflecting a faired flap within a rotor blade. Their actuator used piezoelectric ceramics to deflect a 10% trailing edge flap. Piezoelectric ceramics are normally large force, small displacement devices. Their usefulness in this application is produced by amplifying the piezoelectric ceramic deflections in two ways. The first amplification comes from bonding two piezoelectric plates together, and actuating them in bending. By doing this, the piezoelectric ceramic becomes a moderate force, moderated displacement actuator. The second amplification comes from using a lever arm arrangement to actuate angular deflections. By making the lever arm sufficiently short, the small tip deflections from the

bender translate into relatively large servo-flap deflections. For such a lever arm arrangement to work, however, in addition to the flap hinge degree of freedom, two additional hinge degrees of freedom are necessary to avoid encountering any geometric stiffening effects in actuating the flap deflections [45]. In their design, Spangler and Hall used small model aircraft hinges to provide these degrees of freedom. Spangler and Hall built and performed wind tunnel tests on a scaled rotor blade typical section. In their experiments, they encountered substantial reductions in performance due to large amounts of friction and backlash caused by these hinges. This thesis presents improvements over this original design, as discussed below in Section 1.3.

Independent of the research presented in this thesis, Walz and Chopra [47] are currently developing a flap deflection mechanism based on this piezoelectric bender idea of Spangler and Hall. The main difference implemented by Walz and Chopra is in the connection between piezoelectric bender and flap. They abandoned the three hinge mechanism for one involving a molded rod attached to the end of the piezoelectric bender and a precision machined cusp, such that the rod is able to slide and rotate as the piezoelectric bender deflects. Using this rod-cusp configuration, they were able to achieve 10% flap authority in a bench test experiment of their actuator. Incorporation of this model in an airfoil is currently underway and planned for hover and forward flight tests at the University of Maryland.

1.3 Thesis Objectives and Overview

1.3.1 Goals

As discussed in the previous sections, there are many benefits that may be obtained in helicopter rotor control by implementing an actuator in the rotating frame. The main goal of this thesis, therefore, was to improve on the design of Spangler and Hall [45], in order to develop an actuator capable of meeting the force and deflection requirements needed for a trailing edge servo-flap to exert useful control on the aerodynamics of

a rotor. Furthermore, bench tests of the re-designed actuator were recognized as a necessary measure of the degree to which this proposed goal was met.

1.3.2 Thesis Organization

This thesis is involved only with the re-design of Spangler and Hall's original actuator, which is defined, in this thesis, as the piezoelectric bender, servo-flap and the linkage connecting the two. The conceptual view of the proposed actuator located inside the cross-section of a target rotor blade is shown in Figure 1-1. This figure is a scale drawing of how the actuator presented in this thesis will fit within an airfoil. As shown, the bender is attached directly to the main airfoil spar, and its length is consistent with an airfoil possessing a 20% trailing edge flap. Two of the major improvements to the design that are discussed in this thesis are easily seen in the figure. The first and most important improvement is the use of the flexure mechanism to couple the bender and flap deflections. As shown, with this mechanism, the three hinges of Spangler and Hall's design have been replaced with three flexures. In addition, the aerodynamic surface has been included as an integrated member of the flexure mechanism part. As will be shown in this thesis, the use of the flexure mechanism results in the complete elimination of the friction and backlash problems encountered by Spangler and Hall. The second improvement shown is the use of a bender with tapered thickness properties. Using a taper increases the efficiency of the bender, while providing additional inertial and size benefits.

Each of the elements of the actuator along with its predicted and observed response are discussed in this thesis. The subjects contained specifically in each chapter are as follows. Chapter 2 describes the fundamental mechanisms that cause the piezoelectric effect, and a derivation of a state space model of the actuator, based on Classical Laminated Plate Theory, is given. The derivation presented there is made general enough to allow the incorporation of benders of other active materials, such as electrostrictive ceramics, into the design of the actuator. This model will be used for comparison purposes when the experimental data of the actuator is analyzed. The

chapter concludes with a comparison of the results predicted when the actuator is modeled as a plate as opposed to a beam.

Chapter 3 presents the original design equations of Spangler and Hall [45] and then treats the effect of the bender's geometry on its efficiency. Specifically, a discussion is presented on how tapering the properties of the bender can significantly increase its efficiency. Furthermore, the force requirements for such an actuator to operate effectively are estimated, and the scaling laws necessary for proper model tests of the proposed actuator are derived. The design of a nonlinear circuit which increases the maximum applied electric field and the associated circuit diagram (Appendix B) are presented. The chapter concludes by describing the design and fabrication of the flexure mechanism.

Chapter 4 discusses the construction and results of the bench test experiments of the designed actuator. Finally, Chapter 5 concludes the thesis by outlining the accomplishments and improvements of the present design and suggests a course for future research into this actuation mechanism.
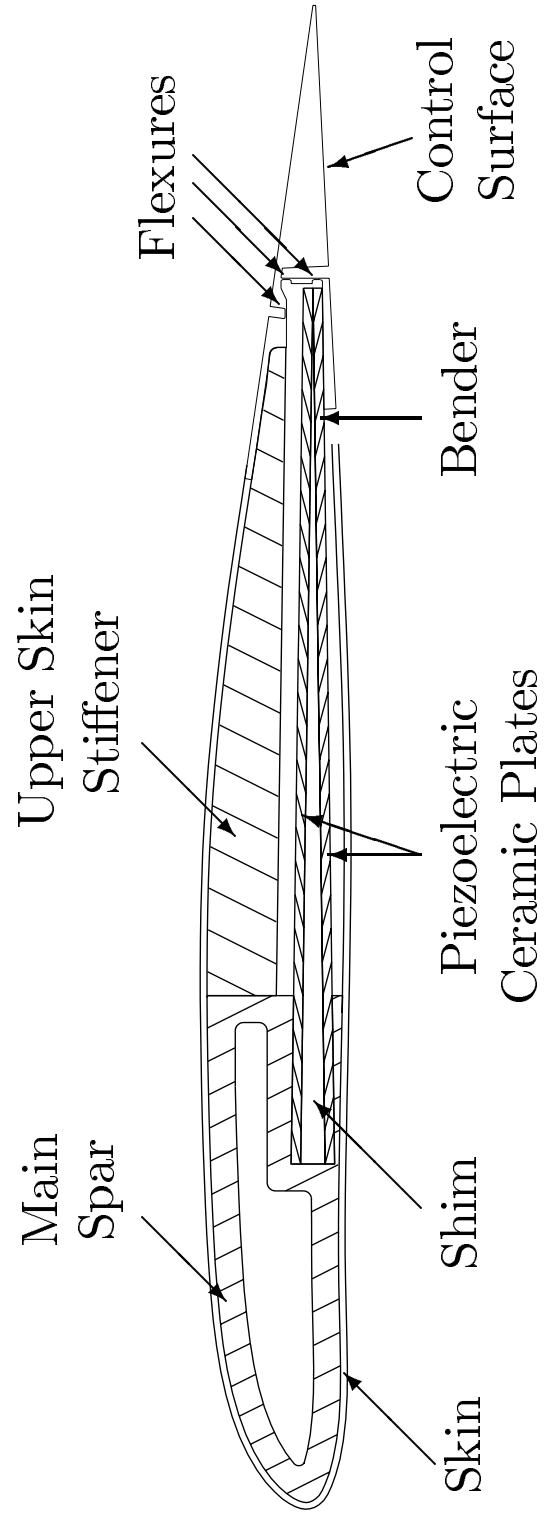
Figure 1-1: Concept of an airfoil with piezoelectrically actuated servo-flap

Chapter 2

Modeling of the Actuator

This chapter presents the derivation of the state space equation of motion of the actuator, where, as discussed in Section 1.3, the actuator is defined as the bender connected to a trailing edge servo flap using the flexure mechanism. While the bender used in the present study is a piezoelectric multi-morph, the derivation is made general enough to include benders of different types of active materials such as electrostrictive ceramics. However, because the material used in this study is piezoelectric ceramic, before the equation of motion is derived, the fundamental mechanisms behind the operation of piezoelectric ceramics are presented as a motivation for the governing equations used to describe their electro-mechanical behavior.

2.1 Piezoelectric Fundamentals

2.1.1 The Piezoelectric Effect

In Greek, the word *piezein* means to press. Thus, materials which generate an electric charge when mechanically deformed (and, reciprocally, those that mechanically deform when given an electric charge) are described as *piezoelectric*. Many materials in nature exhibit a certain amount of piezoelectricity. Examples include natural quartz crystal, and even human bone [41]. While the effect does exist, natural manifestations of piezoelectricity are rarely pronounced. However, specially manufactured ceramics

exhibit the property of piezoelectricity to such a degree that they find engineering applications.

To understand the mechanism that causes a material to possess piezoelectric properties, it is necessary to consider its behavior at the molecular level. A phenomenon called spontaneous polarization causes the piezoelectric effect [41]. In this phenomenon, the electron clouds in the atoms of the piezoelectric material displace to one side of their positively charged nucleus. In addition, positive ions in the crystal structures of the material also displace relative to their negative ions. Both of these effects create tiny electric dipoles out of the atoms and crystals. In a piece of untreated piezoelectric ceramic, all of these dipoles are oriented in a random fashion, making it impossible for any real piezoelectric effect to manifest itself. Figure 2-1(a) presents a conceptual view of this situation where a small cross-section of the material is shown with these randomly oriented dipoles. A macroscopic piezoelectric effect in the ceramic is obtained by *poling* it. A poled ceramic is one where the dipoles are aligned in the poling direction, as shown in Figure 2-1(b).

Poling is induced by placing a large electric field, referred to as the *poling field*, over the ceramic for an extended period of time. In Figure 2-1, this is represented by applying the poling voltage, V_P, over the thickness of the ceramic, where the poling voltage is simply the poling field times the ceramic thickness. The poling voltage in Figure 2-1(b) is positive. Because of this, the negatively charged sides of the dipoles are attracted to it and the positively charged sides are repelled from it, causing them to rotate and align with the electric field. Furthermore, because of these electrical forces, in addition to the rotation, the dipoles also stretch as shown in Figure 2-1(b). This dipole motion causes the ceramic to expand in the poling direction and, from Poisson effects, contract in the transverse directions. Upon removal of the poling field, the ceramic returns to its un-poled dimensions, but the dipoles remain aligned in the poling direction, which is what gives the ceramic its piezoelectric properties.

It must be acknowledged that this dipole model is a simplification of the true piezoelectric mechanism in two ways. The first simplification is that in the actual case, electric dipoles with similar orientation group themselves into tiny *domains* and
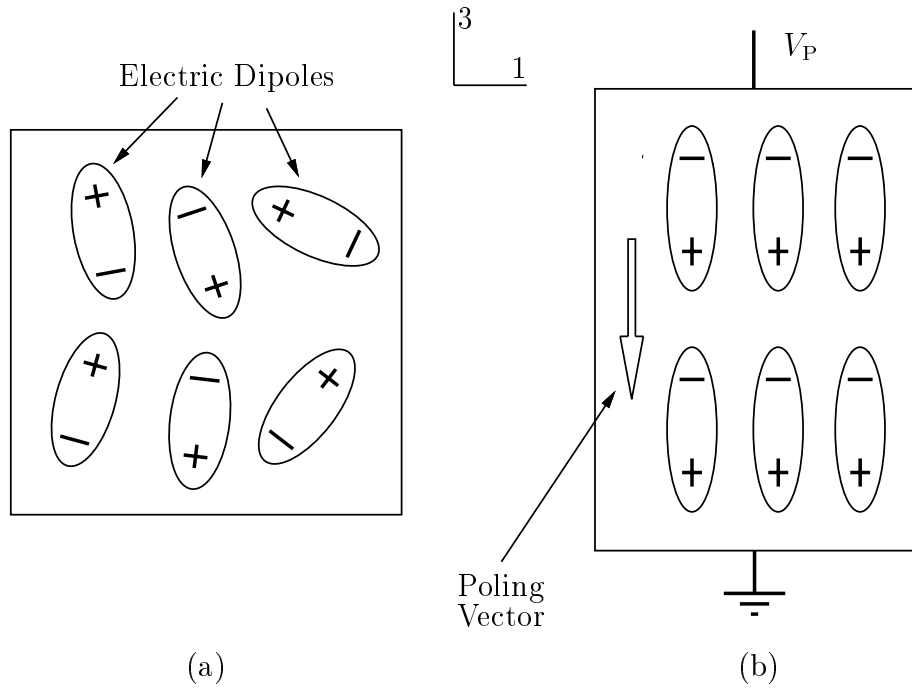
Figure 2-1: The change in dipole alignment upon poling a piezoelectric ceramic. (a) Randomly oriented dipoles do not allow piezoelectric effect to manifest itself. (b) Poling of ceramic aligns dipoles, leading to a macroscopic piezoelectric effect.

it is these domains which get aligned with the electric field upon polarization. The second simplification is that not all of these domains are able to completely align with the electric field due to micro-mechanical effects. However, enough do align to deliver the desired piezoelectric effect [41].

The environment necessary to pole a piezoelectric ceramic is not fixed. It is a function of the electric field level used, the length of time the electric field is applied and the temperature the ceramic is at during the process. For example, the piezoelectric ceramics used in the experiment discussed in Chapter 4 were poled by applying a 40 V/mil electric field over the ceramics at room temperature for 20 minutes. Larger electric fields may be used over shorter periods of time and vice-versa. Furthermore, if the temperature of the ceramic is raised, for example by immersing it in an oil bath, smaller electric fields and shorter periods of time are required to complete the

poling process. The maximum electric field that may be applied to a piezoelectric ceramic in the poling direction is limited only by the electrical breakdown level of the piezoelectric ceramic. This occurs at electric fields between 80 to 100 V/mil [41].

Obviously, an important characteristic of the poling field is its orientation. The poling vector is used to define this property. By convention, the poling vector points from the positive to negative poling electrodes and, furthermore, this direction is always defined as the 3 axis of the ceramic [41]. These conventional definitions of the poling vector and axis system of piezoelectric ceramics are shown in Figure 2-1.

Poling a piece of piezoelectric ceramic has a fundamental effect on both its electrical and mechanical properties. Because of the dipole alignment that occurs, the characteristics of the material in the poling direction, *i.e.*, along the 3 axis, become quite different from those in the plane defined by the 1 and 2 axes. Furthermore, within this plane, the properties become isotropic, meaning that the material exhibits the same characteristics, whether electrical or mechanical, in all directions. In elasticity, materials such as this, that exhibit isotropic behavior within one of its planes of symmetry, are sometimes referred to as *transversely isotropic* [25]. In the following discussion, this will be the term used to describe this property in piezoelectric ceramics.

It is possible to *depole* a piezoelectric ceramic by applying the *coercive field* across it. The coercive field is an electric field oriented in an opposite sense to the poling field. As with the poling field, the definition of the coercive field is not fixed. It is a function of the field level, time of application and temperature. For example, the coercive field is 30 V/mil while actuating the piezoelectric ceramic at 60 Hz but 15 V/mil for operation at DC. The line differentiating AC and DC operation, however, is not clearly defined and because exceeding the coercive field adversely affects the poled properties of the ceramic, it is important to set a coercive field limit appropriate to the actuation frequencies at which the ceramic operates.

2.1.2 Piezoelectric Constitutive Laws

In mechanics, Hooke's law relates the vectors of stress, $\vec{T}$, and strain, $\vec{S}$, in a material according to

$$\vec{S} = \mathbf{S}\vec{T} \tag{2.1}$$

where $\mathbf{S}$ is the compliance matrix of the material. In general, to describe the elastic state of a differential element of material, there are six components in the stress and strain vectors, denoted in engineering notation using subscripts from 1 to 6. The components of these vectors with subscripts of 1, 2 or 3 represent normal stress or strain in directions corresponding to the 1, 2 or 3 axis, respectively. Furthermore, the components with subscripts of 4, 5 or 6 represent shear stress or strain around the 1, 2 or 3 axis, respectively. To relate the stress and strain vectors, the compliance matrix, $\mathbf{S}$, must be a 6×6 matrix. The compliance matrix is symmetric [6]. Because of this, for a completely anisotropic material, it contains 21 independent constants. For materials such as piezoelectric ceramics, which exhibit transversely isotropic properties, however, the number of independent constants in the compliance matrix reduces to five and its form is [25]

$$\mathbf{S} = \begin{bmatrix} s_{11} & s_{12} & s_{13} & 0 & 0 & 0 \\ s_{12} & s_{11} & s_{13} & 0 & 0 & 0 \\ s_{13} & s_{13} & s_{33} & 0 & 0 & 0 \\ 0 & 0 & 0 & s_{44} & 0 & 0 \\ 0 & 0 & 0 & 0 & s_{44} & 0 \\ 0 & 0 & 0 & 0 & 0 & 2(s_{11} - s_{12}) \end{bmatrix} \tag{2.2}$$

In electricity and magnetism, Gauss's law for electricity relates the vectors of electric field, $\vec{E}$, and charge density, $\vec{D}$, according to

$$\vec{D} = \varepsilon \vec{E} \tag{2.3}$$

where ε is the matrix of dielectric constants. The electric field and charge density vectors have only 3 components. Each component represents either the electric field or

charge density directed in one of the main axial directions at a point in a body. In order to relate these two vectors, $\boldsymbol{\varepsilon}$ must be a 3×3 matrix. Because most piezoelectric ceramics have no cross-dielectric terms, the dielectric matrix is diagonal. Furthermore, because of the transversely isotropic property of piezoelectric ceramics, their dielectric constants in the 1 and 2 directions are equal.

For most linear materials, Hooke's Law and Gauss's Law can be applied independently of each other. However, because piezoelectric ceramics transduce mechanical and electrical energy, there is also a coupling term in the constitutive relations of piezoelectric ceramics that relates the electrical and mechanic properties. There are four equivalent forms of the coupling matrices, implying that there are four equivalent forms of the constitutive relations of these materials, depending on the choice of dependent and independent mechanical and electrical variables. These coupling matrices $\mathbf{d}$, $\mathbf{e}$, $\mathbf{g}$ and $\mathbf{h}$ are termed the piezoelectric strain, stress, voltage, and stiffness matrices according to the IRE Standards of Piezoelectric Crystals [23],[24]. Each of these coupling matrices have three rows and six columns. The four forms of the constitutive relations are [4]

$$\left\{ \begin{array}{c} \vec{T} \\ \vec{D} \end{array} \right\} = \left[\begin{array}{cc} \mathbf{C}^{\mathrm{E}} & -\mathbf{e}' \\ \mathbf{e} & \boldsymbol{\varepsilon}^{\mathrm{S}} \end{array} \right] \left\{ \begin{array}{c} \vec{S} \\ \vec{E} \end{array} \right\} \tag{2.4}$$

$$\left\{ \begin{array}{c} \vec{S} \\ \vec{D} \end{array} \right\} = \left[\begin{array}{cc} \mathbf{S}^{\mathrm{E}} & \mathbf{d}' \\ \mathbf{d} & \boldsymbol{\varepsilon}^{\mathrm{T}} \end{array} \right] \left\{ \begin{array}{c} \vec{T} \\ \vec{E} \end{array} \right\} \tag{2.5}$$

$$\left\{ \begin{array}{c} \vec{S} \\ \vec{E} \end{array} \right\} = \left[\begin{array}{cc} \mathbf{S}^{\mathrm{D}} & \mathbf{g}' \\ -\mathbf{g} & \boldsymbol{\beta}^{\mathrm{T}} \end{array} \right] \left\{ \begin{array}{c} \vec{T} \\ \vec{D} \end{array} \right\} \tag{2.6}$$

$$\left\{ \begin{array}{c} \vec{T} \\ \vec{E} \end{array} \right\} = \left[\begin{array}{cc} \mathbf{C}^{\mathrm{D}} & -\mathbf{h}' \\ -\mathbf{h} & \boldsymbol{\beta}^{\mathrm{S}} \end{array} \right] \left\{ \begin{array}{c} \vec{S} \\ \vec{D} \end{array} \right\} \tag{2.7}$$

where the prime ($'$) symbol in these equations denotes the matrix transpose operation.

34

These four equations are equivalent representations of the electro-mechanical state of the material they describe. The relationship of the terms in each are easily found by performing some simple matrix algebra on these equations [4]. For example, to transform Equation (2.5) into a form where the stress and charge density are the independent variables, as in Equation (2.6), the relation for the charge density in Equation (2.5) is rearranged to give

$$\vec{E} = -\left[\boldsymbol{\varepsilon}^{\mathrm{T}}\right]^{-1}\mathbf{d}\vec{T} + \left[\boldsymbol{\varepsilon}^{\mathrm{T}}\right]^{-1}\vec{D} \tag{2.8}$$

Substituting Equation (2.8) into the relation for the strain in Equation (2.5) gives

$$\vec{S} = \left[\mathbf{S}^{\mathrm{E}} - \mathbf{d}'\left[\boldsymbol{\varepsilon}^{\mathrm{T}}\right]^{-1}\mathbf{d}\right]\vec{T} + \mathbf{d}'\left[\boldsymbol{\varepsilon}^{\mathrm{T}}\right]^{-1}\vec{D} \tag{2.9}$$

Comparing Equations (2.8) and (2.9) with Equation (2.6), it can be seen that

$$\mathbf{S}^{\mathrm{D}} = \mathbf{S}^{\mathrm{E}} - \mathbf{d}'\left[\boldsymbol{\varepsilon}^{\mathrm{T}}\right]^{-1}\mathbf{d} \tag{2.10}$$

$$\mathbf{g} = \left[\boldsymbol{\varepsilon}^{\mathrm{T}}\right]^{-1}\mathbf{d} \tag{2.11}$$

$$\boldsymbol{\beta}^{\mathrm{T}} = \left[\boldsymbol{\varepsilon}^{\mathrm{T}}\right]^{-1} \tag{2.12}$$

Using a similar process, the relationship of all the parameters in these constitutive equations may be obtained.

Because the piezoelectric ceramics couple electrical and mechanical properties, the parameters used to describe them must also specify what boundary conditions existed on the material upon measurement of its properties. The superscripts in Equations (2.4), (2.5), (2.6) and (2.7) denote these conditions. The superscripts T and S refer to dielectric measurements taken at constant stress (free) and constant strain (blocked) boundary conditions, respectively, while the superscripts E and D refer to elasticity measurements made at constant field (short circuited) and constant charge density (open circuited) boundary conditions, respectively.

The coupling coefficient matrices for piezoelectric ceramics are not full. For example, the piezoelectric strain constant matrix for many commercially available piezo-
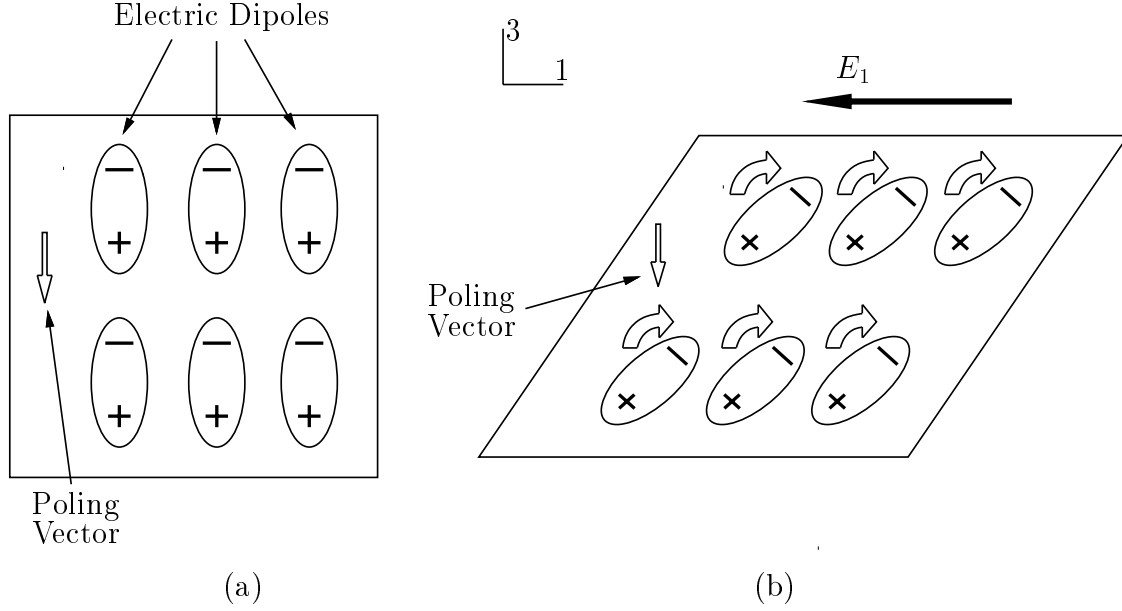
Figure 2-2: Schematic of d_{15} effect in piezoelectric ceramics. (a) Poled piezoelectric ceramic with no electric field applied. (b) Application of positive electric field in the negative 1 direction causes shearing around the 2 axis.

electric ceramics has the form

$$\mathbf{d} = \begin{bmatrix} 0 & 0 & 0 & 0 & d_{15} & 0 \\ 0 & 0 & 0 & d_{15} & 0 & 0 \\ d_{31} & d_{31} & d_{33} & 0 & 0 & 0 \end{bmatrix} \qquad (2.13)$$

In each of the constituents of Equation (2.13), the first subscript denotes the direction of the applied electric field and the second subscript indicates the resultant motion that the coefficient governs. The transversely isotropic nature of the piezoelectric ceramics make the coefficients relating to the 1 and 2 directions the same. Using the dipole model developed in Section 2.1.1, one can gain a physical understanding of each of these strain coefficients.

The effect of the d_{15} strain coefficient depends on the electric field present in the 1 (or 2) direction. An electric field applied in the 1 (or 2) direction causes a shearing of the piezoelectric ceramic around the 2 (or 1) axis, as shown in Figure 2-2. Assuming a positive electric field, E_1, the dipoles rotate, aligning their negative ends with the positive terminal (and vice-versa), shearing the material around the 2 axis, as shown.
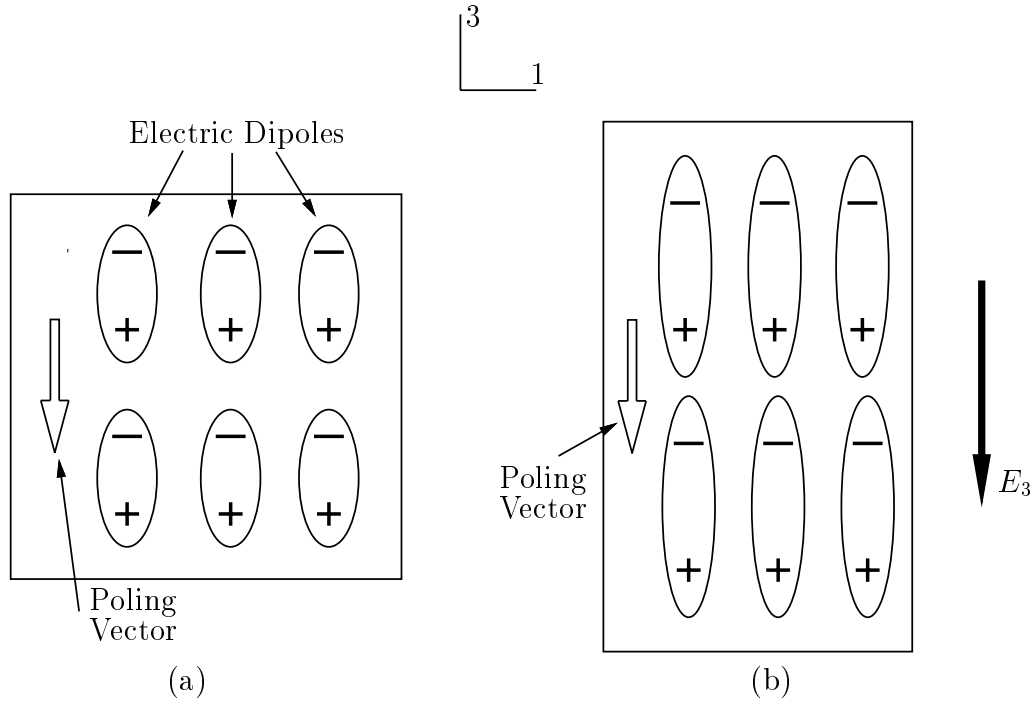
Figure 2-3: Schematic of d_{33} and d_{31} effect in piezoelectric ceramics. (a) Poled piezoelectric ceramic with no electric field applied. (b) Application of positive electric field in the negative 3 direction causes extension and the 3 direction and contraction in the 1 (and 2) direction.

Figure 2-3 shows the motions governed by the d_{33} and d_{31} coefficients upon application of an electric field in the 3 direction. In terms of the dipole model discussed earlier, when an electric field, E_3, is applied in the poling direction, the dipoles and ceramic move as they did during polarization. The negative ends of the dipoles move closer to the positive terminal while the positive half of the dipoles undergo the reverse motion. The material therefore extends in the 3 direction. The amount of strain produced in this direction for a given applied electric field is expressed by the d_{33} coefficient. In addition, due to Poisson effects and additional alignment of the dipoles, the ceramic also contracts in the 1 and 2 directions. The amount of strain produced in these transverse directions for a given applied field is expressed by the d_{31} coefficient. If E_3 becomes negative, both ends of the dipoles get repulsed towards the center of the cross-section, contracting the piezoelectric ceramic in the 3 direction and necessarily extending it in the other two directions.
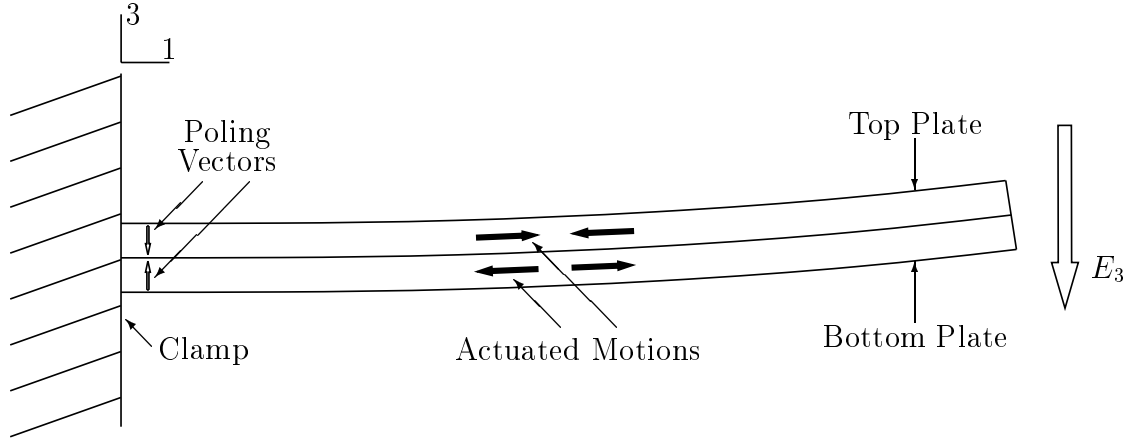
Figure 2-4: Operation of piezoelectric bender.

In the operation of a bender, it is the strain in the transverse direction, governed by the d_{31} coefficient, that actually bends the structure. This is done by bonding two piezoelectric plates together, as shown in Figure 2-4. If one of the plates has an electric field placed over it in the poling direction, like that shown in Figure 2-3, it will try to contract in its transverse directions. However, if the other plate has an electric field placed over it, oriented in the coercive field direction, *i.e.*, directly opposite to that shown in Figure 2-3, it will try to expand in its transverse directions. Because these plates are rigidly bonded together, each will constrain the other's motion. The result will be a bending deflection of the aggregate structure in a direction towards the plate in compression, *i.e.*, toward the plate with the electric field oriented in the poling direction, as shown in Figure 2-4.

2.2 Actuator Equation of Motion

2.2.1 Assumptions

Because assumptions will be made below about the stress and electric field present in the bender, Equation (2.5) is used as a starting point in the derivation. The full

9×9 constitutive law is given by

$$
\left\{
\begin{array}{c}
S_1 \\
S_2 \\
S_3 \\
S_4 \\
S_5 \\
S_6 \\
\\
D_1 \\
D_2 \\
D_3
\end{array}
\right\}
=
\left[
\begin{array}{ccccccccc}
s_{11}^{\mathrm{E}} & s_{12}^{\mathrm{E}} & s_{13}^{\mathrm{E}} & 0 & 0 & 0 & 0 & 0 & d_{31} \\
s_{12}^{\mathrm{E}} & s_{11}^{\mathrm{E}} & s_{13}^{\mathrm{E}} & 0 & 0 & 0 & 0 & 0 & d_{31} \\
s_{13}^{\mathrm{E}} & s_{13}^{\mathrm{E}} & s_{33}^{\mathrm{E}} & 0 & 0 & 0 & 0 & 0 & d_{33} \\
0 & 0 & 0 & s_{44}^{\mathrm{E}} & 0 & 0 & 0 & d_{15} & 0 \\
0 & 0 & 0 & 0 & s_{44}^{\mathrm{E}} & 0 & d_{15} & 0 & 0 \\
0 & 0 & 0 & 0 & 0 & s_{66}^{\mathrm{E}} & 0 & 0 & 0 \\
\\
0 & 0 & 0 & 0 & d_{15} & 0 & \varepsilon_{11} & 0 & 0 \\
0 & 0 & 0 & d_{15} & 0 & 0 & 0 & \varepsilon_{11} & 0 \\
d_{31} & d_{31} & d_{33} & 0 & 0 & 0 & 0 & 0 & \varepsilon_{33}
\end{array}
\right]
\left\{
\begin{array}{c}
T_1 \\
T_2 \\
T_3 \\
T_4 \\
T_5 \\
T_6 \\
\\
E_1 \\
E_2 \\
E_3
\end{array}
\right\}
\qquad (2.14)
$$

where

$$
s_{66}^{\mathrm{E}} = 2(s_{11}^{\mathrm{E}} - s_{12}^{\mathrm{E}})
$$

In general, solving these nine coupled equations for the resultant response of the piezoelectric material is unnecessary because, in most cases, reasonable simplifying assumptions may be made to reduce these equations. This is also the case in the present situation, and the assumptions made are motivated by considering the operation of the actuator.

In analyzing the bender, the first fact to realize is that it is a plate. This is evident from the fact that for the bender used in the present study, its free length to width ratio is 1.33. In addition, the thickness of this bender is less than 5% of its length at all points. For these reasons, it is valid to reduce the three dimensional elasticity relations in Equation (2.14) to two dimensions by making a plane stress assumption [6]. Specifically, a plane stress assumption specifies that all components of stress in the 3 direction are zero. This implies that

$$
T_3 = T_4 = T_5 = 0
$$

The second assumption is generated from the fact that the electric field is applied only in the 3 direction. Therefore, the component of the electric field in the 1 and 2 directions are set to zero.

Using these two assumptions on the electric field and stress, Equation (2.14) reduces to

$$\left\{ \begin{array}{c} \vec{S} \\ D_3 \end{array} \right\} = \left[\begin{array}{cc} \mathbf{S}^{\mathrm{E}} & \widehat{\mathbf{d}} \\ \tilde{\mathbf{d}}' & \overline{\varepsilon_3} \end{array} \right] \left\{ \begin{array}{c} \vec{T} \\ \Lambda \end{array} \right\} \tag{2.15}$$

where

$$\mathbf{S}^{\mathrm{E}} = \left[\begin{array}{ccc} s_{11}^{\mathrm{E}} & s_{12}^{\mathrm{E}} & 0 \\ s_{12}^{\mathrm{E}} & s_{11}^{\mathrm{E}} & 0 \\ 0 & 0 & s_{66}^{\mathrm{E}} \end{array} \right]$$

$$\widehat{\mathbf{d}} = \left[\begin{array}{c} 1 \\ 1 \\ 0 \end{array} \right]$$

$$\tilde{\mathbf{d}} = \left[\begin{array}{c} d_{31} \\ d_{31} \\ 0 \end{array} \right]$$

$$\overline{\varepsilon_3} = \frac{\varepsilon_{33}}{d_{31}}$$

and s_{66}^{E} has the same definition as in Equation (2.14). Note that the applied electric field term, E_3, has been replaced by a general actuation strain term, Λ, according to the discussion of Crawley and Anderson [10]. For the piezoelectric benders used in the present study, $\Lambda = d_{31} E_3$. However, this form of the actuation term allows the substitution of benders of other active materials, such as electrostrictive ceramics, into this derivation by calculating and including an appropriate value for Λ at this point in the derivation.

The ultimate goal of this study was to demonstrate the actuator's performance characteristics in a bench top model only. Because of this, no aerodynamic terms will be included in this derivation.

2.2.2 Rayleigh Ritz Analysis

While an exact solution of the partial differential equation of motion of this actuator would be useful, the effort involved in obtaining such a solution is not warranted

because only an estimate of the low frequency dynamics, *i.e.*, those frequencies less than the second modal frequency of the system, is desired for this study. Therefore, an approximate solution method is utilized here to predict the response of the actuator.

The Rayleigh-Ritz energy method is used to obtain the equation of motion [36]. In this method, one expresses the potential energy, kinetic energy and work terms of the structure being analyzed. The potential energy is the sum of the strain energy in the bender and the potential energy from the stiffness of the flexures in the flexure mechanism. The strain energy in a plate undergoing pure bending is [10]

$$V_{\text{se}} = \frac{1}{2} \int_V z^2 \vec{\mathcal{K}}' \mathbf{C}^{\text{E}} \vec{\mathcal{K}} \, dV, \tag{2.16}$$

where $\mathbf{C}^{\text{E}}$ is the stiffness matrix of the piezoelectric ceramic and $\vec{\mathcal{K}}$ is the vector of curvatures. The stiffness matrix is related to the compliance matrix of Equation (2.15) as

$$\mathbf{C}^{\text{E}} = \left[\mathbf{S}^{\text{E}} \right]^{-1} \tag{2.17}$$

and the curvature vector is defined as

$$\vec{\mathcal{K}} = - \begin{Bmatrix} \dfrac{\partial^2 w}{\partial x^2} \\[2ex] \dfrac{\partial^2 w}{\partial y^2} \\[2ex] 2 \dfrac{\partial^2 w}{\partial x \partial y} \end{Bmatrix} \tag{2.18}$$

In this derivation, $w(x, y)$ represents the transverse deflection of the bender. The transverse deflections act in the z direction, which corresponds to the piezoelectric ceramic 3 axis, consistent with the coordinate definition of Figure 2-4. The transverse deflections are a function of two variables, x and y. The lengthwise x axis corresponds to the piezoelectric ceramics' 1 axis, also shown in Figure 2-4. Furthermore, by the right hand rule, the spanwise y axis, corresponding to the piezoelectric ceramics' 2 axis, is therefore oriented into the page in Figure 2-4. In this analysis, the coordinate origin is located at the bender support with $z = 0$ and $y = 0$ corresponding to the

center of the bender's cross-section there.

Using Classical Laminated Plate Theory [25], a bending inertia matrix $\mathbf{D}$ is defined as

$$\mathbf{D} = \int_z z^2 \mathbf{C}^{\mathrm{E}}\, dz \tag{2.19}$$

Combining this definition with Equation (2.16) gives the plate strain energy as

$$V_{\mathrm{se}} = \frac{1}{2} \int_x \int_y \vec{\mathcal{K}}' \mathbf{D} \vec{\mathcal{K}}\, dy\, dx \tag{2.20}$$

In Figure 1-1, the relationship of the bender to the flexure mechanism was shown. Because of the stiffness contributed by the flexures and the inertia of the flap, the effects of the flexure mechanism must be taken into account in this model. The stiffness of the flexure mechanism is modeled as a linear spring located at the tip of the bender, $x = l$. Its spring constant, k_{M}, represents a stiffness per unit span. Therefore, a spanwise integration must be performed to find the potential energy stored by this spring. This potential energy is

$$V_{\mathrm{M}} = \frac{1}{2} k_{\mathrm{M}} \int_y w^2(l, y)\, dy, \tag{2.21}$$

Summing Equations (2.20) and (2.21) gives the total potential energy in the system by

$$V_{\mathrm{Total}} = \frac{1}{2} \left\{ \int_x \int_y \vec{\mathcal{K}}' \mathbf{D} \vec{\mathcal{K}}\, dy\, dx + k_{\mathrm{M}} \int_y w^2(l, y)\, dy \right\} \tag{2.22}$$

The kinetic energy is also a sum of the kinetic energy of the bender and that due to the rotational inertia of the flap. The inertia of the flap will have a large effect on the dynamics of the actuators. The lever arm distance between the flap hinge and the point where the vertical forces from the bender are applied is represented by the symbol s. From the small angles formula, the flap deflections, δ, are then related to the bender's tip deflections as

$$\delta = \frac{\int w(l, y)\, dy}{sb} \tag{2.23}$$

where b is the width of the bender. Using this expression, the kinetic energy from

the flap is found and added to that of the bender, giving the total actuator kinetic energy as

$$\widetilde{T}_{\text{Total}} = \frac{1}{2} \left\{ \int_x \int_y m\dot{w}^2(x, y) \, dy \, dx + \frac{I_{\text{F}}}{s^2} \int_y \dot{w}^2(l, y) \, dy \right\}, \tag{2.24}$$

where $\dot{(\ )}$ is the derivative with respect to time, m is the mass per unit area of the bender and I_{F} is the mass moment of inertia per unit span of the flap about the flap hinge.

The work done on the system by actuating the bender is [10]

$$W_{\text{Total}} = \int_x \int_y \vec{\mathcal{K}}' \vec{M}_{\Lambda} \, dy \, dx, \tag{2.25}$$

where the moment created by the piezoelectric ceramics is given by

$$\vec{M}_{\Lambda} = \int_z z \mathbf{C}^{\text{E}} \vec{\Lambda}(z) \, dz \tag{2.26}$$

In the Rayleigh-Ritz analysis, assumed mode shapes are chosen, describing the bender's transverse deflections. The actual mode shapes chosen must satisfy the geometric boundary conditions of the actuator [36]. These mode shapes consist of a non-dimensional spatial shape multiplied by a dimensional (with units of length) temporal modal amplitude, so that

$$w(x, y, t) = \sum_{i=1}^{n} q_i(t) \phi_i \left(\frac{x}{l}\right) \xi_i \left(\frac{y}{b_{\text{h}}}\right), \tag{2.27}$$

where n is the number of mode shapes used. Note that the non-dimensional spatial mode shapes consist of uncoupled lengthwise, ϕ_i, and spanwise, ξ_i, components.

Substituting this expression for w into Equations (2.22), (2.24) and (2.25) yield a stiffness and mass matrix along with a forcing vector [36]. The entry at the ith row and jth column of the stiffness matrix is

$$K_{ij} = \int_x \int_y \left(\phi_{i_{xx}} \phi_{j_{xx}} D_{11} \xi_i \xi_j + \phi_{i_{xx}} \phi_j D_{12} \xi_i \xi_{j_{yy}} + \phi_i \phi_{j_{xx}} D_{21} \xi_{i_{yy}} \xi_j + \right.$$
$$\left. \phi_i \phi_j D_{22} \xi_{i_{yy}} \xi_{j_{yy}} + 4\phi_{i_x} \phi_{j_x} D_{66} \xi_{i_y} \xi_{j_y} \right) dy \, dx +$$

Table 2.1: Assumed transverse mode shapes.

Mode Number i	Lengthwise Component $\phi_i\left(\frac{x}{L}\right)$	Spanwise Component $\xi_i\left(\frac{y}{b_h}\right)$
1−5	$\cosh\left(\lambda_i\frac{x}{L}\right) - \cos\left(\lambda_i\frac{x}{L}\right) - \sigma_i\left(\sinh\left(\lambda_i\frac{x}{L}\right) - \sin\left(\lambda_i\frac{x}{L}\right)\right)$	1
6−10	$\cosh\left(\lambda_j\frac{x}{L}\right) - \cos\left(\lambda_j\frac{x}{L}\right) - \sigma_j\left(\sinh\left(\lambda_j\frac{x}{L}\right) - \sin\left(\lambda_j\frac{x}{L}\right)\right)$	$\left(\frac{y}{b_h}\right)^2$

$$k_\mathrm{M}\phi_i(1)\phi_j(1)\int_y \xi_i\xi_j\,dy \tag{2.28}$$

Likewise, the i,jth term in the mass matrix is

$$M_{ij} = \int_x\int_y m\phi_i\phi_j\xi_i\xi_j\,dy\,dx + \frac{I_\mathrm{F}}{s^2}\phi_i(1)\phi_j(1)\int_{-b_\mathrm{h}}^{b_\mathrm{h}}\xi_i\xi_j\,dy \tag{2.29}$$

Finally, the entry in the ith row of the forcing vector is

$$Q_i = \int_x\int_y -\left(\phi_{i_{xx}}\xi_i M_{\Lambda_1} + \phi_i\xi_{i_{yy}}M_{\Lambda_2}\right)dy\,dx, \tag{2.30}$$

where the subscripts *1* and *2* on the M_Λ terms refer to the first and second component of the vector in Equation (2.26).

The mode shapes chosen in the present study were motivated by the analysis of Anderson [2]. Ten mode shapes were used. They are shown in Table 2.1. Note that $j = i - 5$ for the lengthwise components of the last five mode shapes in this table. In addition, the values of λ_i and σ_i for each mode appear in Appendix A. The ten mode shapes may be grouped into two sets of five. The lengthwise components in each set correspond to the first five exact modes of a cantilever beam [7]. The spanwise components of the first set are constant, reflecting the fact that the first five mode shapes represent pure cantilever bending. The spanwise components of the second set of five mode shapes allow for some parabolic bending to occur across the width of the bender. Spanwise bending such as this is often referred to as *anticlastic*.

Because the lengthwise and spanwise components of the mode shapes are uncoupled, the integrations in the stiffness, mass and forcing expressions of Equations (2.28), (2.29) and (2.30) can be performed independently in each direction. The spanwise components of these expressions integrate easily. The mode shapes in the x direction, however, involve more complicated functions. For a uniform plate or beam, these integrals are easily found in a good reference book such as Blevins [7]. However, for the present study, the bender used possessed a specific layered geometry as discussed in Section 4.1. For this reason, these integrations were calculated numerically. A Simpson's rule integration easily provides results with acceptable accuracy. However, to maximize the accuracy for this analysis, a more lengthy numerical integration routine, an adaptive recursive Newton Cotes 8 panel rule, implemented in Matlab using the QUAD8 command [33] was used. The integrations took a great deal of time to run, even considering that, from symmetry arguments, just over $\frac{1}{8}$ of all the entries in Equation (2.28) required computation. After completion, a number of the calculated values were checked using a simple Simpson's rule program and it was determined that using Simpson's rule provided equivalent answers up to the third or fourth significant figure. Considering the time involved, Simpson's rule integration is sufficient.

Once computed, the results of the integrations are stored in a look-up matrix for use with a Matlab script file in order to assemble the mass, stiffness and forcing matrices. The resultant equation of motion is

$$\mathbf{M}\ddot{\vec{q}} + \mathbf{K}\vec{q} = \vec{Q} \tag{2.31}$$

Equation (2.31) includes no damping term. However, piezoelectric ceramics are inherently lossy materials. This means that if a piezoelectric ceramic is driven at a certain frequency, in each period of oscillation a finite amount of energy is dissipated as heat in the ceramic. While the amount of damping in the ceramic is not overwhelming, in order to accurately predict the response of the bender, its effect should be accounted for.

Two common types of damping found in structures are modal damping and hys-

teretic damping. The response of the actuator presented in Sections 4.2.2 and 4.2.3, suggests that hysteretic damping is the predominant damping mechanism in the operation of piezoelectric ceramics. Unfortunately, hysteresis is a nonlinear phenomenon, independent of frequency. For this reason, it would be very difficult to include its effect in the equation of motion. Modal damping, on the other hand, which is a function of frequency, can easily be accounted for in the equation of motion by including a viscous damping term so that Equation (2.31) becomes

$$\mathbf{M}\ddot{\vec{q}} + \mathbf{C}\dot{\vec{q}} + \mathbf{K}\vec{q} = \vec{Q} \tag{2.32}$$

The amount of damping in a structure, whether it is modal or hysteretic, is proportional to the square of the amplitude of motion [36]. Therefore, for lightly damped structures such as piezoelectric benders, the effects of damping are only predominant at the resonances of the structure. So even if hysteretic damping is predominant, its effect can be adequately approximated by using the viscous damping model of Equation (2.32), with a damping level equivalent to the experimentally measured levels present at the first modal frequency of the actuator.

Modal damping is a useful model to account for the damping because it implies that the damping matrix, if transformed into modal coordinates, is proportional to the modal mass and stiffness matrices. Therefore, using the eigenvector matrix, $\mathbf{V}$, of the homogeneous form of Equation (2.31), the modal damping matrix is given by [36]

$$\mathbf{V}'\mathbf{C}\mathbf{V} = \overline{\mathbf{c}} = \begin{bmatrix} \ddots & & 0 \\ & 2\zeta\overline{m_i}\omega_i & \\ 0 & & \ddots \end{bmatrix}, \tag{2.33}$$

where ω_i and $\overline{m_i}$ are the natural frequency and modal mass of the ith mode, respectively, and ζ is the viscous damping factor. For reasons discussed above, the size of the viscous damping factor is found from experimental measurements of the actuator's first mode. The method used to do this is described in Section 4.2.2. This experimentally determined value of the viscous damping factor is substituted into

46

Equation (2.33) and the damping matrix used in Equation (2.32) is obtained by

$$\mathbf{C} = (\mathbf{V}')^{-1}\overline{\mathbf{c}}(\mathbf{V})^{-1} \tag{2.34}$$

Using the state vector

$$\vec{x} = \left\{ \begin{array}{c} \vec{q} \\ \dot{\vec{q}} \end{array} \right\}$$

Equation (2.32) transforms to a state space model of the form

$$\dot{\vec{x}} = \mathbf{A}_{\text{ss}}\vec{x} + \vec{B}_{\text{ss}}u \tag{2.35}$$

Where $\mathbf{A}_{\text{ss}}$ and $\vec{B}_{\text{ss}}$ are

$$\mathbf{A}_{\text{ss}} = \begin{bmatrix} \mathbf{0} & \mathbf{I} \\ -\mathbf{M}^{-1}\mathbf{K} & -\mathbf{M}^{-1}\mathbf{C} \end{bmatrix} \qquad \vec{B}_{\text{ss}} = \mathbf{M}^{-1}\vec{Q}$$

The input to the model, u, is an electric field level while the output, y_0, is the trailing edge flap deflection, given by $y_0 = \vec{C}'_{\text{ss}}\vec{x}$ where $\vec{C}'_{\text{ss}}$ is

$$\vec{C}'_{\text{ss}} = \frac{1}{s} \begin{bmatrix} \phi_1(1) & \phi_2(1) & \cdots & \phi_{10}(1) & 0 & 0 & \cdots & 0 \end{bmatrix}$$

Using this model, the frequency response of the system is obtained for comparison with the experimental data presented in Chapter 4.

2.3   Plate and Beam Model Comparisons

In the above derivation, the bender was modeled as a plate. In the previous study of this actuation mechanism, however, Spangler and Hall [45] modeled the bender as a beam. In their experiment, they noted that there was a visible amount of anticlastic bending present. While visible amounts of anticlastic bending are not expected from the present actuator because it is 72 times as stiff as that used by Spangler and Hall, it will still be of interest to see how the predictions of the model change when

allowing plate as opposed to beam degrees of freedom. Such a comparison is shown in Figures 2-5 and 2-6. Each of these plots are the result of the analytical model derived above. The plate solution was found by running the model using all ten mode shapes in Table 2.1 while the beam solution was found by running the model with only the first five mode shapes in Table 2.1. The fact that the beam solution has half as many modes is not a large source of error, because five modes were determined to be sufficient enough to guarantee numerical convergence of the model.

The magnitude plot in each figure gives the flap deflection in degrees for a given electric field applied to the bender. The absolute magnitudes of these plots are not the important point in this particular discussion, however. The characteristic that these figures attempt to highlight is the difference between the predictions of the model in using beam as opposed to plate mode shapes.

Figure 2-5 shows the frequency response comparison from 1 to 1000 Hz. Although the proposed actuator will never operate at such high frequencies, if feedback control is implemented with these actuators, it will be useful to know the location of high frequency dynamics. The fact illuminated by this figure is that by using the beam model, the presence of a pole and zero at approximately 800 Hz is not predicted.

A more important difference, however, is uncovered by examining the low frequency characteristics of the predicted actuator responses. In order to do this, a close up of their magnitudes at low frequency is presented in Figure 2-6. The beam model over-predicts the location of the first modal frequency by 2 Hz. However, this represents only a 1.7% error, and is not overwhelmingly significant. The more important difference between the two model predictions is that the beam model predicts a magnitude response 13% greater than the plate for frequencies below that of the first mode, indicating that it is important to account for the mechanism of anticlastic bending in predicting the response of the actuator at these low frequencies.

Overall, the beam and plate models follow the same general trends. Indeed, for general calculations, use of the beam model does provide acceptable results. However, if the detailed behavior of the actuator response is desired, a plate model becomes necessary.
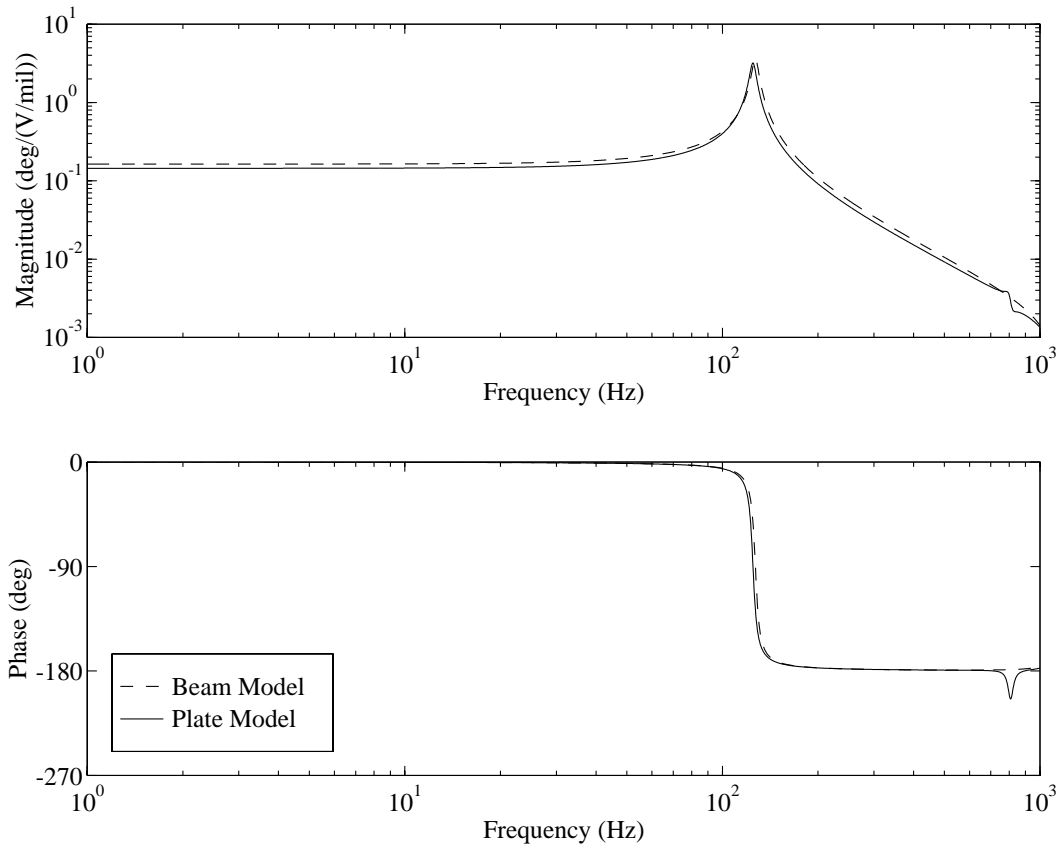
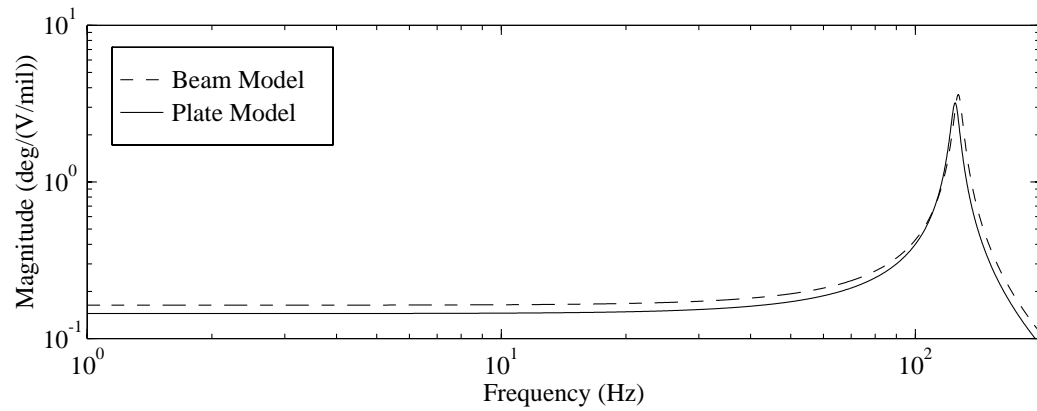**Figure 2-5:** Comparison of high frequency predictions of plate and beam analytic models.

Figure 2-6: Comparison of low frequency magnitude predictions of plate and beam analytic models.

Chapter 3

Actuator Design and Construction Issues

This chapter is concerned with the design and construction of an actuator consisting of a piezoelectric bender that is used to deflect a trailing edge servo flap on a helicopter blade. In order for such a design to be successful, efficient and dependable methods must be found to transform the bender energy into the servo-flap deflections. Spangler and Hall [45] designed and built the original prototype of this actuation mechanism. They used commercially available piezoelectric benders that were connected to a trailing edge flap using small hinges. The present study improves on this design in a number of ways. The most significant improvement is the use of flexures as opposed to hinges in the bender to flap attachment. A second improvement is in the use of a bender with tapered thickness properties. Tapering the bender increases its efficiency in actuating a vertical tip force while providing other beneficial inertial and size effects. A third major improvement is the implementation of a nonlinear amplifier to increase the maximum electric field applied to the bender by 50%. Each of these improvements is discussed in detail in this chapter.

3.1 Sizing the Actuator

While the volume of piezoelectric ceramic present determines the amount of energy available, the efficiency with which this energy is used depends on the geometry of the bender and the size of the lever arm chosen between the tip of the bender and the flap hinge. This section presents the design equations of the actuator using an impedance matching argument, and discusses the benefits provided by a bender with tapered properties. Furthermore, because the design of the actuator is fundamentally dependent on the necessary aerodynamic hinge moments, this section concludes by presenting an estimate of the required hinge moments to operate a servo-flap on a typical model rotor and the scaling laws used to relate the model and full-scale parameters.

The analytical derivation in Chapter 2 made the valid argument that the actuator is best modeled as a plate and not a beam. Unfortunately, closed form analytical solutions for plates with complicated boundary conditions are not easily obtained. Using the analytical model, a comparison between the approximate solution of the equation of motion for the case of plate and beam degrees of freedom was discussed in Section 2.3. While the effects of the anticlastic bending reduce the predicted magnitude response of the bender by approximately 13%, the solutions found with both sets of degrees of freedom follow the same trends. For this reason, a beam model is sufficient for use as a static design tool. Therefore, the derivation of the actuator design equations originally presented by Spangler and Hall [45] is utilized here to produce a preliminary design of the actuator.

3.1.1 The Impedance Matching Condition

The fundamental issue in designing the actuator rests in finding the configuration that maximizes the transfer of energy from the bender to the flap. The conversion of bender energy into flap deflection energy may be broken down into two main parts. One part is the transfer of piezoelectric ceramic strain energy into bender tip deflection energy, and the other part is the transfer of that tip deflection energy into

energy expended by deflecting the flap in the airstream. The former is discussed below in Section 3.1.2 on designing an efficient bender, and the latter is discussed in this section.

The hinge moment needed to deflect a flap increases with flap deflection, δ. This resistance to flap deflections can be modeled as a torsional spring, with spring constant, M_δ. The flap hinge moment is then

$$M_{\mathrm{H}} = M_\delta \delta \tag{3.1}$$

Two-dimensional airfoil theory is used to relate this spring constant to the aerodynamics of the airfoil as

$$M_\delta = \frac{1}{2}\rho U^2 c_{\mathrm{f}}^2 C_{\mathrm{H}_\delta} \tag{3.2}$$

where ρ and U are the density and free stream velocity of the fluid, c_{f} is the flap chord length, and C_{H_δ} is an aerodynamic coefficient reflecting the change in hinge moment per flap deflection. The value of C_{H_δ} for a servo flap located on a typical helicopter rotor blade is estimated in Section 3.1.3.

For the impedance matching argument presented in this section, it is useful to model the contribution of this flap spring force as a linear spring, k_δ, located at the tip of the bender, as shown in Figure 3-1. Also shown in Figure 3-1 is the specific cross-sectional geometry of most commercially available uniform benders. This cross-section consists of two piezoelectric wafers, sandwiching a middle shim. The thickness of each wafer is t_{p}, and the distance between their centers is h. A thickness parameter used to describe such uniform benders is defined as $n = h/t_{\mathrm{p}}$ and can never be less than unity.

The relation between the two spring constants, k_δ and M_δ, comes from realizing that the energy stored in each for a given flap deflection must be equal. This flap deflection energy is

$$V_\delta = \frac{1}{2}M_\delta \delta^2 = \frac{1}{2}k_\delta w_{\mathrm{A}}^2 \tag{3.3}$$

where w_{A} is the tip deflection of the bender. Assuming small angle flap deflections,
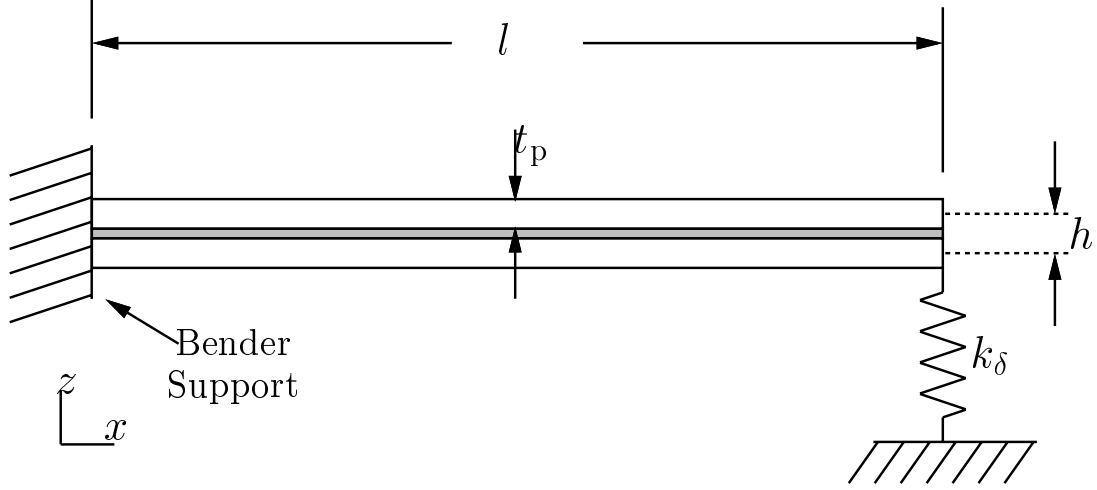
Figure 3-1: Schematic of uniform piezoelectric bender with tip flap spring.

the relationship between bender tip deflections and flap deflections is

$$\delta = \frac{w_A}{s} \tag{3.4}$$

where s is the lever arm distance, originally shown in Figure 1-1. Therefore, using Equations (3.2), (3.3) and (3.4),

$$k_\delta = \frac{M_\delta}{s^2} = \frac{\frac{1}{2}\rho U^2 c_f^2 C_{H_\delta}}{s^2} \tag{3.5}$$

Obviously, the spring stiffness, k_δ, is dependent on the air speed, U. When the airspeed goes to zero, the value of k_δ also goes to zero, and the structural model of the bender reduces to a cantilevered beam. For easy reference, when operating with zero airspeed, the bender will be referred to as "free". Conversely, when operating at a non-zero airspeed, the bender will be referred to as "constrained".

To relate the transfer of energy from the bender to the flap, it is necessary to express the constrained bender tip deflections, w_A, to those of the free bender, w_F. A constant vertical force, F, applied to the tip of the bender results in two different tip deflections for the constrained and free cases. They are

$$w_A = \frac{F}{k_\delta + k_B} \tag{3.6}$$

54

$$w_F = \frac{F}{k_B} \tag{3.7}$$

where k_B is the tip stiffness of the free bender. Since the force is the same for both cases, the relationship between the free and constrained tip deflection is

$$w_A = \frac{1}{1 + \frac{k_\delta}{k_B}} w_F \tag{3.8}$$

Substituting Equation (3.8) into Equation (3.3) gives the flap deflection energy as

$$V_\delta = \frac{1}{2} k_B w_F^2 \frac{\frac{k_\delta}{k_B}}{\left(1 + \frac{k_\delta}{k_B}\right)^2} \tag{3.9}$$

Because the tip deflection energy of the free bender is

$$V_F = \frac{1}{2} k_B w_F^2 \tag{3.10}$$

the flap deflection energy is identified as the product of the bender tip deflection energy and an impedance matching efficiency, η_q,

$$V_\delta = V_F \eta_q \tag{3.11}$$

This efficiency factor takes on a maximum value of 0.25 when $k_B = k_\delta$. This is the impedance matching condition originally described by Spangler and Hall [45]. By ensuring $k_\delta = k_B$, the maximum amount of the bender's tip deflection energy is converted into flap deflections.

The parameter used to enforce the impedance matching condition is the lever arm distance, s. The necessary value of this impedance matching lever arm is

$$s_{opt} = \sqrt{\frac{M_\delta}{k_B}} = \sqrt{\frac{\rho U_D^2 c_f^2 C_{H_\delta}}{2 k_B}} \tag{3.12}$$

where U_D is the design point airspeed.

Once the actuator is designed and built, all the design parameters are set. It

is therefore instructive to see how the flap deflections of the actuator change with airspeed. Dividing both sides of Equation (3.8) by the lever arm length gives the relation of flap deflections for the constrained and free case as

$$\delta_{\mathrm{A}} = \frac{1}{1 + \frac{k_\delta}{k_{\mathrm{B}}}} \delta_F \tag{3.13}$$

If the proper impedance match was made to the design point airspeed, the tip stiffness is

$$k_{\mathrm{B}} = \frac{\frac{1}{2}\rho U_{\mathrm{D}}^2 c_{\mathrm{f}}^2 C_{\mathrm{H}_\delta}}{s_{\mathrm{opt}}^2} \tag{3.14}$$

and the ratio of the bender and flap stiffness becomes

$$\frac{k_\delta}{k_{\mathrm{B}}} = \left(\frac{U}{U_{\mathrm{D}}}\right)^2 \tag{3.15}$$

Substituting Equation (3.15) into Equation (3.13) gives

$$\delta_{\mathrm{A}} = \frac{1}{1 + \left(\frac{U}{U_{\mathrm{D}}}\right)^2} \delta_F \tag{3.16}$$

At the design point, $U = U_{\mathrm{D}}$, the constrained flap deflection, $\delta_{\mathrm{A_D}}$, equals one half the free flap deflection. Normalizing Equation (3.16) by this design point flap deflection gives

$$\frac{\delta_{\mathrm{A}}}{\delta_{\mathrm{A_D}}} = \frac{2}{1 + \left(\frac{U}{U_{\mathrm{D}}}\right)^2} \tag{3.17}$$

which expresses the variation of the flap deflection from the design point as the airspeed changes.

3.1.2 Designing an Efficient Bender

As discussed in the previous section, choosing a properly impedance matched lever arm distance maximizes the conversion of energy from the bender to the flap. Therefore, the only additional way to increase the amount of energy converted into flap deflections is to increase the efficiency with which the bender converts its strain en-

ergy into useful tip deflection energy. It is therefore logical to define a bender efficiency as

$$\eta_{\mathrm{B}} = \frac{\frac{1}{2} k_{\mathrm{B}} w_{\mathrm{F}}^2}{V_{\mathrm{B}}} \qquad (3.18)$$

where the numerator is the amount of energy transferred into tip deflections and V_{B} is the strain energy of the bender. V_{B} is given by

$$V_{\mathrm{B}} = \frac{1}{2} \int_V E\Lambda^2 \, dV \qquad (3.19)$$

where E is the Young's Modulus and Λ is the actuation strain discussed in the last chapter. The volume integral of Equation (3.19) is taken only over the volume of piezoelectric ceramic present in the bender. This efficiency is a function of the geometry of the bender.

Efficiency of a Uniform Bender

For a commercially available bender, possessing uniform properties over its length, such as the one shown in Figure 3-1, the strain energy is

$$V_{\mathrm{B}} = E\Lambda^2 l t_{\mathrm{p}} \qquad (3.20)$$

The tip stiffness for this bender is

$$k_{\mathrm{B}} = \frac{3EI}{l^3} \qquad (3.21)$$

If the bending inertia of the middle shim is neglected, the moment of inertia is

$$I = \frac{t_{\mathrm{p}}^3}{6} \left(1 + 3n^2\right) \qquad (3.22)$$

If the bond between the two sides of a bender is perfect, allowing no shear lag, the induced strain of the piezoelectric ceramics may be modeled as a moment acting at the tip of the bender [11]. Therefore, the bending moment at each point in the beam

is

$$M = E\Lambda t_\text{p}^2 n \tag{3.23}$$

From elementary beam theory, the resultant tip deflection of the free bender is then

$$w_\text{F} = \frac{Ml^2}{2EI} \tag{3.24}$$

Using Equations (3.20), (3.21), (3.22), (3.23) and (3.24), the uniform bender efficiency reduces to

$$\eta_\text{B} = \left(\frac{3}{4}\right)\left(\frac{3n^2}{1+3n^2}\right) = \eta_\text{t}\eta_\text{c} \tag{3.25}$$

The first efficiency, η_t, equals 3/4 and represents the fraction of energy a beam in bending converts into vertical tip deflections. For a uniform beam, it is a constant. However, as discussed in the next section, by tapering the properties of the bender, the value of η_t can be increased.

The second efficiency in Equation (3.25), η_c, represents the local efficiency of the bender in actuating a moment. It is not a function of the geometry or the boundary conditions of the bender. In actuating a force or displacement, 100% efficiency from an infinitesimal element of a piezoelectric ceramic is attained when it is allowed to strain without constraint. However, actuating a piezoelectric plate in bending forces the stress (and strain) distribution to vary linearly through the thickness, with one half in tension and one half in compression. Because of this, the work done by the material becomes more inefficient the farther it is from the surface of the bender. This loss in efficiency from the interior piezoelectric material is the cause of the efficiency factor, η_c. This factor increases from a value of 0.75 when $n = 1$ to a value of 1 when $n = \infty$. It reflects the fact that as the two piezoelectric plates of the uniform bender move farther apart, the induced strain over the thickness of the plate becomes less constrained and the efficiency of the bender increases.

When no shim is present between the two halves of the bender, $n = 1$ and $\eta_\text{c} = 0.75$. For a uniform bender, this makes the overall bender efficiency $\eta_\text{B} = 0.5625$. By increasing the thickness of the middle shim, both of these efficiencies increase. As a
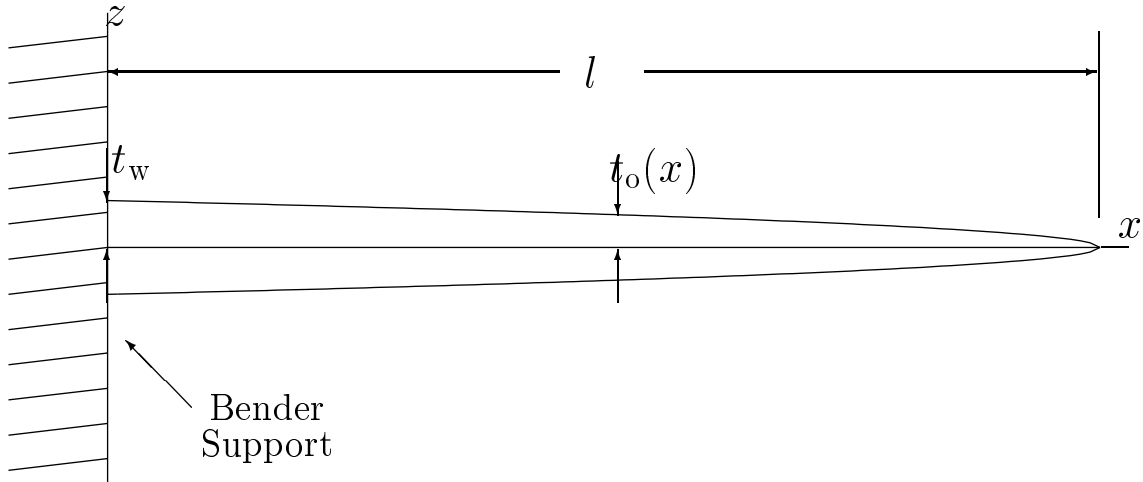
Figure 3-2: Schematic of piezoelectric bender with optimum thickness taper.

note, in the theoretical limit where $n = \infty$, $\eta_c = 1$ and the bender efficiency increases to 75%. However, this overestimates the true efficiency that would result because the bending inertia of the shim was assumed to be negligible in Equation (3.22). Therefore if the bending inertia of the shim becomes large enough to invalidate this assumption, the expression given by Equation (3.22) should be modified to include the effects from the shim.

Efficiency of a Tapered Bender

In the expression for the uniform bender efficiency, Equation (3.25), η_t was described as the efficiency of the bender in converting its strain energy into vertical tip deflections. For a bender with constant lengthwise thickness properties, this efficiency is a constant $3/4$. However, tapering the properties yields values of η_t greater than $3/4$ and, in the theoretical limit, makes $\eta_t = 1$. Tapering the bender properties also creates more room for bender tip deflections and a center of gravity located closer to the leading edge of the airfoil. All of these issues are discussed in this section.

Theoretically, there exists an exact thickness distribution that raises η_t from $3/4$ to 1. It will be instructive to find this distribution. The bender analyzed here is shown schematically in Figure 3-2. This theoretical bender is modeled as two tapered
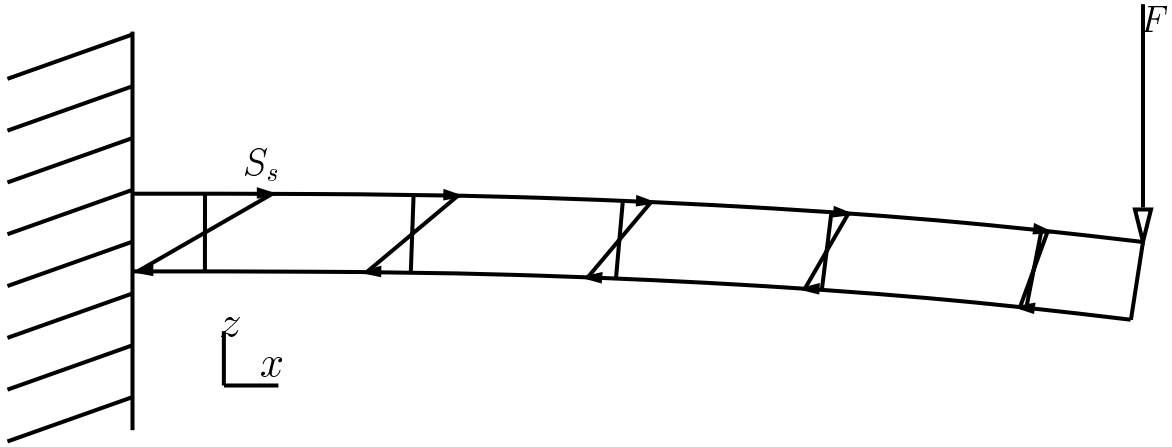
59

Figure 3-3: Distribution of strain in a uniform bending structure.

piezoelectric plates bonded directly to one another. For simplicity, no middle shim was included in the make-up of this bender.

The goal is to determine the effect a certain thickness distribution has on the bender's ability to actuate a tip deflection. However, due to the non-uniform thickness properties of this bender, presenting a closed form analytical solution for this problem would overshadow, with mathematical complexity, the governing motivation behind why a tapered bender is useful. A straightforward way to understand the problem recognizes that by Maxwell's Law of Reciprocal Deflections [6], predicting the tip deflections caused by a piezoelectric actuation strain is equivalent to predicting the strain caused by an applied tip force. The strain at any point from a tip force is

$$S = \frac{Mz}{EI(x)} = \frac{F(l-x)z}{EI(x)} \tag{3.26}$$

which expresses that the strain at any cross-section of a beam in bending varies linearly with z. This is illustrated in Figure 3-3 for a uniform cantilevered beam with an applied tip force. Also shown in Figure 3-3 is the strain distribution at five different cross-sectional locations. As shown, the amount of strain over a cross-section decreases upon moving toward the tip. By the Law of Reciprocal Deflections, this implies that the piezoelectric material at the tip of a uniform bender contributes very

little in actuating a tip displacement.

Because the amount of strain at any cross-section is proportional to the strain at the beam surface, the change of the surface strain with x is a valid way to measure how the overall cross-sectional strain changes with length. The moment of inertia of the tapered beam of Figure 3-2 is

$$I(x) = \frac{2t_o^3(x)}{3} \tag{3.27}$$

Substituting t_o in for z in Equation (3.26) and using Equation (3.27), the surface strain is expressed as

$$S_s = \frac{3F\,(l-x)}{2Et_o^2(x)} \tag{3.28}$$

By keeping the surface strain constant over the length of the beam, the amount of induced strain from the tip force is maximized, and, reciprocally, the amount of tip deflection from a given piezoelectrically actuated strain is also maximized. A constant surface strain is attained by prescribing the thickness distribution as

$$t_o(x) = t_w\sqrt{1 - \frac{x}{l}} \tag{3.29}$$

The definition of the bender efficiency, Equation (3.18), and strain energy, Equation (3.19), still hold for this tapered bender. The strain energy is

$$V_{B_s} = E\Lambda^2 t_w \int_0^l \sqrt{1 - \tfrac{x}{l}}\, dx = \frac{2E\Lambda^2 t_w l}{3} \tag{3.30}$$

and the tip stiffness and free bender deflection, found using elementary beam theory, are

$$k_{B_s} = \frac{Et_w^3}{l^3} \tag{3.31}$$

$$w_{F_s} = \frac{\Lambda l^2}{t_w} \tag{3.32}$$

Substituting Equations (3.30), (3.31) and (3.32) into Equation (3.18) shows that the

efficiency of this square root tapered bender is 75%. However, this 75% efficiency is accounted for by considering that the value of η_c, which is a local efficiency, independent of geometry, is 75% when there is no middle shim in the bender. Therefore, by introducing the square root taper, the efficiency, η_t, has increased by 33% to its maximum possible value of one.

Another benefit of the bender with the square root taper is that its center of gravity is closer to the leading edge of the airfoil. Since having weight near the trailing edge of an airfoil leads to undesired effects such as flutter instabilities [5], any modification that shifts the center of gravity of these actuators toward the leading edge is very useful.

The final benefit from using a tapered bender is one related to the size constraint on the design. The thickness of the airfoil at the chord location corresponding to the tip of the bender governs how thick the actuator may be. The actuator is constrained to be small enough to fit within this thickness while also allowing enough room for the necessary bender tip deflections. Tapering the properties of the bender decreases its thickness at the tip, greatly relieving this thickness constraint in the design.

Benders with square root tapers are not feasible, because it is almost impossible to apply a voltage over such a bender that will create a uniform electric field throughout. However, by constructing a bender with uniform piezoelectric plates, separated by a linearly tapered shim, a great deal of the improved efficiency is realized. This tapered bender design is shown in Figure 1-1. The equation for the curvature of the bender at any cross-section is

$$w''(x) = \frac{M(x)}{EI(x)} = \frac{6\Lambda\left(1 + \frac{t_s(x)}{t_p}\right)}{\left(t_p + \frac{1}{2}t_s(x)\right)\left(1 + 3\left(1 + \frac{t_s(x)}{t_p}\right)^2\right)} \tag{3.33}$$

where the shim thickness, t_s, is now a linear function of x. By integrating this function numerically, the tip deflections and stiffness may be calculated. Performing an iterative search of different shim thicknesses yields a design maximizing the efficiency of the bender. For example, by using an aluminum shim with a wall thickness of
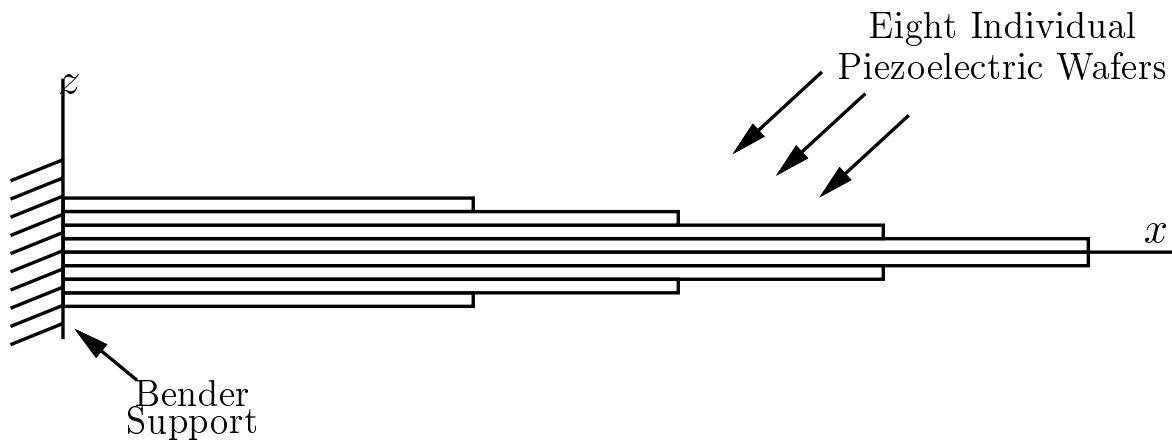
Figure 3-4: Concept of the layered piezoelectric bender.

0.068 in that tapers to a point at the bender tip, along with two piezoelectric ceramic plates, each 0.030 in thick, an efficiency of 74.8% was calculated. Of course, by using a middle shim to achieve the tapered geometry, in addition to the increase in efficiency from tapering the bender, this calculated efficiency also reflects the extra efficiency gained from having a non-zero shim thickness over the length of the bender.

The construction of a workable bender with a tapered shim was not possible, due to time constraints. Therefore, a second, simpler method was used to create a bender with a tapered cross-section. This consisted of a layered geometry with eight thin piezoelectric wafers possessing different lengths, as shown in Figure 3-4. Integrating numerically and iterating to find the optimum set of lengths which maximized the efficiency led to the actuator used in the experiments presented in Chapter 4. The dimensions of this actuator are presented in Section 4.1. No middle shim was used in its construction.

In actuality, obtaining efficiencies from this layered bender on the order of $70 - 75\%$ becomes impossible when the extra stiffness from the electrodes present on each of the individual wafers is taken into account. However, if the the extra stiffness from any electrodes present on the piezoelectric wafers is neglected, a 70.6% efficiency is calculated for this bender. This is a 26% improvement over the efficiency of a uniform bender with no middle shim.

Although manufacturing benders with tapered thickness properties is more diffi-

63

cult than producing uniform benders, considering all of the benefits they provide in the particular application of deflecting a trailing edge flap on a helicopter blade, it makes sense to include them in all future designs of this actuation method.

Basic Actuator Design Procedure

From the above discussion, a basic actuator design procedure can be formulated. The thickness of the airfoil at the bender tip, T_{tip}, presents a major thickness constraint on the design of the actuator because the tip thickness of the bender, t_{bt}, must be small enough to fit within this gap while also providing enough room for its necessary displacements. This thickness constraint is expressed as

$$t_{\text{bt}} + 2w_{\text{A}} < T_{\text{tip}} \qquad (3.34)$$

Another constraint on the design is the allowable bender length. This constraint is a structural one. The bender is clamped directly to the main airfoil spar, as shown in Figure 1-1. The length of the bender must be small enough to ensure that the loss of main spar material at the clamp location does not seriously affect the structural integrity of the blade.

The design process begins by choosing a desired flap deflection size. By Equation (3.4), this is translated into an equivalent bender tip deflection using an initial guess of the lever arm size. Using Equation (3.34), the allowable bender thickness is found. Following the efficiency discussion above, reasonable piezoelectric wafer and shim thicknesses are then chosen. The last bender parameter specified is its length. It is chosen long enough such that the desired bender tip deflections may be achieved without seriously affecting the structural integrity of the airfoil, as discussed above. In a separate calculation, a design point airspeed is identified and the flap spring stiffness, M_δ, is estimated according to the discussion of Section 3.1.3. The impedance matching condition, Equation (3.12), is then enforced to find the necessary lever arm length, s. Using this updated lever arm length, the resultant flap deflections are checked to ensure that they are large enough. If they are not, the dimensional prop-

Table 3.1: Target model rotor parameters

Model Parameter	Value
Rotor Blade Radius, R	4.5 ft
Rotational Speed, Ω	780 RPM
Blade Cross-Sectional Shape	RC 410
Blade Chord, c	4.454 in
Blade Thickness	10%

erties of the bender are adjusted and the process repeated. By iterating with this procedure, the necessary actuator dimensions may be set so that it yields the maximum amount of useful control authority over the aerodynamics in which it operates, while not substantially affecting the structural characteristic of the rotor blade.

3.1.3 Actuator Force Requirements and Scaling

The design of an actuator capable of operating at a design point location on a target helicopter blade depends, from the impedance matching arguments of Section 3.1.1, on finding an accurate estimate of the expected flap hinge stiffness, M_δ, at that point. The target rotor for this study was a model scale rotor used for operation in Freon. Its parameters are specified in Table 3.1. In this section, the hinge moments expected along the blade span of this rotor are estimated in order to determine the necessary design point flap stiffness. Furthermore, since the fundamental concern in the model scale studies of this actuator is to determine useful information about its full-scale applications, the scaling laws relating model and full-scale actuator parameters are also presented.

Servo-Flap Hinge Moment Estimates

In the discussion of Section 3.1.1, the hinge moment was expressed as a function of only the flap deflection angle, δ. However, a more accurate representation of the hinge

moment is

$$M_{\mathrm{H}} = \frac{1}{2}\rho U^2 c_{\mathrm{f}}^2 \left\{ C_{\mathrm{H}_\alpha}\alpha + C_{\mathrm{H}_\delta}\delta \right\} \tag{3.35}$$

where α is the airfoil angle of attack and C_{H_α} is an aerodynamic coefficient expressing the sensitivity of the hinge moments to changes in angle of attack. This equation expresses the fact that while the hinge moments increase with flap deflection, the angle of attack of the airfoil also affects the hinge moment magnitudes. Because the aerodynamics of a helicopter rotor are so complex, the values for the angle of attack and the hinge moment coefficients, C_{H_α} and C_{H_δ}, are not constant. The value of C_{H_δ} used in Equation (3.2) must therefore be an average aerodynamic coefficient relating the sensitivity of the hinge moment at a certain design speed to changes in the flap deflection angle. Furthermore, because of the dependence of the hinge moments on angle of attack, the choice of this average value must also take into account the effects from non-zero angles of attack.

Glauert [19] determined an analytical expression for the expected hinge moments using thin airfoil theory. Defining the flap chord length as $c_{\mathrm{f}} = E_{\mathrm{f}}c$, the aerodynamic coefficients are

$$
\begin{aligned}
C_{\mathrm{H}_\alpha} &= \frac{-C_{\mathrm{L}_\alpha}}{\pi E_{\mathrm{f}}^2} \left[\left(\frac{3}{2} - E_{\mathrm{f}}\right)\sqrt{E_{\mathrm{f}}(1-E_{\mathrm{f}})} - \left(\frac{3}{2} - 2E_{\mathrm{f}}\right)\left(\frac{\pi}{2} - \arccos\sqrt{E_{\mathrm{f}}}\right) \right] \\
C_{\mathrm{H}_\delta} &= \frac{2\left(a_2 C_{\mathrm{H}_\alpha} - b_0 C_{\mathrm{L}_\alpha}\right)}{C_{\mathrm{L}_\alpha}} \\
b_0 &= \frac{2(1-E_{\mathrm{f}})\sqrt{E_{\mathrm{f}}(1-E_{\mathrm{f}})}}{\pi E_{\mathrm{f}}^2} \left[\frac{\pi}{2} - \arccos\sqrt{E_{\mathrm{f}}} - \sqrt{E_{\mathrm{f}}(1-E_{\mathrm{f}})} \right] \\
a_2 &= \frac{1}{2}C_{\mathrm{L}_\alpha}\left(1 - \frac{2}{\pi}\left[\arccos\sqrt{E_{\mathrm{f}}} - \sqrt{E_{\mathrm{f}}(1-E_{\mathrm{f}})}\right] \right)
\end{aligned}
$$

For airfoils with very large aspect ratios (> 20), such as rotor blades, the lift curve slope is approximated as $C_{\mathrm{L}_\alpha} = 2\pi$.

Abbott and Von Doenhoff [1] present a simple formula for the hinge moment coefficient as

$$M_{\mathrm{H}} = \frac{1}{2}\rho U^2 c_{\mathrm{f}}^2 \left\{ \frac{\partial C_{\mathrm{H}}}{\partial C_{\mathrm{L}}}C_{\mathrm{L}} + \frac{\partial C_{\mathrm{H}}}{\partial \delta}\delta \right\} \tag{3.36}$$

The value of C_{L} is plotted in [1] as aerodynamic data as a function of collective angle

Hinge Moment Stiffness (in-lb/in/rad)

—— Thin Airfoil Theory (Alpha = 0)
• Abbott and Von Doenhoff (Alpha = 0)
·—· Abbott and Von Doenhoff (Alpha = 5 deg)
× XFOIL with Mach and Viscous Effects (Alpha = 0)
+ XFOIL with Mach and Viscous Effects (Alpha = 5 deg)
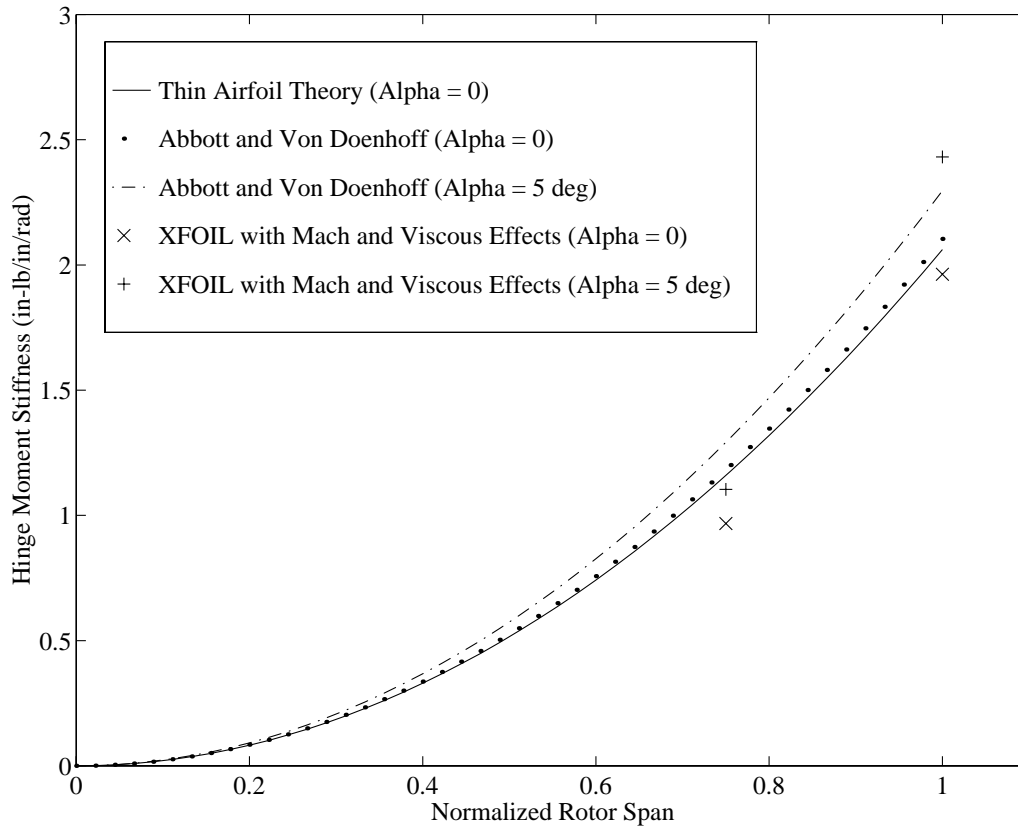
Normalized Rotor Span

Figure 3-5: Calculated hinge moment stiffness with blade span for a rotor in hover, using several computation methods.

of attack, α, and flap deflection, δ and values for $\frac{\partial C_\mathrm{H}}{\partial C_\mathrm{L}}$ and $\frac{\partial C_\mathrm{H}}{\partial \delta}$ are found with thin airfoil theory. For an airfoil with a 20% flap to chord ratio, $\frac{\partial C_\mathrm{H}}{\partial C_\mathrm{L}}$ and $\frac{\partial C_\mathrm{H}}{\partial \delta}$ are -0.09 and -0.65, respectively. Abbott and Von Doenhoff remark, however, that while thin airfoil theory can be used to get values for hinge moments, the accuracy of these numbers is sometimes poor due to viscous effects at the trailing edge.

An additional source used to verify hinge moment magnitudes was XFOIL [12], a 2-D panel method accounting for compressibility and viscous forces. The hinge moment stiffness magnitudes, M_δ, calculated using the above three sources are plotted in Figure 3-5 as a function of span location on a blade of the target rotor operating in hover.

Considering the 0 deg angle of attack data first, the agreement between the calculations of Glauert and Abbott and Von Doenhoff is good. This is expected, since

both are based on thin airfoil theory. However, they serve as a check on one another, validating the hinge moment magnitudes predicted. The numbers found with XFOIL for 0 deg angle of attack are smaller than the predictions found with thin airfoil theory. The viscous forces on an airfoil tend to increase the boundary layer thickness, which lowers the necessary hinge moments.

The hinge moments for a 5 deg collective angle of attack were also calculated using the methods of Abbott and Von Doenhoff and XFOIL. As shown, at the tip, XFOIL no longer underestimates the hinge moment magnitudes found with thin airfoil theory. This increase can be attributed to compressibility effects that are largest at the tip of the rotor.

In this study, the goal is to demonstrate that a piezoelectrically actuated servo-flap can operate effectively at the highest dynamic pressure present on a typical rotor system. This would usually imply impedance matching to the aerodynamics at the rotor tip. However, because of the tip loss associated with a helicopter rotor, the actuator in the present study was designed to operate at the 90% span location of the target rotor blade. From Figure 3-5, to operate at the 90% span location, a reasonable estimate of the flap hinge stiffness, M_δ, is 1.8 in-lb/in/rad.

Usually this value for M_δ can immediately be applied to the actuator design process described in Section 3.1.2. However, as discussed below in Section 3.3.1, extra stiffness is added from the flexure mechanism, which couples the bender and flap deflections. Because of this fact, the value of M_δ used in the design of the actuator for this study is slightly larger than 1.8, as discussed in Section 3.3.1.

Model Scaling Laws

Before an aerodynamic device is implemented into a full-scale prototype, a model of it and the aerodynamic structure it is a part of is typically built and tested. The purpose of building a model is to obtain data that can predict how the device will operate in the full scale prototype. However, in order to insure that tests of a model accurately characterize the full-scale prototype, the designer must ensure that the aerodynamic conditions for the model and full-scale tests are dynamically similar.

Two aerodynamic flows are dynamically similar when identical types of forces are parallel and related by a constant scale factor [17]. This is done by setting equal appropriate non-dimensional groups of the model and full scale flows.

The appropriate groups to use are found by non-dimensionalizing the governing equations of motion of the phenomenon under study. In the present case, by treating the hinge moment applied by the bender as an externally applied moment, the dynamic equation of motion of the flap is

$$I_{\mathrm{F}}\frac{\partial^2 \delta}{\partial t^2} + \frac{1}{2}\rho U^2 c_{\mathrm{f}}^2 C_{\mathrm{H}_\delta}\delta = C_p \frac{E\Lambda t_{\mathrm{p}}^2 s}{l} \tag{3.37}$$

where C_p is a constant factor, depending on the geometry of the bender (tapered or uniform). According to the Buckingham Π Theorem [17], to non-dimensionalize this equation, three dimensional parameters must be chosen such that by combining them into certain ratios yields factors with dimensions equal to the equation's *primary dimensions*. The primary dimensions in the above equation are length, mass and time. For this reason, the density, rotor blade radius, R, and free stream velocity are chosen as the dimensional parameters used to non-dimensionalize Equation (3.37).

The lengths in Equation (3.37) are easily non-dimensionalized by normalizing them by the rotor blade radius, so that $\bar{c}_{\mathrm{f}} = c_{\mathrm{f}}/R$, $\bar{t}_{\mathrm{p}} = t_{\mathrm{p}}/R$, $\bar{s} = s/R$ and $\bar{l} = l/R$. The non-dimensional flap mass moment of inertia and the time variable are

$$\bar{I}_{\mathrm{F}} = \frac{I_{\mathrm{F}}}{\frac{1}{2}\rho R^4} \tag{3.38}$$

$$\bar{t} = \frac{tU}{R} \tag{3.39}$$

Substituting these non-dimensional parameters into Equation (3.37) gives

$$\bar{I}_{\mathrm{F}}\frac{\partial^2 \delta}{\partial \bar{t}^2} + \bar{c}_{\mathrm{f}}^2 C_{\mathrm{H}_\delta}\delta = \frac{E}{\frac{1}{2}\rho U^2}\frac{C_p \Lambda \bar{t}_{\mathrm{p}}^2 \bar{s}}{\bar{l}} \tag{3.40}$$

This equation shows that in order to perform meaningful tests of a geometrically scaled model of this actuator, the non-dimensional mass moment of inertia and the

modulus to dynamic pressure ratio,

$$\frac{E}{\frac{1}{2}\rho U^2} \tag{3.41}$$

must be equal in the model and full-scale tests. Because Young's modulus, E, for piezoelectric ceramics does not change between the model and full-scale, this implies that the dynamic pressure for the model and full-scale flows must be equal.

In addition to the above requirements on the scaling between model and full scale, because compressibility forces play a major role in the aerodynamics of a rotor system, the Mach number represents the last non-dimensional parameter that should be equal between model and full-scale in order to ensure dynamic similarity.

Setting equal the model and full-scale values of the non-dimensional parameters specified above will yield the necessary scaling laws. Geometric similarity requires that all dimensions scale according to

$$R_S = \frac{R_f}{R_m} \tag{3.42}$$

where, in the following, the subscripts "m" and "f" denote model and full-scale parameters and the subscript "S" denotes a constant factor representing the full-scale to model ratio. Furthermore, enforcing the Mach number requirement forces the velocities to scale as

$$U_S = \frac{U_f}{U_m} = \frac{a_f}{a_m} \tag{3.43}$$

where a is the speed of sound of each aerodynamic medium. And, finally, in order to have equal dynamic pressures, the model and full-scale fluid densities must be related as

$$\frac{\rho_m}{\rho_f} = \frac{U_f^2}{U_m^2} = U_S^2 \tag{3.44}$$

The inertial scaling between model and full-scale requires only that the non-dimensionalized mass moment of inertia, defined in Equation (3.38), be the same for both cases. Because of this, the inertial scaling for these tests may be satisfied independently of the other scaling laws derived above.

In the present study, the frequency behavior, flap deflections and achievable hinge moments will be important parameters to relate between the model and a full-scale helicopter. The flap deflections are the ratio of the lever arm length to bender tip deflections. Because the model is geometrically scaled, this ratio and therefore the flap deflections will be equal between model and full-scale.

The frequency scaling law is found by using the definition of the velocity at any point on the rotor as

$$U_{\mathrm{S}} = \frac{U_{\mathrm{f}}}{U_{\mathrm{m}}} = \frac{R_{\mathrm{f}}\Omega_{\mathrm{f}}}{R_{\mathrm{m}}\Omega_{\mathrm{m}}} \tag{3.45}$$

$$\frac{\Omega_{\mathrm{f}}}{\Omega_{\mathrm{m}}} = \frac{U_{\mathrm{S}}}{R_{\mathrm{S}}} \tag{3.46}$$

In helicopter control, it is typical to normalize the frequencies associated with a rotor in terms of its rotational speed, Ω, thereby expressing frequencies as a number of cycles per revolution of a rotor blade. For example, the bandwidth of the actuator of the present study can be specified as the frequency of the first structural mode. The value of the first modal frequency will change between model and full-scale tests according to Equation (3.46). However, its normalized value, *i.e.*, the modal frequency divided by the rotational frequency of the rotor, will be the same in the model and full scale tests. This is discussed further in Section 4.2.2.

The hinge moment scaling law is found by considering the full-scale to model ratio of any of the terms in Equation (3.37). For example, taking the ratio of the static hinge moment term gives

$$\frac{M_{H_{\mathrm{f}}}}{M_{H_{\mathrm{m}}}} = \frac{(c_{\mathrm{f}})_{\mathrm{f}}^2 (C_{\mathrm{H}_\delta})_{\mathrm{f}}}{(c_{\mathrm{f}})_{\mathrm{m}}^2 (C_{\mathrm{H}_\delta})_{\mathrm{m}}} \tag{3.47}$$

where the subscripts outside the parenthesis stand for full or model scale. The hinge moment coefficient, C_{H_δ}, is dependent only on the flap chord ratio [19]. Therefore, if the same flap chord ratio is used in model and full-scale (which is necessary due to geometric scaling), the hinge moments scaling law becomes

$$\frac{M_{H_{\mathrm{f}}}}{M_{H_{\mathrm{m}}}} = R_{\mathrm{S}}^2 \tag{3.48}$$

All of the above scaling laws are summarized in Table 3.2. Each scaling relation-

Quantity	Ratio of Full-Scale to Model
Geometry	R_{S}
Velocity	U_{S}
Density	$\frac{1}{U_{\mathrm{S}}^2}$
Frequency	$\frac{U_{\mathrm{S}}}{R_{\mathrm{S}}}$
Hinge Moment	R_{S}^2

Table 3.2: Scaling laws from model to full-scale.

ship in the second column of this table represents the ratio of the full scale to model scale value. The relationships expressed in Table 3.2 are the correct scaling laws to ensure dynamic similarity for rotating model scale tests of the piezoelectric actuator.

The actuator in the present study was designed for incorporation into the model rotor specified in Table 3.1. This is a Mach-scaled rotor, but the dynamic pressures associated with it are approximately 35% smaller than those of a full-scale helicopter. This will not affect the measurements performed in the present study, because it consists only of bench top experiments, independent of any specified aerodynamic environment but it will be an important fact to take into account when the full-scale capabilities of the present actuator are determined. In the above discussion on the estimated hinge moments, the designed actuator location was specified as the 90% span point on the target model rotor in Freon. If the actuator in the bench top experiment is properly impedance matched to this span location, by Equation (3.13), the deflections measured on the bench will be twice those expected at the 90% span location on the target model rotor in Freon. If the dynamic pressures were equal between model and full-scale, the bench top measurements would also be twice as large as the expected flap deflections from a full-scale actuator located at the 90% span point on an operational helicopter. However, because the full-scale dynamic pressures are larger than the model scale, Equation (3.13) must be used with an appropriate value chosen for k_δ to relate the model and full-scale flap deflections.

This will be discussed further in Section 4.2.3.

3.2   The Nonlinear Circuit

The poling and coercive field limits for a piezoelectric ceramic differ by at least a factor of two. It is possible to take advantage of this fact by using a nonlinear circuit to drive the piezoelectric bender. The motivation behind this circuit and its design is presented in this section.

From the discussion of Section 2.1.1, determining an exact value for the poling and coercive fields is not possible, because the definition of each is not fixed. It is possible to apply electric fields in the poling direction that are very large indeed. The field level in the poling direction is limited only by the electrical breakdown of the piezoelectric material, which occurs between 80 and 100 V/mil [41]. For this reason, it is not unusual to apply poling fields as high as 60 V/mil over a piezoelectric ceramic. The coercive field, on the other hand, is extremely dependent on the actuation frequency. For example, its value at DC is specified as 15 V/mil, while for AC operation at 60 Hz, it is given as 30 V/mil [41]. In most cases, the operation of the actuators for helicopter control will not occur at frequencies near DC. For this reason, a coercive field limit of 30 V/mil is allowable in the operation of the piezoelectric bender for helicopter control.

If a pure sinusoidal voltage is applied to a piezoelectric ceramic, to avoid depoling it, its amplitude is constrained to ensure the resultant applied electric field remains less than the coercive field limit. The relationship of such an applied voltage signal to the poling and coercive voltages, V_P and V_C, is shown in Figure 3-6(a). Obviously, using such an input driving signal would not take advantage of the capacity of piezoelectric ceramics to withstand high electric fields oriented in the poling direction.

A common method of making use of the difference in poling and coercive field limits in the operation of piezoelectric stacks, which provide only extension and compression, is to add a DC bias, V_0, in the poling direction and actuate with a sinusoid of appropriate amplitude, such that both the poling and coercive voltage limits are
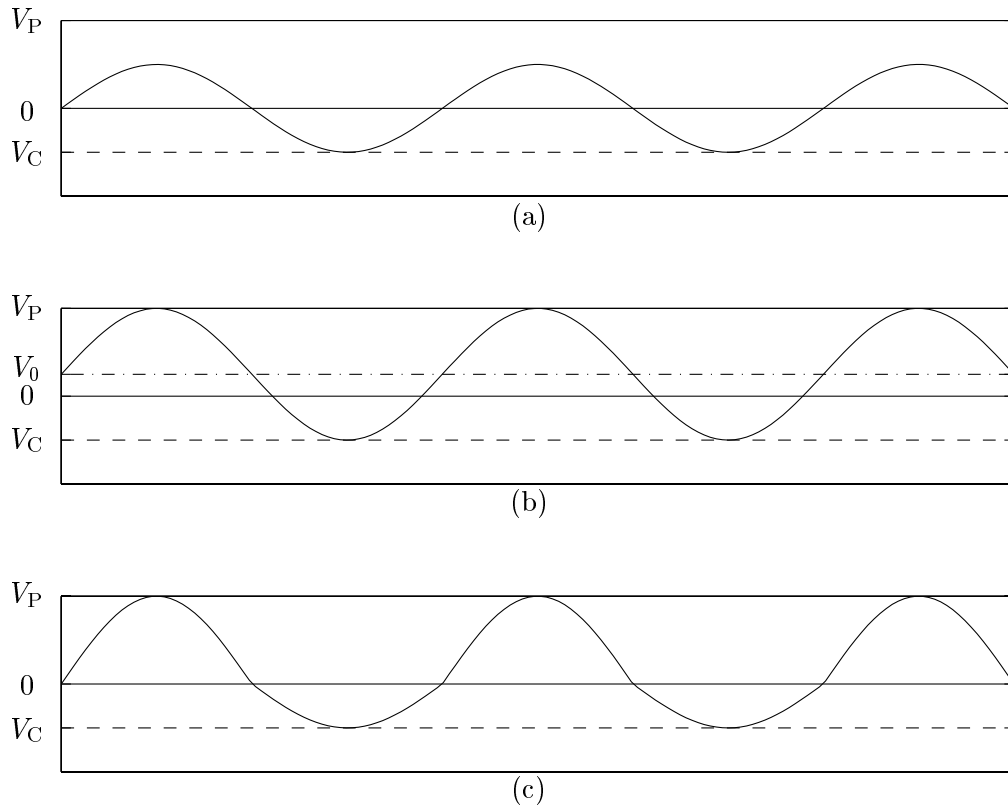
Figure 3-6: Piezoelectric ceramic input voltage driving signals.

reached, as shown in Figure 3-6(b). However, if such an input is used to actuate a bender, the maximum DC bias that can be applied is also limited by the coercive field. Therefore, if the ratio of the poling to coercive field limits is set greater than three, this limit on the DC bias will also place a limit on the amplitude of the applied AC signal so that the resultant electric field remains below the coercive limit over its entire period of oscillation. When the ratio of the poling to coercive field limits is significantly greater than three, these limits will constrain the applied electric field to levels far below the maximum allowable poling field constraint. For this reason, this is also not an optimum way to drive a piezoelectric bender.

A better way to take advantage of the antisymmetric voltage limits of the piezoelectric bender is to construct a nonlinear circuit such that an input sinusoid, V_{in}, produces the trace shown in Figure 3-6(c). Such a trace is obtained by constructing
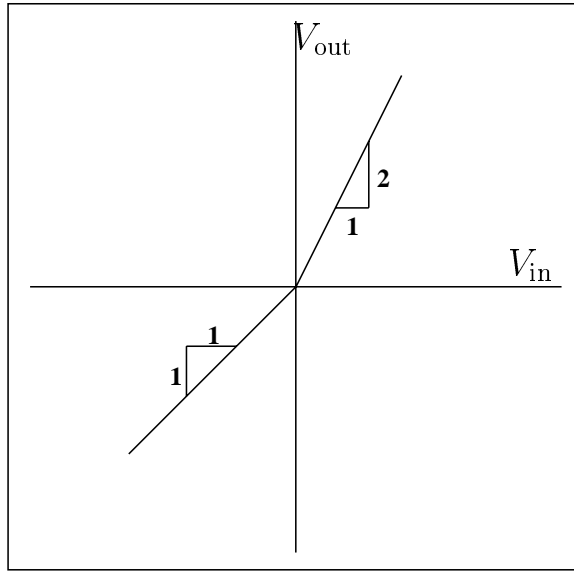
Figure 3-7: Input to output characteristic of nonlinear amplifier.

the nonlinear amplifier so that it has the input to output voltage characteristic shown in Figure 3-7.

As discussed in Section 3.1.2, the stress and strain vary linearly through the thickness of a structure in bending, with one half in tension and the other in compression. In light of the fact that the electric fields in the poling and coercive directions actuate compression and tension in the transverse direction, respectively, it is clear that at any given time in the operation of the bender, one half will have an electric field oriented in the poling direction, and the other half will have an electric field oriented in the coercive direction. Therefore, in order to implement the above described nonlinear circuit in the operation of a bender, two nonlinear amplifiers with input to output voltage characteristics similar to Figure 3-7 are needed, one for each half of the bender.

In order to create the necessary input to output voltage characteristic of each nonlinear amplifier, diodes were used in the make-up of the circuit. When forward biased, a diode may be modeled as an infinitely conductive short circuit, while a reverse biased diode behaves like an open circuit. Ideally, the break between the short and open circuit regimes of a diode would occur when the voltage difference
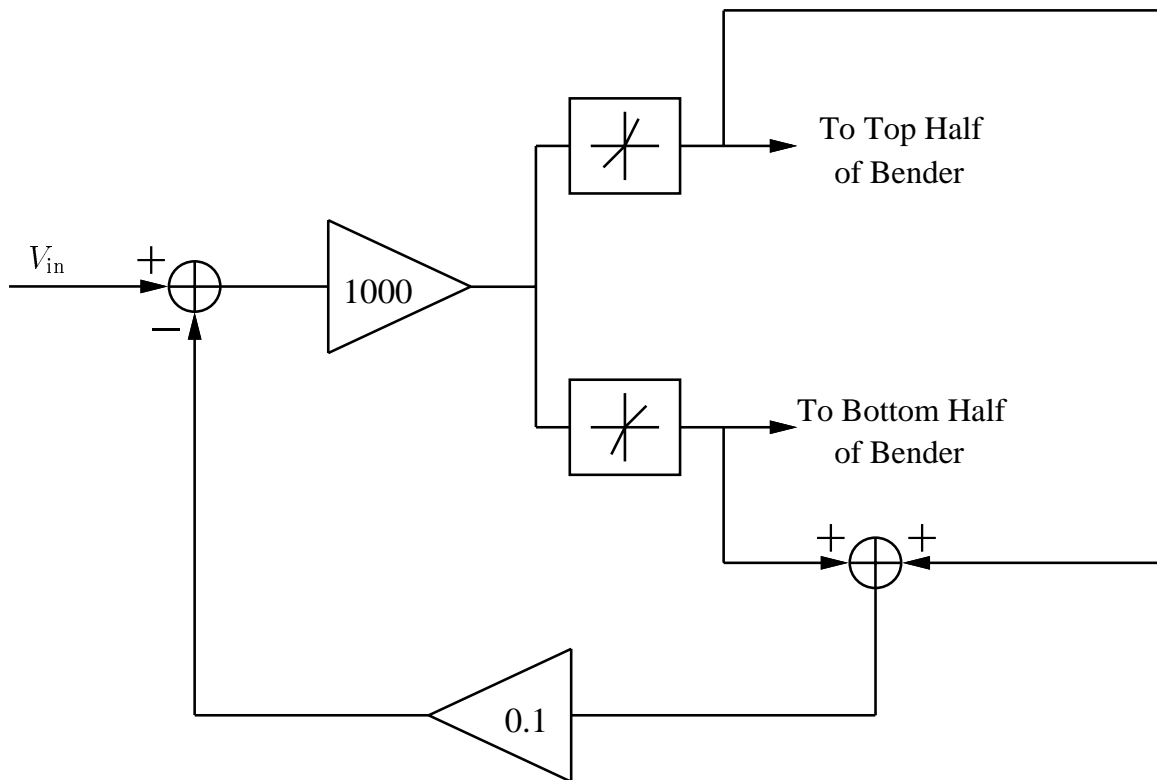
Figure 3-8: Block diagram of nonlinear circuit with feedback linearization.

across the diode changed signs. In actuality, however, when the diode is forward biased, it cannot be assumed to be infinitely conductive until the voltage difference across it exceeds approximately 0.6 V. The input to output voltage characteristic of Figure 3-7 shows the change in slopes of the input to output characteristic to occur at the origin. However, the presence of the non-zero 0.6 V activation voltage of the diodes moves the point where the slopes change away from the origin, which distorts the desired input signal trace of Figure 3-6(c). This distortion was eliminated using feedback linearization. By summing the output of the two nonlinear amplifiers, feeding a fraction of that signal back to the input, and introducing a large linearizing gain, the distortion was virtually eliminated. This feedback loop is shown in Figure 3-8 and the actual circuit used in this study is presented in Appendix B.

The circuit in Appendix B is set up for operation between poling and coercive field limits that differ by a factor of two. As discussed at the beginning of this section, it is

possible to operate the bender using the field limits of 60 and 30 V/mil. However, for conservative reasons, in the present study the applied poling and coercive electric field limits were limited to 40 and 20 V/mil, respectively. In the experiments presented in the next chapter, these limits were never exceeded. It is important to realize this when predicting the achievable performance of the actuator from the bench top measurements, as discussed in Section 4.2.3.

If the nonlinear circuit discussed in this section were not implemented, to avoid depoling the ceramic, an applied bender input voltage signal similar to that shown in Figure 3-6(a) would be necessary. However, if the poling and coercive field limits differ by a factor of two, use of the nonlinear circuit increases the average applied electric field by 50%, which will significantly increase the actuated response of the bender.

3.3 Design and Fabrication of the Flexure Mechanism

The most critical part to succeeding in actuating a trailing edge flap with a bender is to find a way to effectively connect the bender to the flap, while providing three separate degrees of freedom for proper operation.

Spangler and Hall used hinges in their design [45]. Not only are hinges a source of some mechanical backlash in the system, they were not feasible for the present design, due to its small scale. A better way to provide for the degrees of freedom is to use flexures. This was done by creating a part consisting of the three separate flexures in a very specific arrangement. The cross-section of the first generation flexure mechanism is shown in Figure 3-9. As shown, the flexure mechanism includes the aerodynamic control surface, three flexures, as well as two surfaces used to bond the flexure mechanism to the bender and to the airfoil's top surface. Besides the obvious advantage of using flexures as opposed to hinges, another distinct advantage of this design is that the lever arm distance, s, is now set precisely upon fabrication of the part.
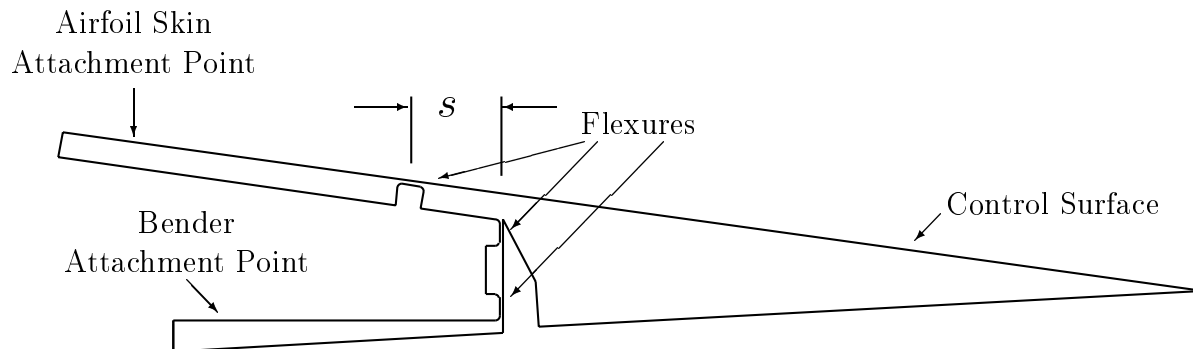
Figure 3-9: Geometry of first generation flexure mechanism.

The flexure mechanism is manufactured by hot pressing a piece of Delrin, using precision machined dies. Delrin is an acetal resin, made by Dupont, with exceptional fatigue properties. It has a sharp melting point at 347 F, a modulus of elasticity of 450,000 psi, a tensile strength of 10,000 psi, and a specific gravity of 1.42 [13]. As discussed in the next chapter, some problems existed with Delrin's bond integrity to the bender. For this reason, other materials might be investigated for better bonding properties, while retaining the strength and fatigue properties of Delrin.

3.3.1   Geometric Stiffening

Obviously, the use of flexures adds additional stiffness to the system. To insure that this extra stiffness did not seriously detract from the operation of the actuator, the summed contribution of the stiffnesses from the three flexures was specified to remain less than 10% of the hinge moment stiffness, M_δ.

Each flexure was modeled as a torsional spring with a stiffness of

$$k_i = \frac{E_\mathrm{d} I_i}{l_i},$$

(3.49)

where i is the flexure number, identified in Figure 3-10, l_i is the flexure length, the moment of inertia is

$$I_i = \frac{t_i^3}{12}$$

(3.50)

78
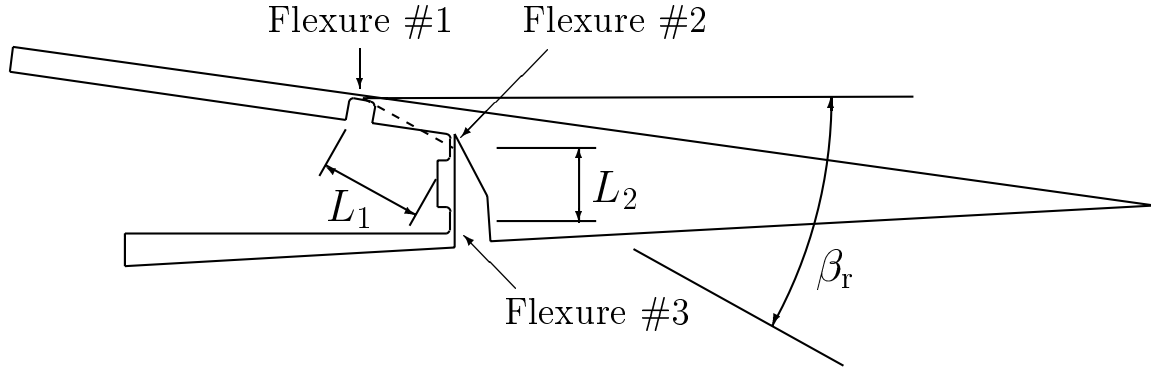
Figure 3-10: Effect of flexure mechanism geometry on its stiffness.

and t_i is the flexure thickness. To determine the overall flexure mechanism stiffness, the stiffnesses of the three flexures cannot simply be added because there are geometric constraints relating the deflection undergone by each flexure. Figure 3-10 shows the important geometric relation between each of the flexures. Assuming the bender tip moves in a purely vertical direction, the relative kinematics were analyzed and expressions for the strain energy in each of the flexures was obtained. The linearized form of these expressions is

$$V_1 = \frac{1}{2} k_1 \delta^2 \tag{3.51}$$

$$V_2 = \frac{1}{2} k_2 \left\{ \left[1 + \frac{L_1}{L_2} \sin \beta_\mathrm{r} \right] \delta \right\}^2 \tag{3.52}$$

$$V_3 = \frac{1}{2} k_3 \left(\frac{L_1}{L_2} \sin \beta_\mathrm{r} \right)^2 \delta^2 \tag{3.53}$$

where L_1, L_2 and the rigid angle, β_r, are defined in Figure 3-10, δ is the flap deflection and k_1, k_2 and k_3 are given by Equation (3.49). For the first generation flexure mechanism, $L_1 = 0.124$ in, $L_2 = 0.058$ in, and $\beta_\mathrm{r} = 36$ deg. What this analysis shows is that because of such a large non-zero rigid angle, β_r, the rotations undergone by flexure #2 are 2.2 times greater than those of flexure #1, making the energy lost in that middle flexure five times as great. This is enough to seriously reduce the effectiveness of the flexure mechanism. For this reason, the final design of the flexure mechanism possessed the cross-section shown in Figure 3-11, where $\beta_\mathrm{r} = 0$. Using this configuration, Equations (3.49) – (3.53) predict a total flexure mechanism stiffness of
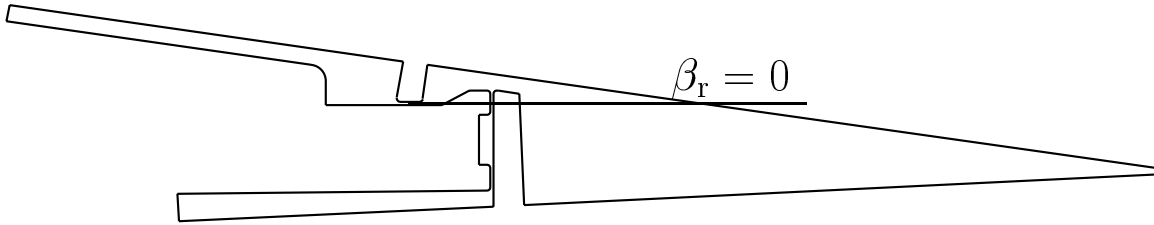
Figure 3-11: Final design of flexure mechanism.

0.16 in-lb/in/rad with flexures 0.004 in thick and 0.030 in long.

In Section 3.1.3, the design point flap hinge stiffness was specified as 1.8 in-lb/in/rad. The flexure mechanism adds 0.16 in-lb/in/rad of stiffness to this value. Therefore, rounding the sum of these two stiffnesses, the flap deflection stiffness, M_δ used in the design of the actuator for this study was specified as 2.0 in-lb/in/rad.

3.3.2 Fabrication

The flexure mechanism dies were machined out of 2024 Aluminum. Because of the special geometry of the flexure mechanism, three separate dies were needed to press the part. The lines detailing the cross-section of the flexure mechanism in Figure 3-11 also represent the relative cross-sectional geometries and alignment of the three dies used at the final stage of the hot press procedure. Cross-sectional views of the flexure mechanism dies are shown in Figures 3-12 and 3-13.

A hydraulic press with plates that can be heated to a desired temperature is used for the hot press. The bottom and side dies are placed on the bottom plate of the press. A 0.030 in thick rectangular piece of Delrin is place between the two dies as shown in Figure 3-12. The bottom plate and the two dies are heated up to 347 F. Using bolts, the side die is pressed against the bottom die to form flexures #2 and 3 as well as the bender attachment surface. A triangular cross-section wedge of Delrin is then placed onto the bottom die as shown in Figure 3-13. The top plate of the press is heated to 347 F, and the top die is placed on dowel line-up pins and pressed down upon the other two dies forming the desired flexure mechanism part. The dies are then cooled and separated, yielding the finished flexure mechanism.
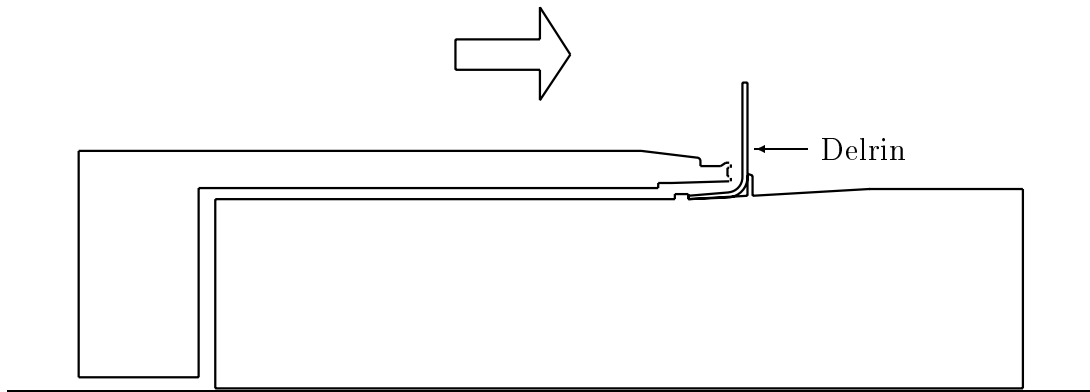
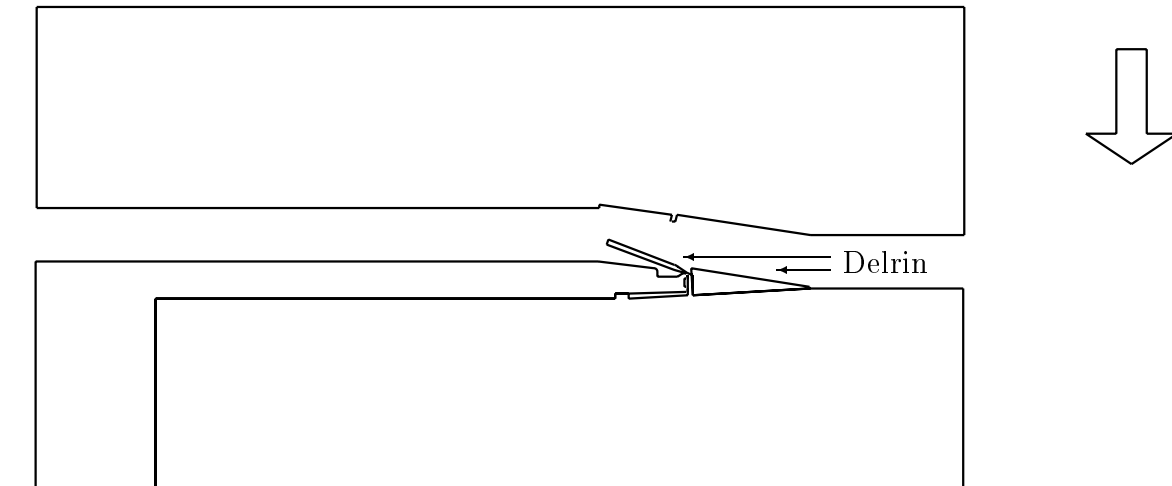**Figure 3-12:** Initial press: Side and bottom flexure mechanism dies.

Figure 3-13: Final press: Top, bottom and side flexure mechanism dies.

For the hot pressing operation to work, the dies have to come together with less than 0.001 in of error. This requires machining the flexure dies to absolutely no more than approximately 0.005 in of error and, once the machining is complete, using steel shims on the order of 0.001 in to adjust the final relative position of the dies. While the machining of flexure mechanism dies requires a great amount of precision, once made, the fabrication of a large number of flexure mechanisms can easily be accomplished.

As a final note, because the flexure mechanism specified above has a flap made of solid Delrin, a relatively dense substance, it will have a significant effect on the dynamics of the actuator. Specifically, as will be shown in the experimental data presented in the next chapter, the inertia due to the Delrin flap will substantially reduce the first modal frequency of the actuator. For this reason, in future designs, additional steps should be added to the above fabrication process that modify the cross-section of the flap, perhaps by removing a large portion of the interior Delrin and replacing it with a honeycomb stiffener. The effects of the large flap inertia will be discussed further in Section 4.2.2.

Chapter 4

Bench Test Experimental Results and Discussion

Before the proposed actuator can be implemented into an operational helicopter, its force and deflection characteristics must be demonstrated. The goal of this research, therefore, was to demonstrate the capabilities of the actuator on the bench top. This chapter presents the experimental set-up and results of such a bench top experiment.

4.1   Experimental Set-Up

The integration of an actuator inside a helicopter blade has associated with it a fundamental size constraint. For this reason, the dimensions of the bench test article were constrained to those of the target airfoil specified in Section 3.1.3. A cross-section of the bench test section is shown in Figure 4-1. The base of the bench test article consisted of plexiglass, with surfaces machined for clamping the piezoelectric bender and affixing the flexure mechanism at an angle corresponding to the airfoil's trailing edge top surface. The flexure mechanism was pressed out of Delrin using the method described in Section 3.3.2 and attached to the base with a cyanoacrylate adhesive. The flexure mechanism's spanwise dimension measured 1.736 in. Terminal strips affixed at the front of the article were used to anchor down the bender's leads. Note that the flexure mechanism and bender in the bench test article are oriented

upside-down from the conventional airfoil reference frame. This was done only for convenience in bonding the flexure mechanism to the base.

A layered construction such as that described in Section 3.1.2 was implemented to maximize the efficiency of the bender. The actual cross-sectional dimensions of this actuator are presented in Figure 4-2. Shown in this figure are the eight individual piezoelectric wafers and the glue layers separating each. The front (*i.e.*, closest to the leading edge of the airfoil) 0.5 in of the piezoelectric bender is reserved for clamping. The filled arrows on the left side of the bender represent the poling vectors of the individual piezoelectric wafers. The leads drawn on the left side show the wiring used to actuate the multi-morph in bending. The voltages V_{top} and V_{bot} are the voltage signals applied to the top and bottom halves of the piezoelectric bender. Using the nonlinear circuit described in Section 3.2, these two signals oscillate between the poling and coercive limits of 300 and 150 volts during operation at the maximum applied voltage. To operate in bending and avoid de-poling, it is necessary for these voltage signals to be out of phase, so that, for example, as V_{top} reaches the poling limit of +300 volts, V_{bot} must reach the coercive limit of +150 volts. Note that the layered bender shown demonstrates the extra benefit gained from gaining access to the electrodes between each wafer in that smaller voltages are needed for operation than if the electric field was generated by just making electrical contact to the outer surfaces of the bender.

The piezoelectric wafers are Type 850, obtained from American Piezo Ceramics, Inc. Comparison of the properties of Type 850 piezoelectric ceramic with more common PZT-type ceramics reveals that it has properties closely resembling those of PZT-5A. The cross-section of each wafer consisted of 0.0075 in of piezoelectric ceramic, sandwiched by two 0.001 in nickel electrodes. The width of each wafer measured 1.5 in and the length dimensions were chosen to maximize efficiency according to the discussion of Section 3.1.2, while providing a tip stiffness of 200 lb/in/in. The electrodes were modeled as pure nickel, rigidly bonded to each wafer for the analytical calculations of the bender tip stiffness. Electrodes of this thickness were used only because of their availability. Because the electrodes take up space and add unneces-
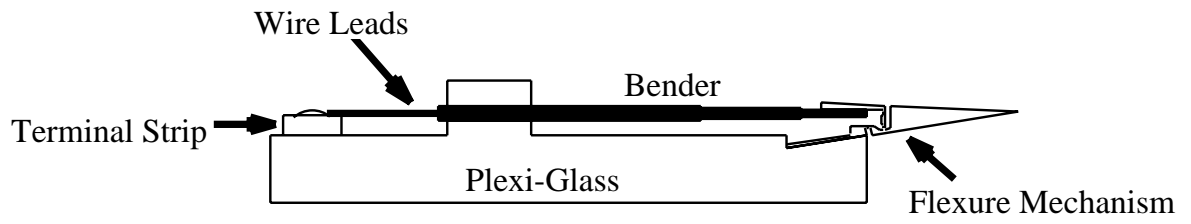
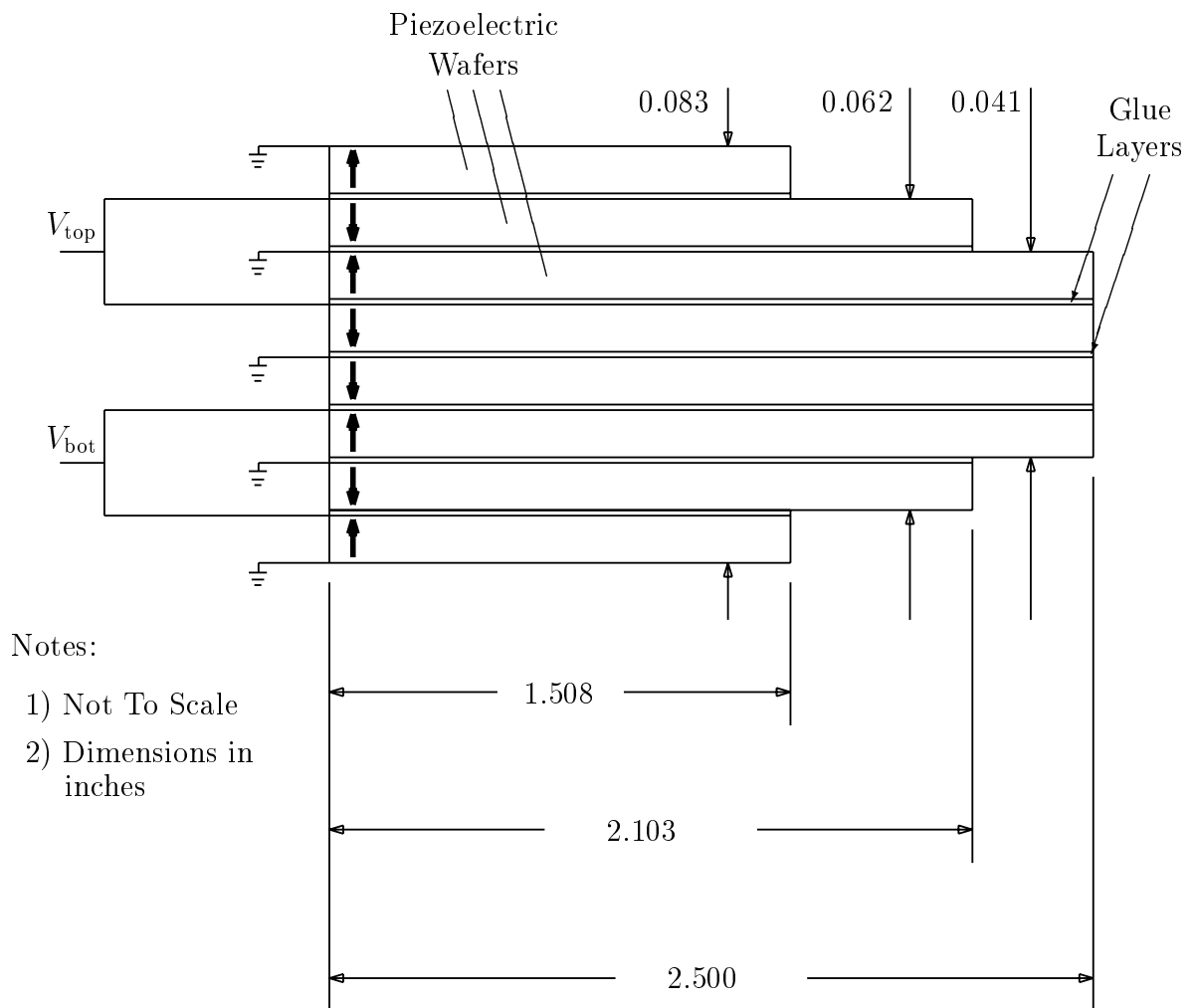**Figure 4-1:** The bench test article.

Figure 4-2: Schematic of piezoelectric actuator used in experiment.

sary bending inertia to the multi-morph, in future designs, it is worthwhile to use the thinnest electrode layer that is feasible.

EPO-TEX Epoxy 907 served as the adhesive between the piezoelectric wafers. The bond layer using this adhesive measured 0.001 in. To provide electrical contact between each layer of the bender, small oval shaped copper electrodes were inserted between each layer, at the front end of the bender. These electrodes are 0.0015 in thick, approximately 1 in long and 0.25 in wide. Wire leads were soldered to each electrode. After completing the lay-up, these wires and copper electrodes were potted in a silicone rubber adhesive sealant, RTV 118. All other free edges of the actuator were insulated with M-Coat-A polyurethane coating. These measures were taken to guard against arcing.

Air arcs at an electric field of approximately 80 V/mil. During the operation and poling of this actuator, an electric field of 40 V/mil was never exceeded. However, grease and dust particles are sometimes present on the sides of a piezoelectric ceramic, promoting the chances of arcing. When an arc does occur, a deposit is occasionally left behind that possesses some conductivity. If this deposit connects the two sides of a piezoelectric ceramic, it becomes unable to sustain a charge. Applying proper insulating materials, such as silicone and polyurethane, helps avoid these arcing problems.

The leads at the front of the piezoelectric bender were originally potted in epoxy mixed with cotton powder. This led to a severe arcing of the individual piezoelectric wafers, making the actuator virtually unusable. The arcing was hypothesized to have occurred in the epoxy potting material. By dissolving away the epoxy, cleaning up the electrodes at the front and repotting in silicone, six of the eight piezoelectric wafers were brought back into service. Only the two innermost wafers were not in service for these experiments. As discussed in Section 3.1.2, the efficiency of a piezoelectric wafer in actuating a moment increases with its distance from the neutral axis. Because of this, the reduction incurred from turning off the inner two wafers was minimal. As a check, the analytical model of Chapter 2 was run to compare the change in frequency response by turning off these two wafers. These computations predicted only an 8%

loss in flap deflection magnitudes by operating with only the outer six as opposed to all eight piezoelectric wafers. This eight percent factor will be accounted for in Section 4.2.3 when the operating capability of the actuator is summarized.

As discussed in Section 3.1.3, the actuator used was designed to operate at the 90% span location of a properly scaled model rotor in Freon. In addition, from Section 3.3.1, for an actuator to operate effectively at this location, it should be designed such that the bender is impedance matched to a combined flexure mechanism and aerodynamic flap hinge stiffness of 2.0 in-lb/in/rad. The tip stiffness of the bender specified above was calculated as $k_B = 200$ lb/in/in. Using the impedance matching condition, Equation (3.12), these stiffness magnitudes force the lever arm length, s_{opt}, to be 0.1 in.

The nonlinear circuit discussed in Section 3.2 was used to drive the bender. It was built on a Global Specialties Proto-Board, Model 203A. The nature of the nonlinear driving signal necessitated two amplifiers to operate the top and bottom sides of the bender. KEPCO Bipolar Operational Power Supply/Amplifiers, Model BOP 1000M, were used as these high voltage amplifiers.

The input and output devices changed depending on the measurement being made. For hinge moment measurements and general operation, a Philips PM 5191 Programmable Function Generator provided the input to the nonlinear amplifier while a Nicolet Digital Oscilloscope Model 2090 displayed and stored the signal traces. For frequency response identification, a Tektronix 2630 Fourier Analyzer calculated the transfer functions while driving the system with a random, frequency banded input signal. The signal analyzer takes an FFT of the input and output of the system being identified and ratios their autospectra to find the transfer function.

A Keyence LB-11/70 Laser Displacement Sensor measured the flap deflections. The laser was positioned vertically above the flap, measuring the displacements of the flap tip. The flap deflections were calculated using the small angles formula, dividing this laser measurement by the radius from the flap hinge to the laser spot location. During the experiments, the beam from the laser was not exactly perpendicular to the radius. However, a geometric analysis done on the accuracy of the flap deflections
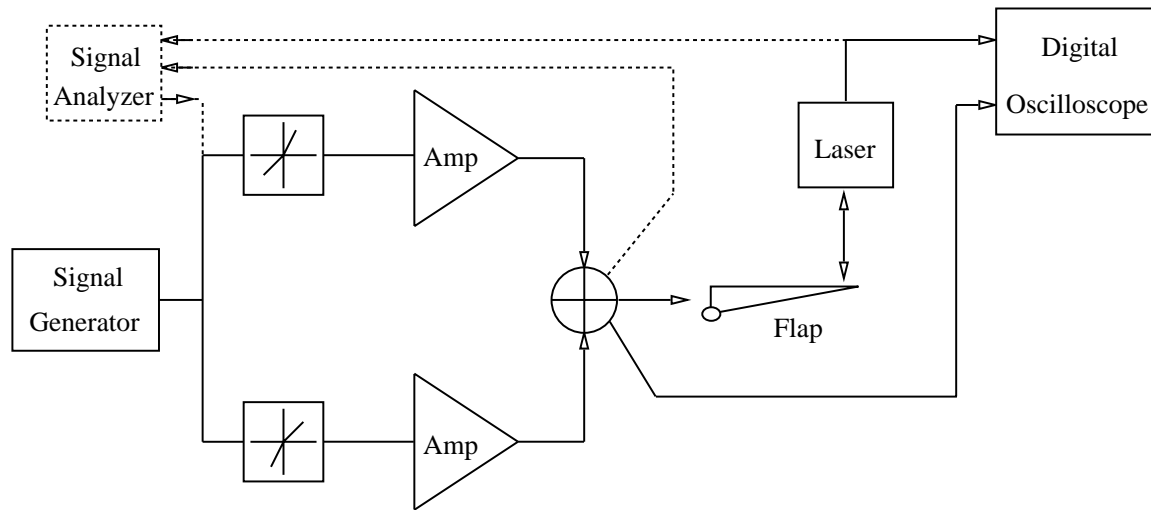
Figure 4-3: Block diagram of actuation and measurement system.

measured with this set-up indicated that the laser position used added little error to the measurements. The instrumentation block diagram for the experiment is shown in Figure 4-3.

4.2   Data Presentation and Discussion

The flap deflections and forces created by the actuator are the characteristics of interest in this study because their product represents the energy created in operating the flap. In addition, since rotor control involves actuation at high frequencies, knowledge of the behavior of these characteristics as a function of frequency is also important. For these reasons, a frequency response of the system showing the dynamics of the first two modes and data addressing the achievable hinge moments of the actuator constituted the measurements taken in this bench top experiment.

4.2.1   Unmodeled Actuator Response

The modeling process depends, fundamentally, on making correct assumptions about the system of study. Piezoelectric ceramics exhibit a number of well-known nonlinearities in their operation. Because the linear model derived in Chapter 2 will not

account for these effects, they will cause variations between the experimental and predicted actuator response. Furthermore, in preliminary tests of the actuator, two additional sources of unexpected behavior were observed. The first involved extra compliance identified in the flexure mechanism and its bond to the bender. The second was a realization that the actual tip stiffness of the bender was almost a factor of two smaller than expected from the design calculations. This section will provide a preliminary discussion of these effects while Sections 4.2.2 and 4.2.3 will treat the specific implications that they have on the measured data.

The equations of motion derived in Chapter 2 govern the behavior of a linear, small-signal, layered piezoelectric multi-morph. However, the nonlinearities, such as hysteresis, creep and nonlinear strain behavior all affect the operation of the bender used in these experiments [10, 38, 40]. The presence of hysteresis was discussed in Section 2.2.2 on damping. However, the additional effects of creep and nonlinear strain behavior require some preliminary explanation.

Creep is a time dependent change in the observed strain of a material [22]. There was a non-trivial amount of creep observed during the tests of the actuator and, unfortunately, the effects from this seriously handicapped the collection of hinge moment data. The implications of this are discussed in Section 4.2.3

It is expected that the effects of creep are important only for frequencies less than 1 Hz. Because of this, creep should not pose many problems in helicopter N/rev control. However, it remains a question as to how it impacts the effectiveness of collective rotor control. Because creep is a strain dependent mechanism, the amount of time dependent deflection seen when actuating against a constraint, *i.e.*, a blocked condition, is small. Therefore, it may be true that actuation in an airstream will minimize the effect of low frequency creep, making collective rotor control achievable using these actuators.

The resultant strain in a piezoelectric bender for a given applied electric field is governed by the value of the d_{31} coefficient. Calling this parameter a coefficient, however, is a bit of a misnomer because its value is not truly constant. It is a function of the electric field and temperature of the ceramic.
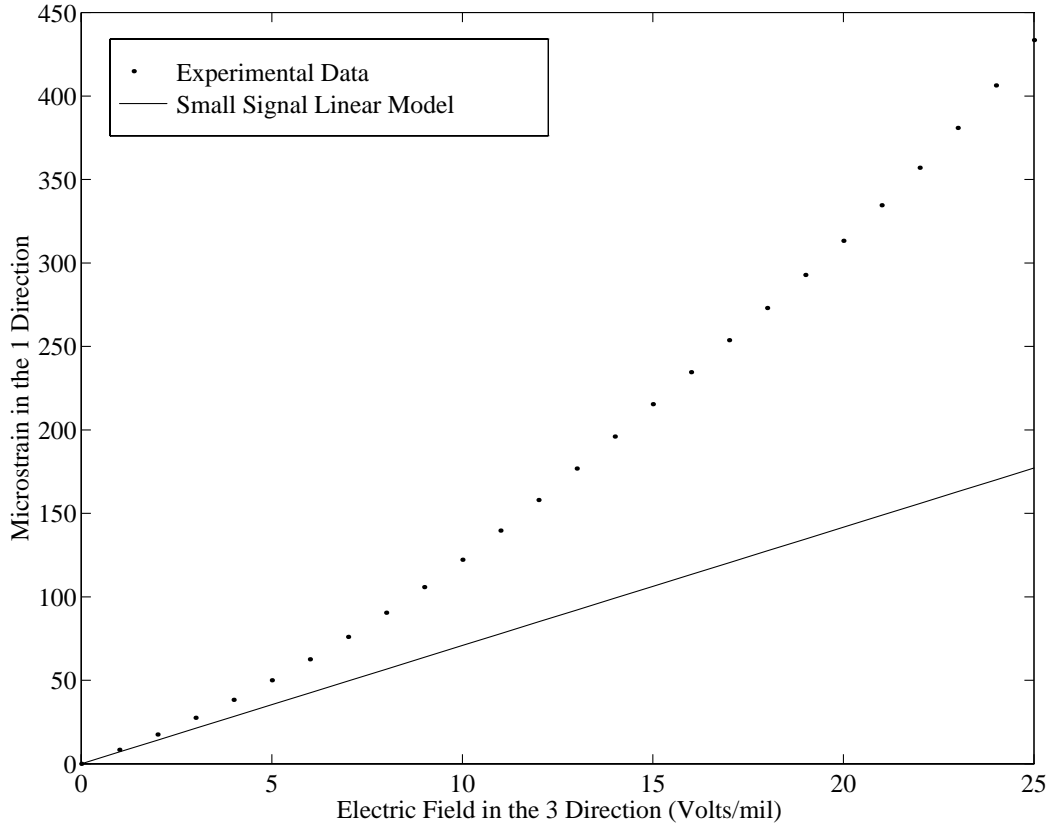
Figure 4-4: Microstrain vs electric field (From Crawley and Anderson [10]).

The value of the d_{31} coefficient increases with electric field. This trend is shown in Figure 4-4, taken from Crawley and Anderson [10]. This figure shows the strain measured at different electric field levels for actuation of a piezoelectric ceramic at 0.1 Hz. The slope of this strain to field curve at any point corresponds to the d_{31} coefficient at that field level. The d_{31} coefficient specified in most piezoelectric ceramic catalogs corresponds to the slope of the curve at low field levels, *i.e.*, less than 1 V/mil. Included in this figure is this small signal linear d_{31} relationship. As is clearly shown, at 0.1 Hz, the amount of strain for large electric fields is two to three times that of the linear model.

The explanation for this effect is related to the discussion on dipoles of Section 2.1.1. In that discussion, it was explained that upon poling a piezoelectric ceramic, the dipoles rotate to align themselves with the poling field. That expla-

nation implied that upon removal of the poling field, the dipoles remained set in the material. However, not all dipoles completely align nor stay aligned with the poling field direction upon completion of the poling process. Therefore, when large electric fields are applied during the operation of a ceramic, additional dipole rotation and motion occurs, yielding larger strain values than predicted with a linear model.

The strain generated by additional rotation of the dipoles takes longer to occur than that caused by the motion of those dipoles permanently aligned in the poling field direction. Therefore, as the frequency of actuation increases, this additional strain mechanism contributes less to the overall resultant strain of the material. For high enough frequencies, the linear small signal strain to field relationship is recovered. Indeed, this is how the strain to electric field relationship for the small signal model is actually measured.

The use of the nonlinear circuit described in Section 3.2 will allow the application of electric fields up to 40 V/mil in the operation of the bender, increasing the contribution of the above strain mechanism. However, it is expected that this effect will become less prevalent as the actuation frequency increases.

A second factor that may have a small impact on the size of the strain levels in the ceramic is the temperature. Data from [38] shows that for PZT-5A, the d_{31} coefficient can change by as much as 4% for a temperature change from 15 to 25 C. There are two sources from which heat can enter an oscillating piezoelectric ceramic. One source is the hysteresis of the material. As discussed in Chapter 2, the amount of hysteresis in the material is a measure of the energy lost in one cycle of operation. The second source is electrical energy lost in the dissipation of current oscillating through the ceramic. The energy lost from both of these effects must be converted into heat. A 4% change in strain is not a large difference but, as will be discussed in the next section, in identifying a system with a number of nonlinear mechanisms, the response measured becomes extremely sensitive to the system parameters at the time the data is acquired. Therefore, even small temperature changes could have a noticeable effect on the identified response.

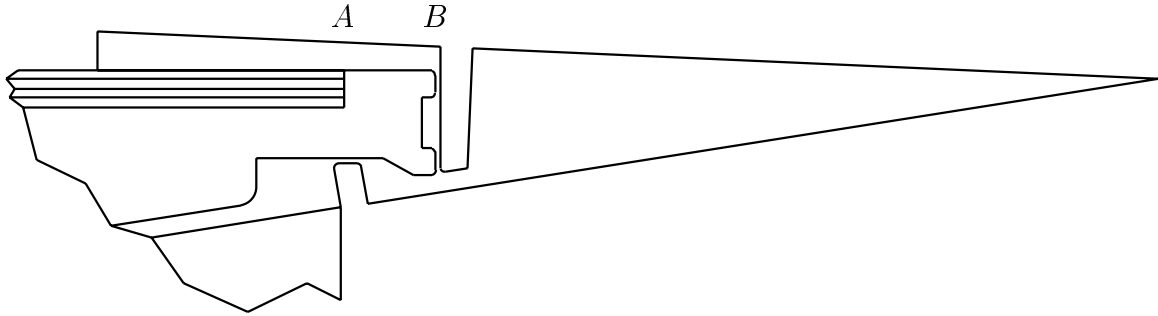The flexure mechanism was modeled as rigid, apart from the designed compliance

Figure 4-5: Location of extra compliance in the flexure mechanism.

of the flexures. However, during testing, extra bending in the flexure mechanism was observed between the tip of the bender and the vertical portion of the flexure mechanism, identified as member AB in Figure 4-5. During testing the gap between points A and B measured approximately 0.1 in. The design allowed for this gap to insure that no glue seeped onto the bottom flexure when attaching the flexure mechanism to the bender. However, due to the extra compliance that this gap introduces, future designs should minimize this distance.

In addition to the compliance identified between point A and B in Figure 4-5, another source of unmodeled flexibility in the system comes from the bond between the bender and the flexure mechanism. A cyanoacrylate adhesive was used to attach the flexure mechanism to the bender. The flexure mechanism, however, was intentionally separated from and re-attached to the bender a number of times throughout the course of the experiments, creating a rough bonding surface. Because of this, it was suspected that the bond may not have been intact over the entire bonding surface.

The combined effect on the system from these areas of extra compliance may be modeled as a spring, k_f, in series with the tip stiffness of the bender, k_B, and the modeled stiffness of the flexures, k_M, as shown in Figure 4-6, where M_F represents the equivalent mass contributed by the inertia of the flap. Although no good method exists to estimate the stiffness of this spring, k_f, because it is extremely dependent
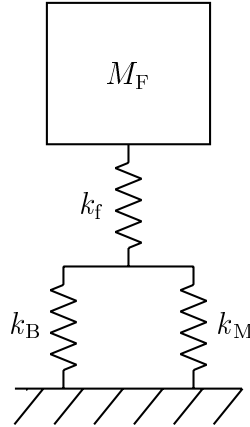
Figure 4-6: Configuration used to model extra compliance.

on the bond strength of the flexure mechanism to the bender, a preliminary estimate can be made by basing the stiffness magnitude on the bending stiffness of member AB in Figure 4-5. Using such a model, the spring stiffness is

$$k_{\mathrm{f}} = C_{\mathrm{f}} \frac{E_{\mathrm{d}} I_{\mathrm{f}}}{l_{\mathrm{f}}^3} \qquad (4.1)$$

where l_{f} and I_{f} are the length and moment of inertia of member AB and the coefficient, C_{f}, is chosen so as to quantify the strength of the bond layer boundary condition. In Section 4.2.2, the value chosen for C_{f} in order to relate experimental and analytical results is discussed.

In Section 4.1, it was mentioned that the electrodes were modeled as pure nickel, rigidly bonded to each piezoelectric wafer. Further checking into the makeup of these electrodes revealed that while they are a nickel alloy, they are actually silkscreened onto the piezoelectric wafers and not rigidly bonded. Because of this, the stiffness contributed by the electrodes to the bending inertia of the piezoelectric multi-morph is negligible. Their only contribution to the stiffness is in increasing the moment of inertia of the individual piezoelectric wafers by moving them farther from the neutral axis. Using this new model of the electrodes' stiffness contribution, the computed tip stiffness of the piezoelectric bender was almost halved from a design value of
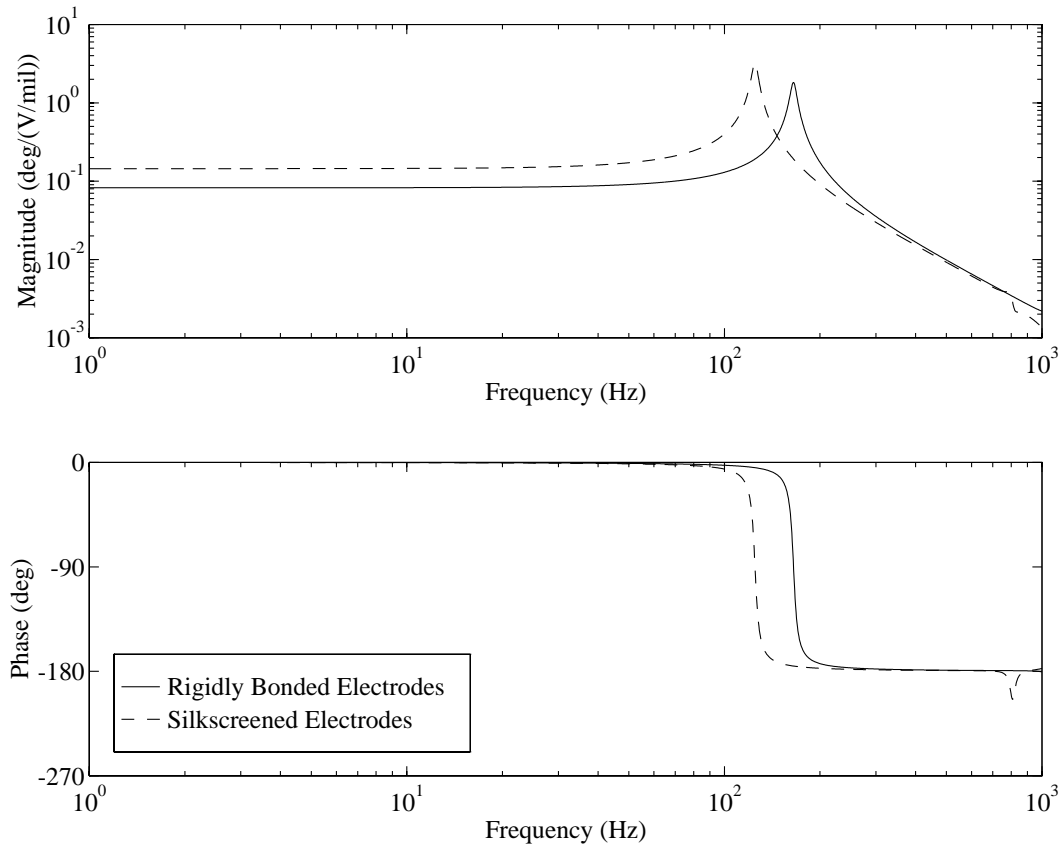
Figure 4-7: Change in flap deflection magnitudes as electrode stiffness changes.

200 lb/in/in to 113 lb/in/in. Since the lever arm length was already set before this error was detected, the actuator is no longer impedance matched for the design point span location of 90%, as discussed in Section 3.1.3.

While the tip stiffness is smaller than original predictions, because the same amount of piezoelectric ceramic, and thus energy, is still present in the bender, the expected flap deflections must increase. This is shown in Figure 4-7, where results from the analytical model are presented, comparing the predicted frequency response of the actuator for the two cases when the nickel electrodes are modeled as rigidly bonded and silkscreened onto the piezoelectric wafers. As expected, the flap deflections do increase. Furthermore, because the bender with silkscreened electrodes is more compliant, the first modal frequency drops from 165 Hz to 125 Hz, between the rigidly bonded and silkscreened cases.
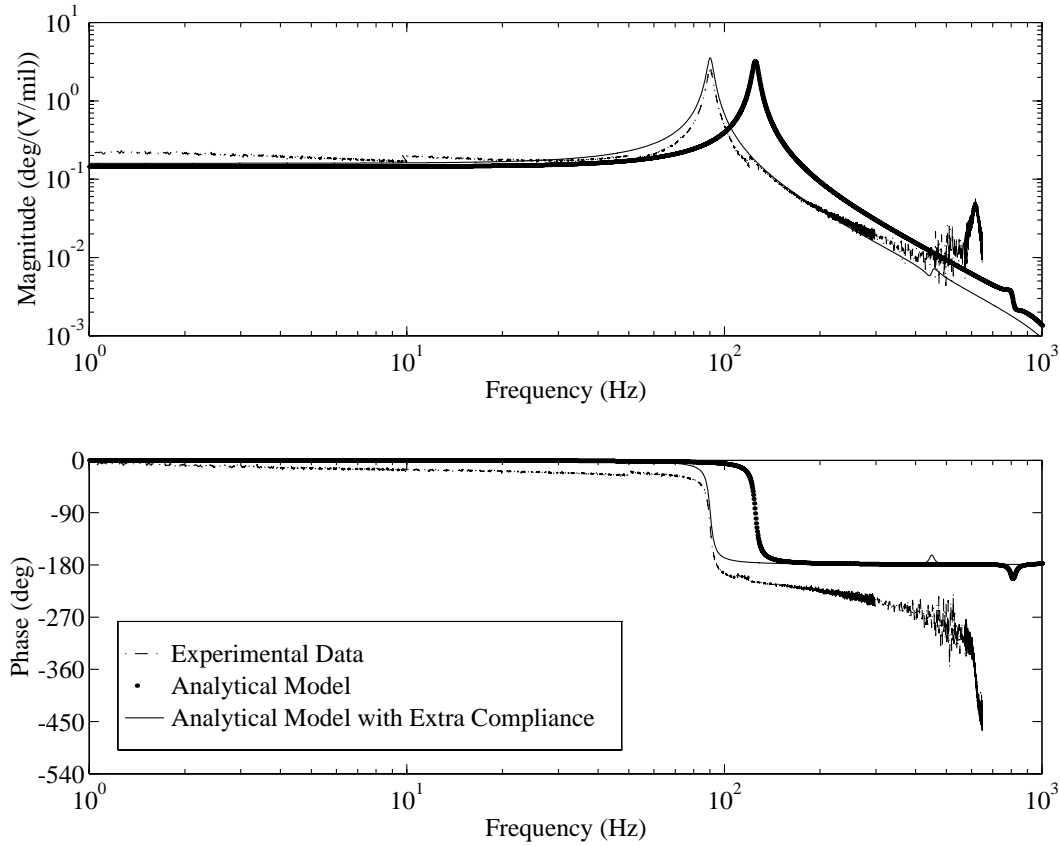
Figure 4-8: Experimental frequency response for first two modes of actuator.

In all future comparisons made with the analytical model, besides adding space in between piezoelectric wafer layers, the nickel electrodes are modeled as adding no stiffness to the bending inertia of the multi-morph.

4.2.2 Frequency Response Data

Actuator Response

Frequency response data was collected for the actuator in the configuration shown in Figure 4-1. Figure 4-8 shows the frequency response data for the entire band of frequencies identified in this experiment. Figure 4-9 is a close up of the low frequency behavior from 1 to 200 Hz. Figure 4-9 is included to highlight some of the nonlinear behavior of the actuator, discussed below. The frequency response data is presented in the standard Bode plot format. The transfer function represented by the magnitude
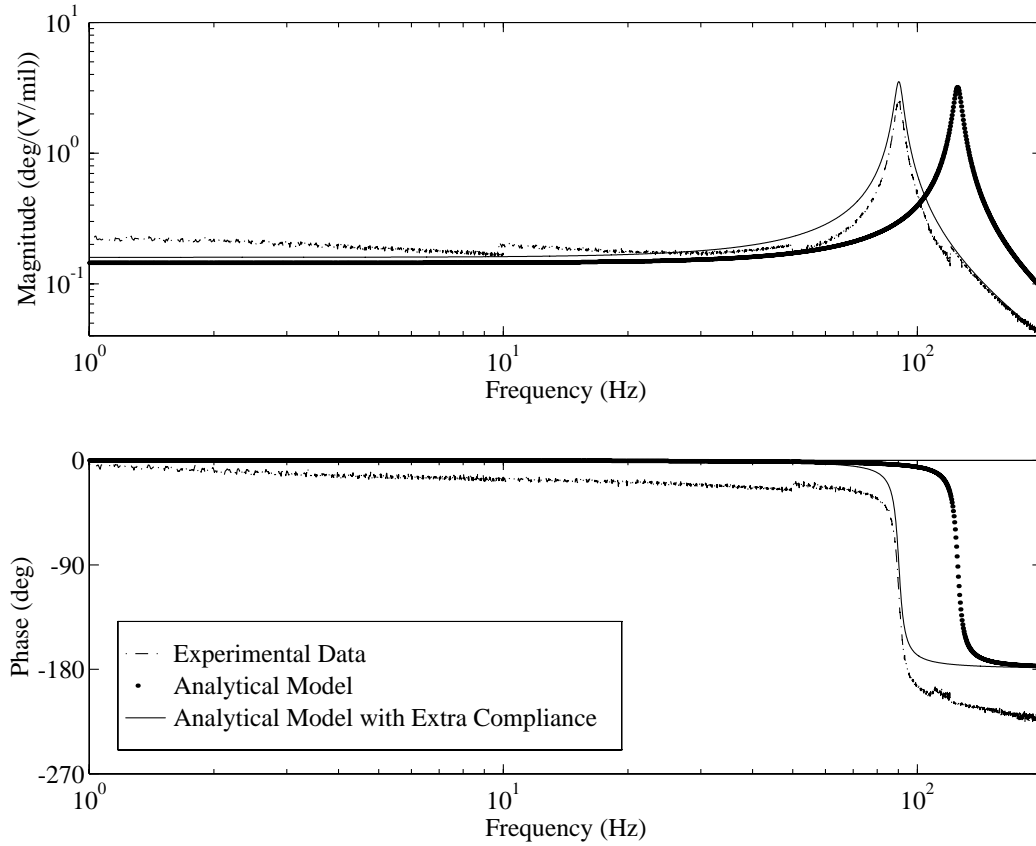
Figure 4-9: Experimental frequency response for first mode of actuator.

plot is the resultant flap deflection, in degrees, for an electric field applied over the bender. The applied electric field used is the sum of the electric field over the top and bottom halves of the bender. For example, the magnitude of the response given by the data at 1 Hz is 0.207 deg/(V/mil). Therefore, if the applied electric fields over the top and bottom half of the bender are 40 V/mil and 20 V/mil, the resultant flap deflection is

$$\delta = 12.42 \text{ deg}$$

The coherence for the data of Figures 4-8 and 4-9 is presented in Figure 4-10. The coherence is a measure of how accurately the acquired data characterizes the system. Excessive noise or disturbances to the system, as well as nonlinearities present in the system, can lead to poor coherence. The coherence can take on a value between zero and unity, where a value of unity means that the data taken exactly characterizes the
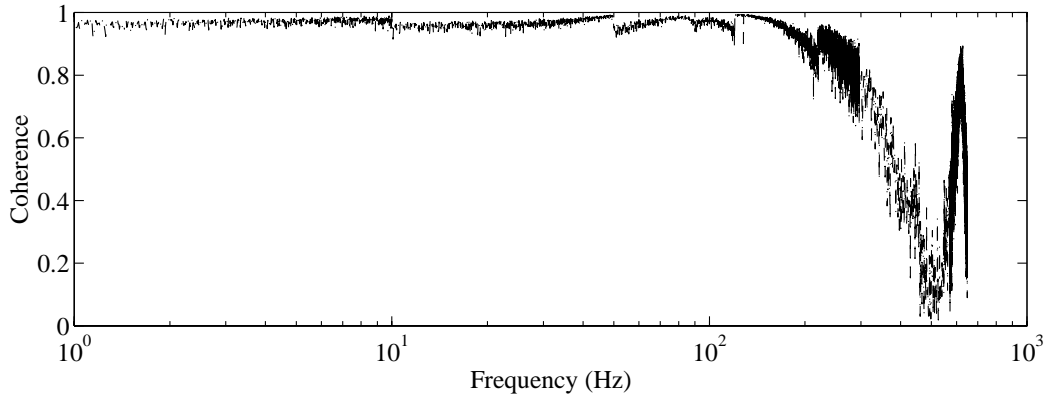
Figure 4-10: Coherence of the experimental frequency response data.

frequency response of the system. As shown in the figure, the coherence of the data for low frequencies is good. However, the coherence for data at frequencies greater than approximately 200 Hz is poor.

The reason for the poor coherence stems from current constraint of the high voltage amplifiers, which have a built in maximum current limit of 40 mA. Piezoelectric ceramics require more current as the actuation frequency increases, according to

$$i = VC\omega \tag{4.2}$$

where ω is the actuation frequency in radians/sec, V is the applied voltage, and C is the capacitance of one side of the bender, which, for this case, is 300 nF. If the maximum input signal is applied to the bender, the voltage signal becomes as large as 300 V during each cycle of operation. For such an input, Equation (4.2) indicates that the amplifiers will current limit at actuation frequencies greater than 70 Hz. During identification, however, it is not necessary to drive the system with the maximum voltages. In particular, due to the large response around the first mode, the data from 50 to 120 Hz was attained while driving the system with a relatively small input signal. However, even with the lower input magnitudes, once the actuation frequency reaches a certain level, the amplifiers do current limit, thus requiring the applied voltage to be reduced further. For frequencies greater than about 200 Hz, the

applied voltages had to be reduced to such a degree that the noise present constituted a significant portion of the measured signal, leading to a poor level of coherence. It is the additional response magnification of the second mode, however, that allowed its location and phase to be identified. Use of high voltage amplifiers which allow larger current levels are needed to accurately identify these high frequency dynamics. Unfortunately, none were available for these tests.

From Figures 4-8 and 4-9, the easiest characteristics of the system to identify are the frequency of the first and second modes, which are 90.1 Hz and 617 Hz, respectively. The target rotor for this study has a rotational speed of 780 RPM. Therefore, a natural frequency of 90.1 Hz corresponds to the 7/rev normalized frequency of that rotor. As discussed in Section 3.1.3, for a properly scaled rotor, if a modal frequency corresponds to the N/rev frequency of a model rotor, that modal frequency in the full-scale prototype will also occur at the N/rev frequency of the prototype. Therefore, a full-scale version of the present actuator will also have a resonant peak at the full-scale rotor's 7/rev frequency.

Also, as discussed in Section 3.3.2, the modal frequency found in this experiment is lower than it would be had the flap been properly inertially scaled. As it is, the flap has too much mass and, therefore, unnecessarily lowers the first modal frequency. For example, if the mass of the servo-flap drops by 50%, while retaining the same radius of gyration about the flap hinge, the analytical model predicts a 37% larger first modal frequency. This implies that if such a flap were used for the present experiment, a first modal frequency would occur close to the 10/rev frequency of the target model rotor. Of course, this projection depends, to a small degree, on the accuracy of the analytical model, but this example is included to emphasize that the modal frequencies present in this data underestimate what they could be if the inertial properties of the flap were set properly.

There are many additional issues regarding the behavior of the bender and flexure mechanism actuator highlighted by this data and the associated analytical model. The discussion of each are treated in the following subsections.

Analytical Predictions

Two additional frequency response traces are shown in Figures 4-8 and 4-9. These were both calculated using the analytical model derived in Chapter 2, and the dimensions of the layered piezoelectric multi-morph described in Section 4.1. The electrodes silkscreened onto each piezoelectric wafer were assumed to add no additional stiffness, as discussed above in Section 4.2.1.

In Section 2.2.2, the method used to add damping to the analytical model was described. The value of the viscous damping factor, ζ, is easily estimated from the magnitude of the experimental frequency response plots in Figures 4-8 and 4-9. If the maximum response at the frequency of the first structural resonance is denoted as Q, the half power points of this mode are those frequencies, f_1 and f_2, where the magnitude of the response drops to $\frac{Q}{\sqrt{2}}$. Once these points are identified, the viscous damping factor may be approximated as [36]

$$\zeta = \frac{f_2 - f_1}{2f_n} \tag{4.3}$$

where f_n is the frequency of the first mode. The half power frequencies estimated from the data in Figure 4-9 are approximately 88.2 and 92.3 Hz. Therefore, using Equation (4.3), the estimated damping factor, $\zeta = 0.0225$. This is the amount of damping included in the calculations yielding the two analytical frequency response plots in Figures 4-8 and 4-9.

As a note, even when testing at zero airspeed, Spangler and Hall observed levels of damping on the order of $\zeta = 0.2$ in their actuator [44]. This is almost a factor of 10 greater than that observed here. Their explanation for this damping was that it probably resulted from unmodeled friction effects present in the hinges. The large difference between the values of damping observed here as compared to Spangler and Hall's measurements, indicates that this assumption was probably correct, and it highlights the fact that the flexure mechanism has completely eliminated the friction problems encountered by Spangler and Hall [45], [44].

As shown in the frequency response plots, the pure analytical model predicts a

first structural resonance at 125 Hz, which is 39% greater than the actual value. A possible explanation for this large difference is the extra compliance in the flexure mechanism and in its bond to the bender, as discussed in Section 4.2.1. In that section, a method suggested to account for this extra motion was to model it as a spring, k_f, in series with springs representing the tip stiffness of the bender and the designed stiffness of the three flexures in the flexure mechanism. An expression for the stiffness of this extra spring was given in Equation (4.1). It is well known, from elementary beam theory, that if member AB is rigidly clamped to the tip of the bender, then $C_f = 3$. However, if this model is to account for the difference in the first modal frequency, then it is necessary for $C_f = 0.135$. The second analytical curve shown in Figures 4-8 and 4-9 uses this value of C_f to incorporate this compliance mechanism into the analytical model. As shown, this modified transfer function does yield a first modal frequency matching that of the data.

A value of $C_f = 0.135$ implies that the extra motion due to the imperfect bond between the bender and flexure mechanism makes member AB's boundary condition at the bender softer than a rigid clamp by a factor of approximately 22. While it is conceivable that the integrity of the bond is poor enough to account for this difference in modal frequencies, without measurements of the bond strength, it is not possible to be absolutely certain. Nevertheless, it is clear that the bond strength at the bender can have a major effect on the response of the actuator.

Presence of Piezoelectric Ceramic Nonlinearities

In interpreting the data presented in Figures 4-8 and 4-9, the first fact to realize is that the method used in identifying a system by Fourier analysis rests, fundamentally, on the assumption of linearity in the material. For a purely linear system, it is warranted to expect the frequency response to be very similar to that found with the linear analytical methods. However, nonlinearities in the system will lead to differences in the measured and predicted responses. For a strongly nonlinear system, the measured response can appear completely unrelated to the linear analytical predictions. The fact that the data in Figures 4-8 and 4-9 has a strong resemblance to the analytically

predicted curves indicates that the nonlinearities present in the piezoelectric ceramic do not overwhelm its response. However, because the nonlinearities do exist, the data in these figures must be interpreted with some care. The following section will present an explanation of how the different nonlinear mechanisms associated with piezoelectric ceramics may explain the observed behavior.

Using a linear analysis tool to identify the response of a system with nonlinearities will not capture certain details of the system's behavior. Furthermore, identifying the same system while driving it with slightly different input signals can result in slight variations in the measured response. For example, in the identification of the data in Figures 4-8 and 4-9, to maximize the coherence, separate frequency response identification tests were run to obtain the data for the frequency ranges of $0 - 10$ Hz, $10 - 50$ Hz, $50 - 120$ Hz, $120 - 220$ Hz and in 40 Hz increments from $220 - 580$ Hz with the final two sets of data covering the frequency ranges from $580 - 610$ Hz and $610 - 650$ Hz. There is no guarantee that the input conditions during each of these tests was identical. Besides the obvious fact that the input signal for each of these tests was centered around a different frequency, other nonlinear effects such as the strain to temperature and strain to electric field behavior of piezoelectric ceramics, discussed in Section 4.2.1, could also lead to slight changes in the conditions of the system and how it reacts to the input during each of these tests. Because of this, there is no guarantee that the measured response at the boundaries between these tests will exactly line up. This is why the apparent discontinuities appear in the magnitude response, as highlighted in Figure 4-9 at 10, 50 and 120 Hz.

At frequencies less than approximately 20 Hz, the magnitude of the data is larger than analytical predictions. It is postulated that higher strain levels than predicted from the linear model account for this difference in magnitudes. As discussed in Section 4.2.1, higher than predicted strain levels may be attributed to temperature, creep and nonlinear strain to electric field effects. The effects of temperature are not substantial enough to explain the magnitude behavior observed. Furthermore, while the creep mechanism of the piezoelectric ceramic is a possible explanation of higher than normal deflection amplitudes, because it is an effect predominantly important

at frequencies less than 1 Hz, it is believed that its contribution is also minimal. Therefore, it is suspected that the nonlinear strain to electric field effect is the predominant cause of the magnitude differences between the data and the analytical model frequency response plots in Figures 4-8 and 4-9.

In Section 4.2.1, the mechanism behind the nonlinear strain to electric field relationship of the piezoelectric ceramic was identified as additional poling motion occurring due to high applied electric fields. As mentioned there, this effect decreases with frequency. This is clearly shown in Figures 4-8 and 4-9 by the reduction in the magnitude response from 1 Hz up to approximately 30 Hz, where the first mode begins to contribute. Another fact discussed in Section 4.2.1 was that for high frequencies, this nonlinear strain mechanism diminishes to the point where the linear strain to field relationship specified in most piezoelectric catalogs is recovered. The indication of such behavior in the measured data is evident from the fact that the magnitude of the measured response approaches that of the linear model for frequencies greater than 20 Hz.

Another nonlinear mechanism easily identified in the frequency response data is hysteresis. A definite manifestation of the hysteresis in the bender is its larger than predicted phase lag. As discussed in Section 2.2.2, the amount of hysteresis increases with amplitude. This is reflected in the phase plots of the data by the large reduction in phase for frequencies near the first and second modes. Extra phase lag due to hysteresis will present some limits on the performance when actual feedback control is implemented with the actuators. It may be possible to implement a simple feedback of the piezoelectric ceramic charge to eliminate the effects of hysteresis [44] when closed loop control is implemented with these actuators.

While piezoelectric ceramics do exhibit a number of nonlinearities, they are mild enough not to exclude the possibility of using these materials for the desired purpose of helicopter control. Even so, the presence of the nonlinearities does add some complications to the response and should be seriously considered in the use of such actuators.
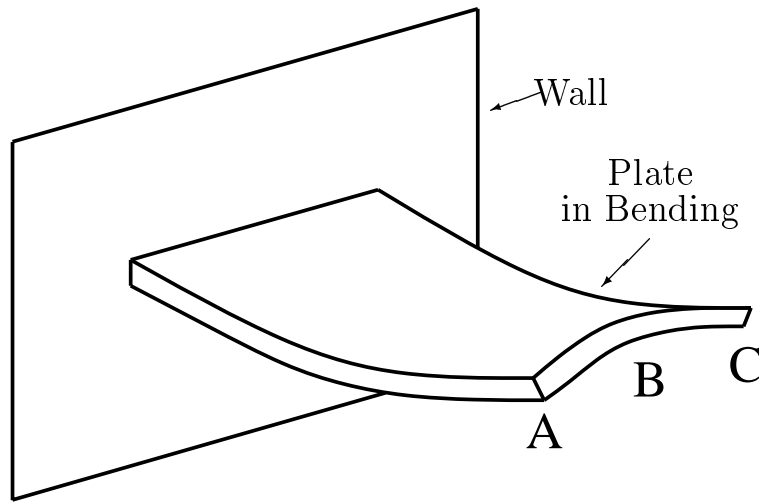
Figure 4-11: Conceptual picture of anticlastic bending.

Zero Location

The analytical model predicts a near pole-zero cancellation of the second mode. The presence of the second mode in the data, however, demonstrates that this cancellation does not actually occur. Furthermore, analyzing the phase at the second mode also indicates that the zero does not occur at a lower frequency than this mode but actually at a frequency much higher than the second modal frequency. The process of predicting the location of the zeros is subject to the greatest amount of modeling errors. For this reason, due to the simplicity of the analytical model, it is not completely realistic to expect an accurate answer about zero locations. However, using the analytical model and some physical insight, a possible explanation of the behavior of the first zero may be explained by considering the spanwise or anticlastic bending at the tip of the multi-morph.

The second mode of the analytical model represents anticlastic bending. A conceptual view of the anticlastic effect on a plate as it bends is presented in Figure 4-11. As shown, when the plate bends up, the compression in the top half and tension in the bottom half of the plate cause its outer corners, points A and C, to travel through smaller deflection than its center, point B. In the analytical model, the tip displace-
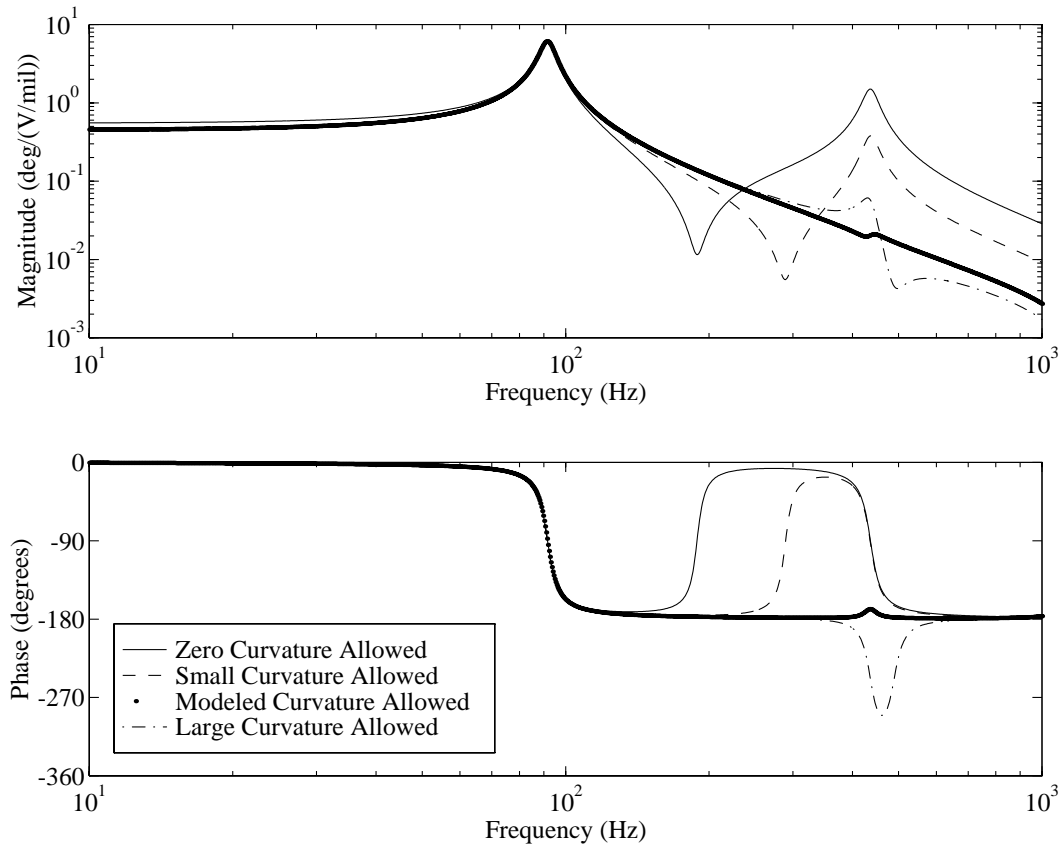
Figure 4-12: Effect of anticlastic bending on poles and zeros.

ment was calculated by averaging the deflections over the width of the bender. If the anticlastic effect is large enough in comparison to the lengthwise bending of the plate, the calculated tip displacement will be zero. By the same argument, if even more anticlastic bending occurs, the calculated tip displacement could have a net value reflecting a downward motion when the plate bends up. This type of behavior would be reflected in the frequency response of the system by a phase shift of 180 deg caused by the zero moving to a frequency greater than the second modal frequency. This is, in fact, how the analytical model behaves. By modifying, at the output, the amount of anticlastic bending accounted for in the calculation of the tip displacement from zero curvature up to a curvature greater than the actual value used to calculate the analytical curves of Figures 4-8 and 4-9, the change in the location of the zero may be shown by a sequence of frequency response plots, as in Figure 4-12. In this figure,

the meaning of "small" and "large" are, of course, relative. The actual change in the amount of anticlastic bending between each case is not too substantial. Each level of curvature was chosen to demonstrate how the analytics follow the above explanation. As shown, the change in the zero location with different amounts of curvature does indeed follow this explanation.

The location of the zero is important because in feedback control, it is often useful to know the location of high frequency dynamics in order to determine if they contribute to the magnitude or phase of the system under control. It is not clear whether extra anticlastic bending is the sole reason why the first zero of the actual system is located at a frequency much greater than the second mode. The coherence problems discussed above preclude the ability to clearly identify the high frequency dynamics. However, the above discussion does present a plausible explanation, implying that future models of the bender's behavior should treat the expected anticlastic bending with some depth for a realistic prediction of the location of and the effect that changes in system parameters have on the first zero.

4.2.3   Achievable Hinge Moments

Figure 4-13 shows the measured flap deflections for sinusoidally applied electric fields applied to the bender at 0.1, 1, 5 and 10 Hz. As with the frequency response data of the previous section, the electric fields representing the abscissas of this plot are the sum of the electric fields into both sides of the bender.

Two different low frequency effects contribute to create larger maximum deflections at 0.1 and 1 Hz as compared to the 5 and 10 Hz data traces. The first effect is the nonlinear strain to electric field relationship discussed in Section 4.2.1 and 4.2.2. It is believed that it is the main cause of the larger deflections seen in the 1 Hz data. As discussed above, this strain mechanism is frequency dependent, contributing less for higher frequency actuation as shown by comparing the 1 Hz trace to the 5 and 10 Hz data traces. The second effect is one due to the creep mechanism in the piezoelectric ceramics. Because creep is a phenomenon limited to frequencies less than 1 Hz, its contribution to the magnitudes of response for the 1 Hz data trace are assumed
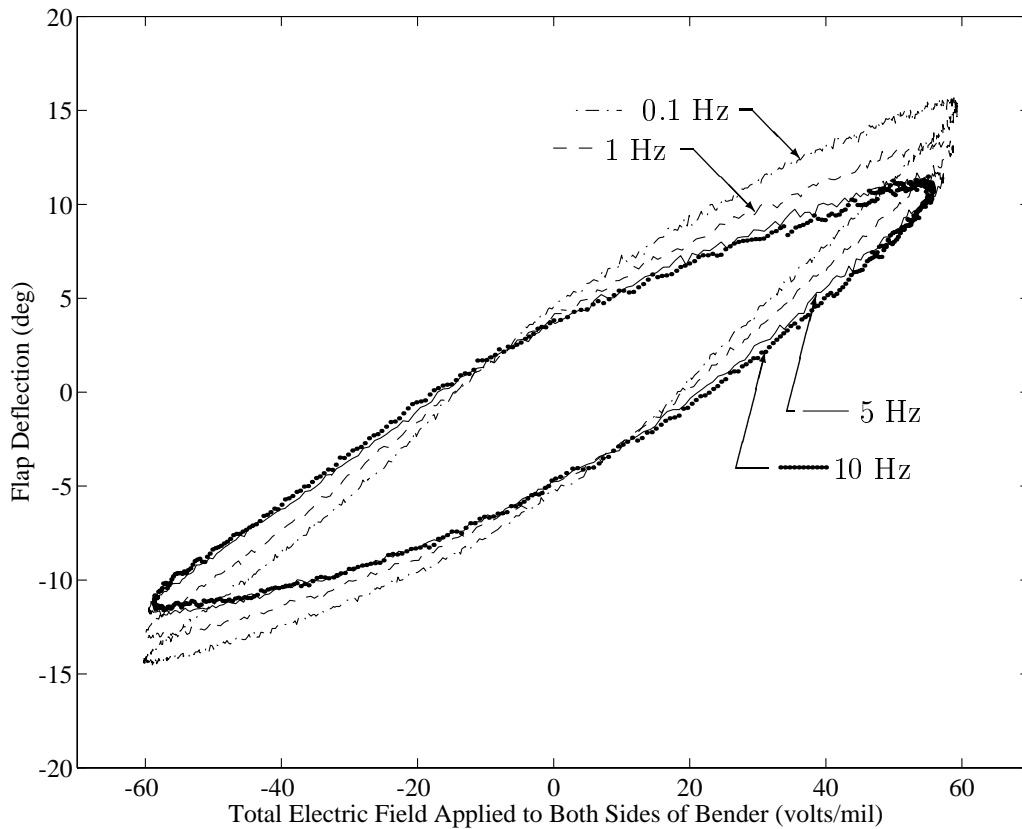
Figure 4-13: Low frequency voltage to deflection behavior.

to be minimal. However, it is suspected to be the main cause in the difference in magnitude between the 0.1 and 1 Hz data traces.

In addition to creep, another interesting phenomenon highlighted by this figure is the hysteresis of the piezoelectric bender with frequencies. As shown in Figure 4-13, the amount of hysteresis is relatively constant for frequencies up through 10 Hz. However, the amount of hysteresis changes with higher frequencies, as shown in Figure 4-14, which is the same type of plot as Figure 4-13, but at higher frequencies and slightly lower input field levels. This figure shows that the amount of hysteresis begins to increase at approximately 20 Hz, with the trace corresponding to actuation at 40 Hz showing a great deal of hysteresis. This behavior is expected when one considers that the amount of hysteresis is proportional to the square of the amplitude of the response [36]. Therefore, as the first mode is approached, the hysteresis should increase as shown.
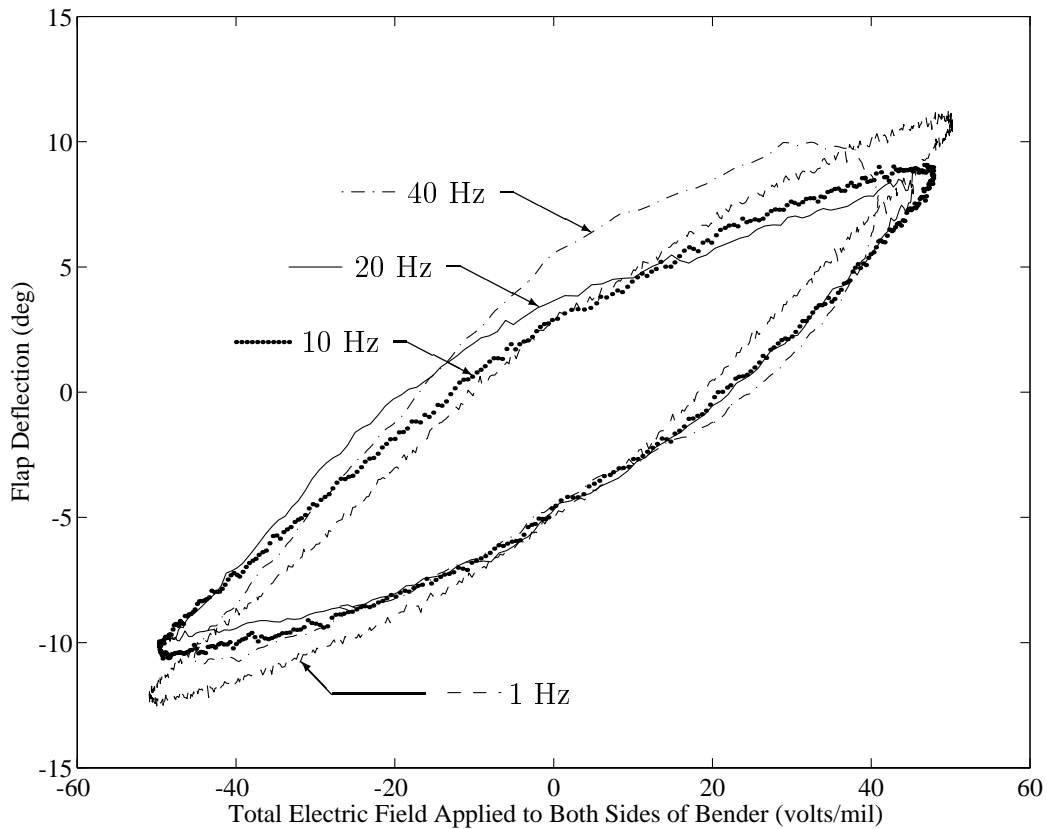
Figure 4-14: High frequency voltage to deflection behavior.

The original strategy for measuring hinge moment capability was to hang weights off the end of the flap and measure the resultant deflection. Unfortunately, however, creep in the piezoelectric ceramic proved to be a limiting factor in performing these measurements because to avoid its effects, the measurements had to be performed at frequencies greater than 1 Hz. Performing such measurements at this frequency level is not feasible considering the inertial forces that would exist due to the tip weights. Because of this fact, only an estimate of the achievable hinge moments is presented here.

If the tip stiffness of the bender is known, the expected hinge moments can be extrapolated in a relatively straight-forward fashion using the deflection characteristic of the system under zero load. The main problem in doing this is that an accurate measurement of the tip stiffness of the bender also could not be obtained due to the creep effects. For this reason, the analytical model is used to estimate the tip stiffness.

As discussed in Section 4.2.1, assuming the electrodes add only space between the piezoelectric wafers and no additional bending inertia, the tip stiffness is calculated as 113 lb/in/in.

As a note, Spangler and Hall also had difficulties in measuring the tip stiffness of their piezoelectric bender, noting that there did not seem to be a constant value of the tip stiffness of these piezoelectric ceramics, and that a practical method to measure this property did not exist [44].

As shown in Figure 4-13, the maximum flap deflection of the actuator at 10 Hz is 11.5 deg. Recalling that only six out of the eight layers of the bender were in service for these experiments, the measured flap deflections were estimated to be 8% less than that possible, as discussed in Section 4.1. Accounting for this factor gives the expected maximum flap deflection at 10 Hz as 12.5 deg, which, using the analytically calculated tip stiffness of 113 lb/in/in, translates into an expected flap deflection of 4.5 deg for 10 Hz operation at the 90% span location on the target model rotor in Freon. As mentioned in Section 3.2, the poling and coercive field limits for this study were conservatively set at 40 V/mil and 20 V/mil, respectively. However, by pushing the applied voltages to their maximum levels, corresponding to electric field limits of 60 V/mil and 30 V/mil, deflections of 6.8 deg for 10 Hz operation at the 90% span location on the target model rotor in Freon can be expected.

The question remains as to how this actuator would perform if scaled for implementation on a real helicopter in air. As noted in Section 3.1.3, the target model rotor has dynamic pressures 35% smaller than those that exist on an operational helicopter in air. However, assuming that all dimensions are scaled geometrically, the difference in flap deflections can be related by using the ratios of the dynamic pressures for each case. Therefore, using Equation (3.13), if actuating with the non-conservative poling and coercive field limits of 60 V/mil and 30 V/mil, the above results indicate that a 5.0 deg deflection can be expected if the present actuator was scaled up and placed at the 90% span location on a typical operational helicopter in air. Furthermore, if the actuator was impedance matched to the aerodynamics present at the 90% span location of such a helicopter, the expected deflections could be as large as 5.6 deg.

A major source of error in the above calculations occurs because the tip stiffness used was analytically determined. True validation of these numbers will only be obtained by determining a valid experimental value for the tip stiffness of the bender.

4.3 Summary

These experiments demonstrated the effectiveness of the actuator in producing appreciable flap deflections. The friction and backlash problems originally identified by Spangler and Hall [45], have been overcome. However, additional complications from the nonlinearities of the piezoelectric ceramics have also been identified. Furthermore, the effects of creep proved to be insurmountable in obtaining a good experimental estimate of the achievable hinge moments of this actuator.

Flap deflections of 11.5 deg were demonstrated on the bench top while operating at a frequency of 10 Hz. Using an analytical prediction of the bender's tip stiffness, this data suggests that properly scaling and impedance matching the actuator can result in flap deflections greater than 5 deg while operating at the 90% span location on an operational helicopter in air.

In addition, the data also indicates that, if proper inertial scaling of the flap is performed, the actuator could have a first modal frequency as high as 10/rev on both the target model rotor, and, if properly scaled, on a full scale helicopter rotor.

Chapter 5

Conclusions

In this thesis, a piezoelectric actuator intended for the control of a helicopter rotor was designed, built, and tested on the bench top. The design used was based on a previous study performed on this actuation mechanism by Spangler and Hall [45]. Its lengths were chosen so that it fit within the cross-section of a model scale rotor operating in Freon with a 4.454 in chord and a 20% flap. In this study, a number of improvements over the original design were introduced. This chapter, the contributions of this research are described and suggestions for future research are given.

5.1   Design Contributions and Improvements

Three major improvements to the actuator originally built by Spangler and Hall were introduced in this thesis. The most significant of these was the use of the flexure mechanism to transmit the bender deflections to the flap. The effectiveness of the actuator used by Spangler and Hall [45] was significantly reduced due to friction and backlash generated from the use of hinges in coupling the bender and flap deflections. The greatest benefit found in the operation of the flexure mechanism is the complete elimination of these friction and backlash problems.

The other major improvements introduced were the tapering of the bender's thickness properties, increasing its efficiency by over 20%, and the implementation of a

nonlinear electric circuit to increase the average electric field applied to the bender by 50%.

A state space model of this actuator based on Classical Laminated Plate Theory was developed using the Rayleigh Ritz energy method. This model provided a metric against which the experimental results were measured and highlighted the effects of nonlinearities inherent in the operation of piezoelectric ceramics, such as creep, hysteresis, nonlinear strain to field and nonlinear strain to temperature behavior. A preliminary treatment of these effects was presented, but they deserve a more thorough investigation.

On the bench top, flap deflection amplitudes of 11.5 deg were demonstrated for actuation at 10 Hz. Because only six of the eight piezoelectric wafers in the bender were in operation for the tests, it was calculated that this deflection was 8% below the actuator's actual flap deflection capability.

There was a substantial amount of creep present in the operation of the bender at frequencies below 1 Hz. For this reason, it was not possible to obtain measurements of the achievable hinge moments of this actuator on the bench top. However, using an analytically determined bender tip stiffness and the experimentally measured flap deflections, the operational characteristics of this actuator were extrapolated

The actuator was designed for operation at the 90% span location on a model rotor in Freon. Based on the experimental results and analysis, it is concluded that a flap deflection of 6.8 deg should be possible at frequencies below the natural frequency for an actuator located at the 90% span location of this target model rotor. Using the scaling laws developed in Section 3.1.3, the data also suggests that if this actuator were properly scaled up to an operational helicopter, flap deflections of 5.0 deg at the same electric field and relative frequency levels can be expected at the 90% span location of an operational full-scale helicopter blade.

The experimental data showed a first modal frequency of 90.1 Hz, which corresponds to the 7/rev frequency of the model rotor. From the scaling laws, this implies that a scaled version of this actuator will also have a first modal frequency corresponding to the 7/rev frequency of a full-scale rotor. Because the inertial properties

of the flap were not addressed, however, larger modal frequencies (and therefore larger actuator bandwidths) should be expected when this actuator is used with a lighter servo-flap.

In summary, a trailing edge servo-flap actuator has been refined to correct the friction and backlash problems identified originally by Spangler and Hall [45]. Substantial deflections have been demonstrated on the bench top for an actuator designed to fit within a scaled model helicopter blade allowing for a 20% flap. The results of this study indicate that this actuator should be able to actuate the rotor of an operational helicopter.

5.2   Future Research Goals

There are three major suggestions for future research;

1. Demonstration of piezoelectrically actuated trailing edge servo-flap in a wind tunnel typical section. To truly gauge the abilities of the present design, a wind tunnel test of a typical section incorporating the improved actuator presented in this thesis should be performed.

2. Detailed design of a model rotor system with integrated trailing edge servo-flaps. There are many issues to be addressed in order to integrate the piezoelectric actuators described in this thesis into an operational model rotor. One major design consideration is the large centripetal accelerations that these actuators will encounter in the rotor blade environment. Enough strength must be ensured to withstand accelerations that are on the order of hundreds of g's. In addition, proper mass balancing of the blades must also be addressed to overcome the stability issues associated with placing heavy actuators in the trailing edge of an airfoil.

3. Tests on a model scale rotor. Once a viable rotor with integrated piezoelectrically actuated trailing edge servo-flaps is designed and constructed, tests must be conducted to determine the ultimate usefulness of these actuators in controlling a helicopter rotor.

Appendix A

Assumed Mode Shapes

In Chapter 2, the assumed mode shapes in the lengthwise (x) direction correspond to the exact mode shapes of a cantilevered beam. These shapes are

$$\cosh\left(\lambda_i \frac{x}{L}\right) - \cos\left(\lambda_i \frac{x}{L}\right) - \sigma_i \left(\sinh\left(\lambda_i \frac{x}{L}\right) - \sin\left(\lambda_i \frac{x}{L}\right)\right)$$

where L is the beam length and the coefficients λ_i and σ_i are given in Table A.1.

Table A.1: Coefficients for first five exact cantilevered beam mode shapes

ModeNumber, i	λ_i	σ_i
1	1.87510407	0.734095514
2	4.69409113	1.018467319
3	7.85475744	0.999224497
4	10.99554073	1.000033553
5	14.13716839	0.999998550

Appendix B

Non-Linear Circuit

The following circuit diagram is that of the non-linear circuit used to drive the piezo-electric bender. The motivating discussion behind this circuit is in Section 3.2. In this diagram, V_{in} is the input signal from the signal wave generator while V_{bot} and V_{top} are the output signals to the high voltage amplifiers which power the bottom and top sides of the bender, respectively.
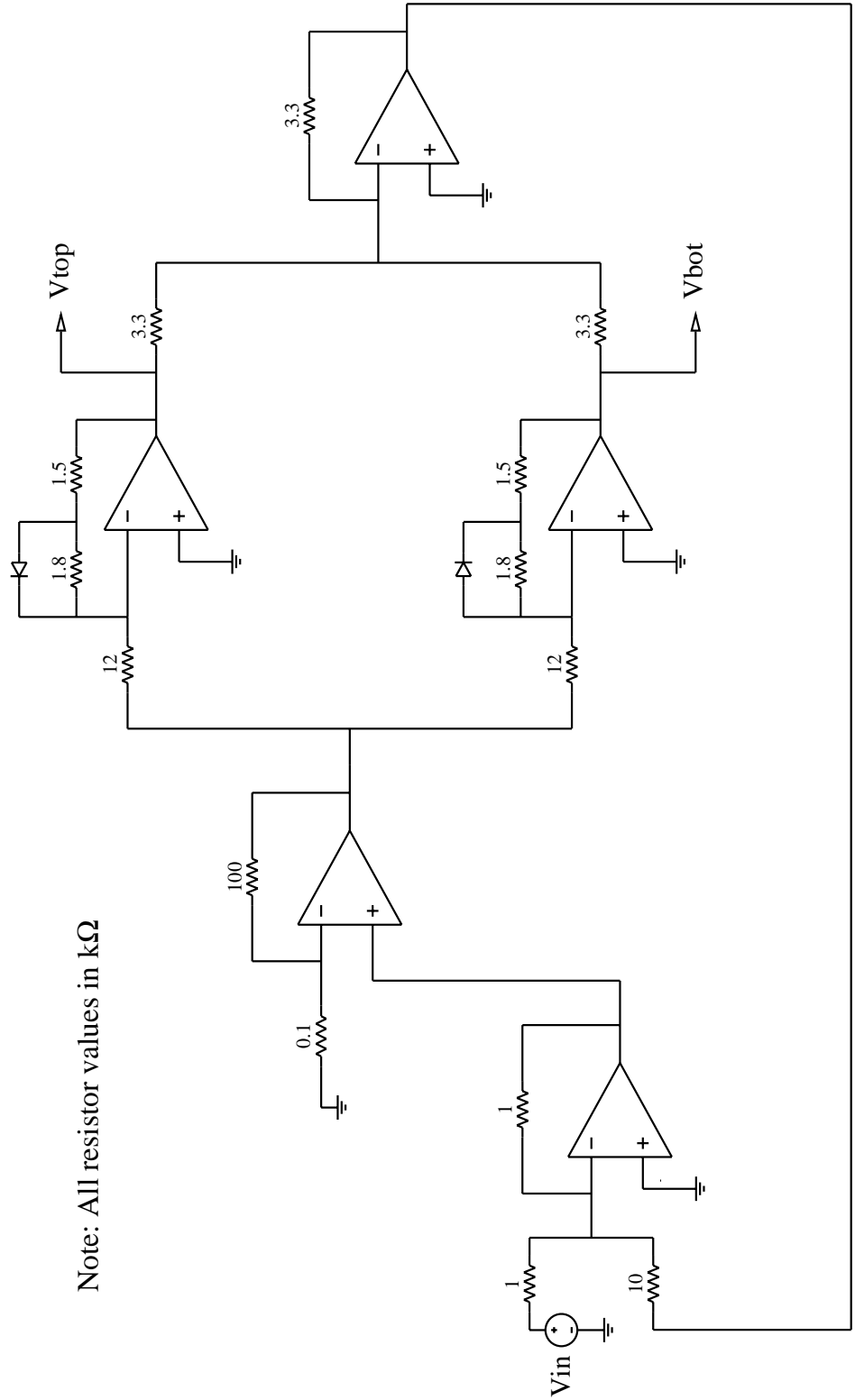
Note: All resistor values in kΩ

Vtop

Vbot

Vin

References

[1] Abbott., I. H. and von Doenhoff, A. E., *Theory of Wing Sections – Including a Summary of Airfoil Data*, Dover Publications, New York, 1959.

[2] Anderson, E. H., "Piezoceramic Actuation of One and Two-Dimensional Structures," Master's thesis, Massachusetts Insitute of Technology, Dept. of Aeronautics and Astronautics, Cambridge, MA, June 1989.

[3] Barrett, R., "Active Plate and Wing Research Using EDAP Elements," *Journal of Smart Materials and Structures*, Vol. 1, No. 3, September 1992, pp. 214–216.

[4] Berlincourt, D., *Ultrasonic Transducer Materials*, Chapter 2, pp. 63–109, Plenum Press, New York - London, 1971.

[5] Bisplinghoff, R. L., Ashley, H. and Halfman, R. L., *Aeroelasticity*, Addison-Wesley, Cambridge, MA, 1955.

[6] Bisplinghoff, R. L., Mar, J. W. and Pian, T. H. H., *Statics of Deformable Solids*, Dover Publications, Inc., New York, 1990.

[7] Blevins, R. D., *Formulas for Natural Frequency and Mode Shape*, Van Nostrand Reinhold, New York, 1979.

[8] Carpenter, P. J. and Paulnock, S., "Hovering and Low-Speed Performance and Control Characteristics of an Aerodynamic-Servocontrolled Helicopter Rotor System as Determined on the Langley Helicopter Tower," NACA TN-2086, May 1950.

[9] Chopra, I., "Dynamic Analysis of Constant-Lift and Free-Tip Rotors," *AIAA Dynamic Specialists Conference*, Atlanta, GA, April 1981.

[10] Crawley, E. F. and Anderson, E. H., "Detailed Models of Piezoceramic Actuation of Beams," *Journal of Intelligent Material Systems and Structures*, Vol. 1, No. 1, pp. 4–25, 1990.

[11] Crawley, E. F. and de Luis, J., "Use of Piezoelectric Actuators as Elements of Intelligent Structures," *Journal of AIAA*, Vol. 25, No. 10, pp. 1373–1385, 1987.

[12] Drela, M., "Xfoil: An Analysis and Design System for Low Reynolds Number Airfoils," *Low Reynolds Number Aerodynamics*, Springer-Verlag Lecture Notes in Engineering, No. 54, 1989.

[13] Dupont, *Design Handbook for Dupont Engineering Plastics - Module III: Delrin acetal resin*, Wilmington, DE.

[14] Ehlers, S. M. and Weishaar, T. A., "Static Aeroelastic Behavior of an Adaptive Laminated Piezoelectric Composite Wing," AIAA Paper 90-1078, April 1990.

[15] Ekquist, D. G., "Design and Wind Tunnel Test of a Model Helicopter Rotor Having an Independently Movable Inboard Blade Panel," U.S. Army Aviation Material Laboratories Technical Report 65-63, October 1965.

[16] Fabunmi, J. A., "Control of Helicopter Rotorblade Aerodynamics," NASA Contract Report CR-4350, July 1991.

[17] Fox, R. W. and McDonald, A. T., *Introduction to Fluid Mechanics*, Third Edition, John Wiley & Sons, New York, 1985.

[18] Garcia, J. C., "Active Helicopter Rotor Control Using Blade-Mounted Actuators," Master's thesis, Massachusetts Insitute of Technology, Dept. of Mechanical Engineering, Cambridge, MA, February 1994.

[19] Glauert, H., "Theoretical Relationships for an Aerofoil with Hinged Flap," Aeronautical Research Council Reports and Memoranda 1095, April 1927.

[20] Hall, S. R., Yang, K. Y., and Hall K. C., "Helicopter Rotor Lift Distributions for Minimum Induced Power Loss," *AHS International Technical Specialists' Meeting on Rotorcraft MultiDisciplinary Design Optimization*, Atlanta, GA, April 1993.

[21] Ham, N. D., "Helicopter Individual-Blade-Control Research at MIT 1977–1985," *Vertica*, Vol. 11, No. 1/2, pp 109-122, 1987.

[22] Hertzberg, R. W., *Deformation and Fracture Mechanics of Engineering Materials*, Third Edition, John Wiley & Sons, New York, 1989.

[23] IRE, "IRE Standards on Piezoelectric Crystals – Determination of the Elastic, Piezoelectric, and Dielectric Constants – The Electromechanical Coupling Factor, 1958," *Proceedings of the IRE*, Committee on Piezoelectric Crystals and Standards Committee, pp. 764 – 778, April 1958.

[24] IRE, "IRE Standards on Piezoelectric Crystals – Measurements of Piezoelectric Ceramics, 1961," *Proceedings of the IRE*, Committee on Piezoelectric Crystals and Standards Committee, pp. 1161 – 1169, July 1961.

[25] Jones, R. M., *Mechanics of Composite Materials*, Scripta Book Company, Washington D.C., 1975.

[26] Kretz, M., "Research in Multicyclic and Active Control of Rotary Wings," *Vertica*, Vol. 1, pp. 95–105, 1976.

[27] Kretz, M. and Larche, M., "Future of Helicopter Rotor Control," *Vertica*, Vol. 4, pp. 13–22, 1980.

[28] Landgrebe, A. J. and Davis, M. W., "Analysis of Potential Helicopter Vibration Reduction Concepts," *AHS Decennial Specialists' Meeting on Rotorcraft Dynamics*, November 1984.

[29] Lazarus, K. B., Crawley, E. F. and Lin, C. Y., "Fundamental Mechanisms of Aeroelastic Control with Control Surface and Strain Actuation," AIAA Paper 91-0985, April 1991.

121

[30] Lemnios, A. Z., Nettles, W. E. and Howes, H. E., "Full Scale Wind Tunnel Tests of a Controllable Twist Rotor," *32nd Annual Forum*, American Helicopter Society, 1976.

[31] Lemnios, A. Z., Smith, A. F. and Nettles, W. E., "The Controllable Twist Rotor, Performance and Blade Dynamics," *28th Annual Forum*, American Helicopter Society, 1972.

[32] Loewy, R. and Tseng, S., "Smart Structures Stabilized Unstable Control Surfaces," *Proceedings of the 34th Structures, Structural Dynamics and Materials Conference*, La Jolla, CA, April 1993.

[33] The Math Works, Natick, MA, *MATLAB Reference Guide*, June 1993.

[34] McCloud, J. L. III, "The Promise of Multicyclic Control," *Vertica*, Vol. 4, No. 1, 1980.

[35] McCloud, J. L. III and Weisbirch, A. L., "Wind-Tunnel Results of a Full-Scale Multicyclic Controllable Twist Rotor," *34th Annual Forum*, American Helicopter Society, 1978.

[36] Meirovitch, L., *Elements of Vibration Analysis*, Second Edition, McGraw-Hill Publishing Company, New York, NY, 1986.

[37] Millott, T. A. and Friedmann, P. P., "Vibration Reduction in Helicopter Rotors Using an Active Control Surface Located on the Blade," *Proceedings of the 33rd Structures, Structural Dynamics and Materials Conference*, Dallas, TX, April 1992.

[38] Morgan Matroc, *Piezoelectric Technology Data for Designers*, Electro Ceramics Division, Bedford OH.

[39] Nguyen, K. and Chopra, I., "Effect of Higher Harmonic Control on Rotor Performance and Control Loads," *Journal of Aircraft*, Vol. 29, No. 3, 1992.

[40] Pan, W. Y., Sun, S. and Tuttle, B. A., "Electromechanical and Dielectric Instability Induced by Electric Field Cycling in Ferroelectric Ceramic Actuators," *Journal of Smart Materials and Structures*, Vol. 1, pp. 286–293, 1992.

[41] Piezo Electric Products Inc., *Piezoelectric Motor/Actuator Kit Manual*, Advanced Technology Group, Cambridge, MA, 1988.

[42] Rossi, M. J., Austin, F. and van Nostrand, W., "Active Rib Experiment for Shape Control of an Adaptive Wing," *Proceedings of the 34th Structures, Structural Dynamics and Materials Conference*, La Jolla, CA, April 1993.

[43] Shaw, J., Albion, N., Hanker, E. J. and Teal, R. S., "Higher Harmonic Control: Wind Tunnel Demonstration of Fully Effective Vibratory Hub Force Suppression," *41st Annual Forum*, American Helicopter Society, Fort Worth, TX, 1985.

[44] Spangler, R. L. Jr., "Piezoelectric Actuators for Helicopter Rotor Control," Master's thesis, Massachusetts Institute of Technology, Cambridge, MA, June 1989.

[45] Spangler, R. L. Jr. and Hall, S. R., "Piezoelectric Actuators for Helicopter Rotor Control," *Proceedings of the 31st Structures, Structural Dynamics and Materials Conference*, Long Beach, CA, April 1990.

[46] Stroub, R. H., Young, L., Cawthorne, M. and Keys, C., "Helicopter Rotor Blade with Free Tip," *NASA Tech Briefs*, Vol. 16, No. 8, p. 62, 1992.

[47] Walz, C. and Chopra, I., "Design, Fabrication and Testing of a Scaled Rotor with Smart Trailing Edge Flaps," *Presentation Materials from the U.S. Army Research Office First Workshop on Smart Structures*, University of Texas, Arlington, TX, September 1993.

[48] Welsh, W. A. and Blackwell, R. H. Jr, "Higher Harmonic and Trim Control of the X-Wing Circulation Control Wind Tunnel Model Rotor," *45th Annual Forum*, American Helicopter Society, Boston, MA, 1989.